Nearshore flow dynamics over shore-oblique bathymetric features during storm wave conditions

Laura Szczyrba[1], Ryan Mulligan[2], Peir Kenneth Pufahl[1], Josh L Humberston[3], and Jesse McNinch[4]

[1]Queen's University
[2]Queen's University Kingston
[3]Sandia National Laboratories
[4]Coastal and Hydraulics Laboratory, US Army Engineer Research and Development Center

November 14, 2023

Abstract

Shore-oblique bathymetric features occur around the world and have been statistically correlated with enhanced shoreline retreat on sandy beaches. However, the physical mechanisms that explain a causal relationship are not well understood. In this study, radar remote sensing observations and results from a phase-resolved numerical model explore how complex morphology alters nearshore hydrodynamics. Observations at selected times during high-energy storm events as well as a suite of idealized simulations indicate that shore-oblique features induce strong spatial variations in the water surface elevation and wave breaking patterns. Re-emergent offshore flows and longshore current accelerations occur near the apex of the oblique nearshore features. The results suggest that complex bathymetric morphology exerts a powerful control on nearshore hydrodynamics and increases the potential for enhanced cross-shore and alongshore sediment transport, thus contributing to localized erosional zones.

Nearshore flow dynamics over shore-oblique bathymetric features during storm wave conditions

L. Szczyrba, R.P. Mulligan, P. Pufahl, J. Humberston, J. McNinch

[1,2]Department of Civil Engineering, Queen's University
[1,3]Department of Geological Sciences and Geological Engineering, Queen's University
[4]Sandia National Laboratories
[5]Coastal and Hydraulics Laboratory, US Army Engineer Research and Development Center

Key Points:

- Radar and numerical modeling indicate variability in surf zone width and wave height
- Offshore-directed flows occur in a region with shore-oblique sand bars and erosional hot spots
- Morphologic influence and directional variability are quantified with idealized model simulations

Corresponding author: Laura Szczyrba, `20LDS@queensu.ca`

Abstract

Shore-oblique bathymetric features occur around the world and have been statistically correlated with enhanced shoreline retreat on sandy beaches. However, the physical mechanisms that explain a causal relationship are not well understood. In this study, radar remote sensing observations and results from a phase-resolved numerical model explore how complex morphology alters nearshore hydrodynamics. Observations at selected times during high-energy storm events as well as a suite of idealized simulations indicate that shore-oblique features induce strong spatial variations in the water surface elevation and wave breaking patterns. Re-emergent offshore flows and longshore current accelerations occur near the apex of the oblique nearshore features. The results suggest that complex bathymetric morphology exerts a powerful control on nearshore hydrodynamics and increases the potential for enhanced cross-shore and alongshore sediment transport, thus contributing to localized erosional zones.

Plain Language Summary

Near the shoreline, underwater topography is affected by sea level, waves, currents, tides, and geological characteristics. Typically, sandbars are oriented parallel to the coastline, but shore-oblique sandbars have also been identified around the world. In many instances, these oblique features have been correlated with zones of erosion, however the explanation for this statistical relationship is not fully understood. In this study, remote sensing observations and modeling results explore how complex underwater topographies alter coastal wave energy and flow patterns. Selected stormy periods were observed in addition to a set of idealized simulations. Results indicate that shore-oblique features cause localized changes to wave heights, wave breaking, and current speeds. These alterations contribute to the presence of fast offshore-directed rip currents and accelerations in shore-parallel currents, which would enhance the potential for sand to be transported away from these zones. The findings suggest that the changes to the flow field induced by the oblique features contribute to zones of high rates of erosion.

1 Introduction

The coastal nearshore region, defined as the transition zone between the shoreline and the inner shelf, is a dynamic zone shaped by the interplay of many physical processes occurring at various spatial and temporal scales. The level and distribution of incoming wave energy exerts a powerful control on nearshore forces and alters currents, sediment transport, and morphology (Wright & Short, 1984; Svendsen, 1984; Gallagher et al., 1998). When propagating at oblique incident angles to the bathymetric contours, surface waves transfer momentum and drive longshore currents, moving material along the coastline (Longuet-Higgins, 1970; Guza et al., 1986). These currents meander and change velocity in response to bathymetric variability (Garnier et al., 2013). At moderate incident angles, gradients in wave-driven setup of the mean water level can cause local alongshore flows to converge and flow offshore as rip-currents (Castelle et al., 2016; Moulton et al., 2017).

These strong offshore-directed rip currents can scour channels in nearshore sandbars and alter patterns in wave dissipation, causing the local mean water level to slope towards the rip channel (Haller et al., 2002). This feedback reinforces offshore flows and can erode the beach profile (Komar & McDougal, 1988). For weak offshore flows, wave energy dissipation can be reduced in rip-channels, leading to higher wave heights that break close to the shoreline (Haller et al., 2002) and increased vulnerability to erosion (Holman & Sallenger, 1993). In some cases, stable patterns in the underlying bathymetry (e.g., submarine canyons) produce morphologically-driven recurring offshore flows by redirecting wave energy (Long & Özkan-Haller, 2005; Magne et al., 2007; O'Dea et al., 2021). For example, dramatic variations in refraction and wave energy occur across the Scripps

Canyon in southern California, with increased local wave heights at the head of the canyon (Magne et al., 2007).

Morphologically-driven processes are often shaped by the underlying geology (also referred to as antecedent or framework geology). The geologic framework, generated over very long time scales, is characterized by deposits or bedrock underlying modern sediments to a depth of approximately 10 m (Browder & McNinch, 2006). Along the east coast of North America, anomalous nearshore bathymetric features have been identified and connected with geological history: shore-normal or shore-oblique troughs and bars occur in New York (Schwab et al., 2000), New Jersey (Snedden et al., 1994), Virginia (Colman et al., 1990; Browder & McNinch, 2006), North Carolina (McNinch, 2004), Florida (Houser et al., 2008; Barrett & Houser, 2012), northeastern New Zealand (Green et al., 2004), Prince Edward Island (Wernette & Houser, 2022) among many other locations and are commonly related to paleo-river channels. These features alter alongshore patterns in wave breaking (Safak et al., 2017), modify the distribution of wave energy (Mulligan et al., 2019a), and have been hypothesized to act as conduits for offshore sediment transport (Thieler et al., 1995) and enhanced alongshore advection (Gutierrez et al., 2005). However, the physical mechanisms linking framework geology to alterations in hydrodynamics and morphodynamics across the shoreface are not well understood.

In this study, we investigate the influence of a complex bathymetric framework on nearshore flow dynamics during storm conditions at Kitty Hawk, North Carolina, USA. We hypothesize that shore-oblique bathymetric features alter mean nearshore currents and induce localized zones of higher wave height and wave setup on the shoreface, which may affect sediment transport patterns and the morphology of this nearshore region. Both real and idealized storm events are simulated with a phase-resolving numerical model for a wide range of incident wave angles. The event-based simulations focus on time periods with large waves corresponding to Hurricane Jose and Hurricane Maria in 2017, that were also observed with an X-band radar (XBR) remote sensing system. The idealized simulations isolate the effects of the bathymetry and incident wave angle on the nearshore hydrodynamics. The novel combination of remote sensing and numerical results are synthesized to provide new insight on wave-driven flows over complex geologically-controlled bathymetric features.

1.1 Regional setting

Kitty Hawk (KH) is located on the Outer Banks of North Carolina (Fig. 1a). The Outer Banks are a series of long barrier islands segmented by inlets that formed in a microtidal, wave-dominated environment (Hayes, 1979), and are subject to storms (e.g., Tropical Cyclones and Nor'Easters) and high rates of sea level rise (Sallenger et al., 2012; Kemp et al., 2017). These barrier islands have been shaped into cuspate forelands that divide large estuaries (Albemarle and Pamlico Sounds) from the Atlantic Ocean. Currently, few inlets connect the sounds to the ocean and the barrier islands receive a very limited supply of sediment from riverine sources (Culver et al., 2007; Mulligan et al., 2019b). Located 5 km west of the modern transgressive shoreline at KH, a progradational beach ridge complex formed 3 ka - 2 ka before present during a period of rapid Holocene sea level rise and abundant sediment availability (Mallinson et al., 2008). The present-day coastal morphology and dynamics are influenced by the complex underlying regional geologic framework.

2 Shore-oblique features

The segment of coast is dominated by shore-parallel depth contours except near KH, where the nearshore region includes a series of bathymetric undulations with bars and troughs as shown in Fig. 1b. These bathymetric variations are situated in mean water depths ranging from 2-12 m and are oriented offshore at an average angle of 42° from the shoreline (Schupp et al., 2006). The morphologic features are referred to as shore-oblique features (SOFs) and, within the region considered in the present study, include a northern (SOF-N) and southern (SOF-S) trough shown in Fig. 1b. Seismic imaging studies have associated these bathymetric anomalies to underlying Pleistocene paleo-channels, specifically the paleo-Roanoke River (Boss et al., 2002; McNinch, 2004; Browder & McNinch, 2006). Cycles of eustatic sea-level changes that occurred concurrently with glacial episodes during the Pleistocene epoch dissected numerous fluvial channels into the underlying Quaternary strata (Boss et al., 2002). During the ensuing Holocene transgression, these channels were drowned and infilled with muds, peats, sands, and gravels (Riggs et al., 1992, 1995; Schwartz & Birkemeier, 2004).

The SOFs are relatively stable but can migrate approximately 250 m alongshore in response to individual storm events (McNinch & Miselis, 2012). Schupp et al. (2006) found that all movement was confined to zones shoreward of the -9 m bathymetric contour. They also slowly migrate downdrift on a decadal timescale. Between 2004 and 2017, SOF-N migrated south by approximately 600 m and deepened by 0.5 m (Szczyrba et al., 2023a). Regionally, these SOFs have been correlated with areas of high shoreline variability and, on longer time scales, high long-term shoreline change rates. McNinch (2004) visually identified a correlation between the SOFs and high shoreline change rates and Schupp et al. (2006) quantified this correlation on a regional scale as statistically significant. However, the nearshore hydrodynamic processes that physically link the SOFs with erosion have not been well defined.

3 Observations

3.1 Bathymetry and wave data

In June, 2017, bathymetric profiles were collected to support the local beach nourishment monitoring plan (APTIM, 2017). The nearshore survey lines were collected by a survey vessel and spaced approximately 150 m meters apart, with sounding points sampled every 7-8 m (APTIM, 2017). The survey data were interpolated onto a 5 m x 5 m regular grid in ArcGIS 10.7.1, encompassing two shore-oblique bathymetric features (SOF-N and SOF-S). This bathymetric grid, shown in Fig. 1c, is used as input to the numerical model.

Wave observations used as boundary conditions in the numerical model were sourced from the US Army Corps of Engineers Field Research Facility (FRF) at Duck, located 14 km north of KH. Wave spectra were observed by a 1 MHz Nortek Acoustic Wave and Current (AWAC) profiler, located offshore in a nominal depth of 11 m. Previous studies have shown that the bulk wave statistics including significant wave height (H_s), mean direction (θ_m), and peak period (T_p) are highly correlated at the 11 m depth over a distance of 33 km between the FRF and Jennette's Pier, located 20 km south of KH (Mulligan et al., 2019a). Wave data were obtained for key times during major wave events in September 2017. These correspond to a time during Hurricane Jose (denoted "J"; 19-September-2017 20:00:00 UTC), and two times during Hurricane Maria (denoted "M1" and "M2"; 27-September-2017 09:00:00 UTC and 28-September-2017 02:00:00 UTC) indicated in Fig. 2 and Table 1. Directional energy-density wave spectra were used as offshore boundary conditions for the numerical model (Fig. 3). The directional spectra were calculated from the first four Fourier coefficients, using the maximum entropy method (Lygre & Krogstad, 1986) with a directional resolution of 1°, a frequency resolution of 0.0075 Hz, and a frequency range of 0.0400-0.4975 Hz. The spectra were rotated 28° clockwise of true north to match the orientation of the rotated bathymetric grid before they were input into the model.

The times corresponding to J, M1, and M2 were selected because they have similar mean total water levels, and a range of energy levels and incident wave angles (Table 1 and Fig. 3). Hurricane Jose at time J was a moderate wave height ($H_s = 2.8$ m) event with a positive incident angle (meaning north of shore-perpendicular) and moderate directional spreading (Fig. 3a, d, g). Hurricane Maria at time M1 was a high-energy event, with an H_s of 4.0 m, long period waves, low directional spreading and an oblique positive incident angle (Fig. 3b, e, h). As Hurricane Maria propagated along the coastline, the dominant wind and wave direction shifted and the conditions at time M2, which occurred 17 hours after M1, had moderate wave heights ($H_s = 2.6$ m) and periods during the passage of the storm. Time M2 was characterized by high directional spreading from the high-frequency oblique wind-waves forced by strong offshore winds (Fig. 3c, f, i).

3.2 X-band radar collection and processing

The Radar Inlet Observation System (RIOS) is a fully automated non-Doppler XBR remote sensing system housed within a mobile trailer for rapid deployment (McNinch et al., 2012; Humberston et al., 2019). RIOS emits microwave radio signals with a horizontal beam width of 1.2° and a vertical beam width of 25° and records the subsequent backscatter. Bragg resonance is the primary mode of XBR backscatter, wherein radar pulses interact with short capillary waves (1-2 cm wavelength, λ) on the water surface. Backscatter increases when waves steepen, modulating the short-gravity wave field, and become roughened as they approach the shoreline and break (Catalán et al., 2014). Thus, RIOS provides a digital reconstruction of the incoming nearshore wave field as a series of sequential spikes in the XBR backscatter return intensity. XBR can resolve the spatio-temporal evolution of incoming nearshore waves and the observations compare well to both numerical models and in-situ data (Szczyrba et al., 2023b). Additional RIOS-system details are described by Humberston et al. (2019) and McNinch et al. (2012).

RIOS was deployed in the study site at the location shown in Fig. 1b (36.066408°, -75.690222°) in September, 2017. Nearshore sea surface conditions were observed for 14 minutes per hour between September 19-23 and September 27-30, capturing J, M1, and M2 time periods. The XBR antenna completed a rotation every 1.67 s, resulting in a sampling frequency of 0.60 Hz. Raw backscatter data were transformed from polar coordinates onto a 5 m x 5 m Cartesian grid (Humberston et al., 2019) and smoothed in the alongshore direction by 100 m using a multidimensional image averaging filter (imfilter). The resulting grid was rotated 28° clockwise of true north to match the orientation of the numerical modeling framework. Overall, the XBR footprint spanned 3 km alongshore and 1 km offshore. The time-dependant surf zone width was calculated from 14 minute time-averaged XBR backscatter data. Time-averaged XBR and optical data highlight zones of high dissipation and are often used to determine the spatial patterns of wave breaking (Lippmann et al., 1993; Brodie et al., 2018). Following the method described by O'Dea et al. (2021), the offshore surf zone edge was identified as the maximum cross-shore gradient of the XBR backscatter intensity, calculated at each alongshore location. Outliers were removed and the resulting surf zone edge lines were smoothed using a moving mean filter with a window size of 100 m.

Methods from O'Dea et al. (2021) were also applied to search for and identify morphologically driven offshore-directed currents in the study region. This approach analyzes backscatter intensity offshore of the surf zone where few waves are breaking. Offshore flows escaping beyond the breaker line can be identified in the XBR data as alterations in surface roughness. Offshore directed rip currents enhance sea surface roughness, incite short-scale wave breaking (i.e. microbreaking), and elevate XBR-measured backscatter intensity (Lyzenga, 1991; Plant et al., 2010; Haller et al., 2014; O'Dea et al., 2021). This effect has been confirmed in a study utilizing both XBR and GPS-equipped floating drifters (Takewaka & Yamakawa, 2011) and with a cross-shore array of current meters (Haller et al., 2014). To identify these zones of wave-current interaction, an alongshore transect of backscatter intensity was extracted at a location 100 m offshore of the surf zone edge during periods with waves with $H_s \geq 2$ m. The mean backscatter intensity was removed from each transect to highlight zone of anomalously high return intensities. The intensity anomaly transect data were then averaged together to identify persistent XBR backscatter anomalies in the 9-day observation period. The XBR anomalies for J, M1, and M2 were also analyzed.

XBR observations were used to determine representative wave phase speeds. Pixel intensity time series were input into the bathymetric-inversion algorithm cBathy (Holman et al., 2013b; Holman & Bergsma, 2021). cBathy is typically used to estimate bathymetry from optical imagery, often from Argus camera systems (e.g., Oades et al. (2023)), but can also process XBR data (Honegger et al., 2019). Resulting XBR-derived bathymetric surfaces have been applied in numerical modeling studies (O'Dea et al., 2021). The algorithm estimates the wave numbers (k) of dominant wave frequencies (f) and uses the linear dispersion equation to relate these k-f pairs to mean water depth. The k-f pairs are extracted within mapped tiles by calculating the Fourier phase cross-spectra between each pixel per tile. In the present study, tile spacings were set to be 10 m in the cross-shore direction and 25 m in the alongshore direction. The algorithm produces a matrix of wave numbers for each the most coherent 4 frequencies wherein the individual matrices contain a range of frequencies that represent the most dominant frequency calculated per pixel.

The most coherent k-f matrix was extracted to create wave speed maps of representative peak wave conditions for each event. cBathy's accuracy declines significantly in very shallow water with $h <$ -2 m (Honegger et al., 2019), therefore these regions were excluded from further analyses. Cross-shore transects were extracted to support comparisons with the modeling data with a 20 m moving mean applied to eliminate noise. Using the peak frequency calculated from cBathy, the method of Streßer et al. (2022) was adapted to convert XBR-measured wave phase speeds to representative wave height estimates (see Eq. 12 in Streßer et al. (2022)). Their wave-by-wave approach applies a physically derived scaling that relates changes in breaking phase speed to wave height via the amplitude dispersion relation:

$$H_p = \frac{{C_p}^2}{g(\frac{1}{\gamma} + \alpha_{ad})} \tag{1}$$

This equation was applied using the celerity of the peak frequency (C_p), the default breaking index (γ) value of 0.78 (Streßer et al., 2022; Larson & Kraus, 1994), and the recommended calibration coefficient (α_{ad}) value of 0.5 (Streßer et al., 2022) to estimate a representative wave height based on peak frequency values (H_p). This method is valid within the surf zone, since it was developed based on the modified nonlinear shallow water phase speed for waves in very shallow water (i.e., h:$\lambda < 1/10$) from Hedges (1976).

4 Numerical model

The phase-resolving 3D numerical model Simulating WAves till SHore (SWASH) applies the nonlinear shallow water horizontal momentum equations and the nonhydrostatic vertical momentum equation using a finite difference scheme (Zijlema et al., 2011; Zijlema, 2020) to simulate the water surface and velocity fluctuations. SWASH was applied to simulate several times (J, M1, M2) in the study period that correspond to radar data collection times. In addition to the selected events, an idealized suite of 21 simulations were also performed to isolate key variables and specifically explore how the incident wave conditions affect the nearshore hydrodynamics.

4.1 Model setup

SWASH has been used to simulate wave-driven currents over variable bathymetry, such as over submerged reefs (da Silva et al., 2023). Previous studies have also applied SWASH to model regions near the present study area (Gomes et al., 2016; Mulligan et al., 2019a; Szczyrba et al., 2023b) and similar numerical input parameters were applied in this study. A 5 m x 5 m regular structured grid, extending 1000 m offshore and 3000 m alongshore, was constructed. A 300 m extension was added to the offshore edge of the bathymetric grid (from x = 1000-1300 m) to create a uniform offshore region and prevent numerical anomalies from being introduced due to depth variations at the east boundary (without the extension, the bathymetric variations at the model boundary causes numerical instabilities that are not realistic). The extension was created by linearly interpolating the offshore bathymetric edge to a constant depth of h =-12 m over a cross-shore distance of 100 m and then extending this constant depth over the remaining 200 m, following previous studies (O'Dea et al., 2021). The bathymetry was also extended by 500 m in each alongshore direction by interpolating the sides to a uniform contour configuration in order to enable the application of periodic alongshore boundary conditions in the numerical model. The bathymetry data was rotated 28° clockwise of true north which oriented the mean shoreline parallel to the y-axis of the grid (Fig. 1c). To resolve depth-dependent dynamics, three bathymetry-following vertical layers with equal thickness were included. This vertical resolution is sufficient to resolve wave frequency-dispersion (Zijlema & Stelling, 2005; Smit et al., 2013). To confirm this, a sensitivity test using 9 vertical layers was conducted to explore the flow structure in and around the SOFs in further detail, and found no substantial differences from the 3-layer runs.

The Sommerfeld radiation condition was applied at the onshore boundary to appropriately limit wave reflection and the offshore boundary was weakly reflective. The alongshore boundary was periodic, meaning that energy exiting one alongshore boundary re-entered the domain at the opposite alongshore boundary. The first 15 minutes of modeling time were disregarded as model spin-up and the remaining 45 minutes were analyzed. The wavemaker generated random wave time series that statistically matched the input wave parameters with a cycle interval of 2700 seconds (45 minutes). According to Zijlema et al. (2011), the cycle time should span 100-300 peak wave periods to provide accurate statistical results and the selected cycle time spans over 200 wave periods of the longest peak period simulated (M1). The model performed calculations with an initial time step of 0.05 s that is automatically adjusted throughout the simulation according to the Courant number, which can reach a maximum of 0.5. Total water levels were adjusted for the correct tidal stage and storm surge present during the simulated events. Event times during hurricane wave events J (Jose), and M1, M2 (Maria) were forced at the offshore boundary using the directional energy-density spectra for each corresponding time (Fig. 3g-i).

4.2 Model output processing

To enable direct comparison with the XBR cBathy products, spectral processing extracted peak wave frequency parameters per grid cell from the J, M1, and M2 simulations. The fast Fourier transform was calculated at each grid cell with 256 samples and a Hanning window with 50% overlap. The peak wave frequency per grid cell was also extracted and used to calculate k and λ with the dispersion relation (Fenton & McKee, 1990; Dean & Dalrymple, 1991). The representative C_p was then calculated and input into Eq. 1. This approach emulates the XBR processing steps. H_s was calculated across the computational domain as four times the standard deviation of the water surface elevation output (Raubenheimer et al., 1996). The spatial gradient of the water surface elevation data highlighted wave crests as locations with steepest slopes. Vectors perpendicular to these crests at each grid cell were then time-averaged to provide local estimates of mean wave angles across the study region (Szczyrba et al., 2023b). A dimensionless wave breaking parameter (Q_b) was calculated from the binary wave breaking locations output from the model (Gomes et al., 2016). This parameter represents the relative intensity of breaking independent of the model time step and spatial resolution. These breaking zones were compared to the surf zone widths observed by XBR.

5 Results

5.1 Event flow dynamics

Regions of persistently high XBR backscatter outside of the surf zone were identified for J, M1, and M2 as well as the mean during all periods with $H_s \geq 2$ m observed by XBR (Fig. 4). The strongest XBR anomalies occur at the southern edge of SOF-N and the southern edge of SOF-S, located at y $\sim$ 1600 m and y $\sim$ 250 m (Fig. 4b-d). Each event, as well as the study-period mean, indicate anomalously high backscatter signals at these locations. Offshore flows enhance XBR backscatter intensity where wave-current interactions roughen the sea surface. Even during lower energy periods, high backscatter indicative of offshore flow extends outside of the surf zone. For example, as shown in Fig. 4d, at a time when $H_s = 2.3$ m, high backscatter return intensity (RI) is evident at y $\sim$ 1600 m and y $\sim$ 250 m. The signals along the southern edges of both SOFs are strongest during M2, an event with negatively incident (southerly) waves. Spikes in XBR backscatter also occur along both the northern and southern edges of SOF-S during M2, and in the channel trough backscatter measures abruptly weaken (Fig. 4b, c). In the mean observations, this U-shaped pattern in the XBR anomaly can be observed in both SOFs and is much wider in SOF-S than SOF-N. This U-shape indicates increased backscatter along both edges of each SOF, with the southern edge inducing stronger backscatter. M1, an event with large waves approaching the shoreline at a highly oblique, positive (northerly) angle, only exhibits backscatter anomalies along the southern edges of the SOFs, and no anomaly is detected near the northern edges. The strongest XBR anomalies align approximately with regions of higher local shoreline change rates, i.e., erosional hot spots (List et al., 2006), with a slight offset (Fig. 4a, b). Each hot spot is offset north of the southern edge of SOF-N and SOF-S, where the highest XBR anomalies occur.

The observed and simulated extent of the surf zone are shown in Fig. 5. Event M1 was the highest energy event with the widest surf zone (Fig. 5a). Mean surf zone widths are 223 m, 281 m, and 269 m for J, M1, and M2, respectively, however the extents vary considerably in the alongshore direction. The surf zone of M1 is widest north of SOF-N, beginning offshore at x $\sim$ 340 m. The surf zone of M2 is widest south of SOF-N, occurring at x $\sim$ 320 m. During all events, surf zones narrow along the shoreward apex of SOF-N and widen on either side, coincident with the feature's edges. SOF-N modulates surf zone widths more than SOF-S. The offshore extent of the surf zone identified by XBR (Fig. 5a) was compared to the breaking parameter (Q_b) calculated from the numerical model (Fig. 5b). The XBR-sensed surf zone edge aligns with the offshore edge of the most intense breaking locations in the SWASH simulations and displays similar lateral variability in break-point locations. During M1, Q_b is most intense at x $\sim$ 200 m, y $\sim$ 2,000, which is located along the northern edge of SOF-N (Fig. 5b).

Spatial patterns in C_p shown in Fig. 6 are similar in XBR observations (Fig. 6a) and SWASH results (Fig. 6b), wherein C_p remains high within the shore-oblique troughs as the waves approach the shoreline, coinciding with the bathymetric contours. Peak frequency waves enter the domain at 9-10 m/s and slow to 6-7 m/s along the 4 m bathymetric line. Across a variety of cross-shore profiles, XBR and SWASH estimates agree well (Fig. 6c-e). Mean C_p errors are 0.26, 0.26, and -0.04 m/s for J, M1, and M2, respectively, however errors vary spatially. In the cross-shore, error is highest shoreward of x $\sim$ 335 m where the model slightly underestimates C_p by 0.47 m/s when compared to XBR observations. In the alongshore, the model underestimates C_p north of y $\sim$ 1,750 m and overestimates south of y $\sim$ 1,500 m. Across all periods simulated, mean error is highest between y $\sim$ 925 - 1,225 m with a maximum of -0.53 m/s.

Using Eq. 1, spatial distributions of C_p were converted into representative wave heights (H_p) to further compare XBR and model results as shown in Fig. 7. Patterns in H_p compare well between XBR and the model. Wave heights vary laterally across the study domain, with higher wave heights reaching closer to the shoreline in the lee of the troughs of the SOFs. Wave dissipation begins along the 4 m contour lines. Root mean square errors (RMSE) are 0.76 m, 0.72 m, and 0.65 m across the entire domain and 1.35 m, 0.61 m, and 0.57 m within the surf zone for J, M1, and M2, respectively.

Fig. 8 displays the spatial patterns in relative wave height H_s/h (Fig. 8a) and wave frequency (Fig. 8b) alongside the alongshore distributions of the normalized maximum H_s (Fig. 8b) and the water surface elevation gradient (Fig. 8c) The distribution of modeled H_s varies across space and by event (Fig. 8a, b). Relative wave heights are elevated north and south of SOF-N around y $\sim$ 2000 and 1500 m, and in these zones high relative wave heights extend to the 6 m contour (Fig. 8a). H_s values increase near the SOFs and decrease in the region between SOF-N and SOF-S (Fig. 8b). During all events, H_s increases along the edges of the SOFs, following the bathymetric contours, and decreases along the central axes (Fig. 8b). The alongshore differences in H_s at a particular cross-shore location varies between 0.2-0.4 m. The alongshore variability in wave heights also induces strong variations in the water surface elevation gradient (Fig. 8c). At SOF-N, the minimum alongshore gradient occurs at y = 1665 m and then sharply increases on either side of that location across all events. The mean wave frequency is also elevated along the southern edges of SOF-N and SOF-S, coincident with the abrupt alongshore variations in wave setup (Fig. 8c), indicative of wave-current interactions. The wave frequency changes displayed in Fig. 8d appear similar to the XBR backscatter patterns displayed in Fig. 4d.

Simulated wave angle and velocity results near SOF-N during J, M1, and M2 are shown in 9. The SOFs modulate patterns of wave refraction during each event (Fig. 9a-c). M1 waves maintain positive approach angles across the domain even near the shoreline but are moderated closer towards shore-normal in the lee of SOF-N. J and M2 waves refract into positive and negative directions, creating zones of convergence and divergence around SOF-N. In both events, divergence occurs along the northern edge of SOF-N while convergence occurs along the southern edge. A similar, but less severe effect, is observed around SOF-S. The features cause asymmetric wave refraction, whereby wave entering at moderate angles refract away from the trough and toward the edges of the SOFs (Fig. 9a-c), increasing wave heights along the edges and sheltering the zone immediately in the lee of the trough (Fig. 8b).

Across all three selected times, cross-shore velocities are directed offshore down the oblique central axis of SOF-N (Fig. 9d-f), coinciding with the locations of wave divergence (Fig. 9a-c). These flows decelerate and broaden as they move offshore. Cross-shore velocities route back onshore at the southern edge outside of the surf zone and this shoreward-directed patch occurs 50 m farther offshore during M1 than during J and M2. North of SOF-N, cross-shore velocities are also directed onshore during J and M2, but this effect is weak during M1. The offshore and onshore-directed velocities thus form asymmetric circulation cells, with the stronger cell occurring along SOF-N's southern edge. The location of the maximum and minimum cross-shore velocities remain fairly stable across all three periods simulated. Alongshore velocities accelerate and meander significantly offshore near SOF-N in J and M2 (Fig. 9g-i). The acceleration in both events occurs near x $\sim$ 250 m, y $\sim$ 1750 m. During M1, the alongshore velocities are very strong and meander slightly in response to the SOF contours. The longshore current reverses direction during M2 at x $\sim$ 300 m, y $\sim$ 1950 m, and the nexus of the reversal coincides with a location of high cross-shore velocity.

During J and M2, the mean flow is characterized by two circulation cells between (1) x ∼ 0-500 m, y ∼ 2000-2500 m and (2) x ∼ 0-500 m, y ∼ 1500-2000 m (Fig. 9j-l). The southern circulation cell is stronger than the northern cell. While water moves offshore down the axis of SOF-N in J and M2, the mean current merely meanders in response SOF in M1 since the strong inertia of the longshore current overpowers potential circulation cells. The offshore-directed flows in J and M2 maintain high velocities offshore of the surf zone, with fast flows identifiable up to 2 surf zone widths away from shoreline. Offshore of SOF-N at x = 600 m, the maximum velocities occur in similar locations (U = 0.57 m/s, 0.90 m/s, 0.54 m/s at y = 1820 m, 1515 m, 1500 m for J, M1, M2, respectively) and the minimum velocities also occur in similar locations (U = 0.45 m/a, 0.79 m/s, 0.40 m/s at y = 2275 m, 2065 m, 2255 m for J, M1, M2, respectively). The alongshore velocity component plays a larger role than the cross-shore velocity component in controlling the overall mean current.

5.2 Idealized effects of incident wave conditions

A second suite of idealized simulations isolated the effects of various wave conditions including incident θ_p and H_s on nearshore hydrodynamics. These simulations were forced by a JONSWAP spectra with a T_p of 12 s and zero directional spreading. The H_s values varied between 1.0, 3.0, and 5.0 m while θ_p varied between -15 to 15° in intervals of 5°. It should be noted that the ideal simulation with an H_s of 5.0 m and θ_p of 15° failed because large waves at highly oblique angles are challenging to simulate (Baker et al., 2021). Thus, results for that simulations pertain to an H_s of 4.9 m at θ_p of 15°.

Model results of Q_b across a variety of incident wave approach angles are shown in Fig. 10. Incident waves that approach from +15° and transition to -15° emulate a common pathway of tropical cyclones in this region and Q_b varies depending on the incoming θ_p (Fig. 10). Q_b is dispersed relatively evenly alongshore between the 6 m depth contour and the shoreline when incident waves approach at +15°. However, Q_b begins further offshore along the edges of SOF-N and closer to the shoreline at the shoreward apex of the SOF. Between +10° - 0°, Q_b begins to concentrate along the northern edge of SOF-N. The breaking region is most localized when incident waves approach at -5°, focused at the shoreward apex of SOF-N (near x = 150 m, y = 1750 m) as well as SOF-S (near x = 250 m, y = 500 m). North of SOF-N most breaking occurs at the shoreline. At -10°, waves break again across the northern sandbar. Finally, at -15°, breaking is more widely distributed across the axes of both SOF-N and SOF-S.

Simulated U across a variety of incident wave approach angles are shown in Fig. 11. When waves approach the shoreline at highly oblique angles, a strong longshore current develops with minor offshore movement (Fig. 11a-b, f-g). The longshore currents accelerate at the apex of SOF-N, near y = 1900 m, and SOF-S, near y = 500 m, and the flow also meanders slightly offshore in these zones. With moderate incident θ_p, several offshore circulation cells develop. During moderately positive incident angles, offshore flows route down the northern edges of the SOFs (Fig. 11b, c) while during moderately negative incident angles, they flow down the southern edges of the SOFs (Fig. 11e, f). During periods of negative wave incidents (Fig. 11e-g), a localized zone of flow acceleration away from the shoreline develops at the location where the shoreline angle changes orientation, between y = 1400 - 1600 m.

Across all simulations, weak offshore flows are consistently present along either the northern or southern edges of SOF-N and SOF-S and these offshore currents exit the computational domain, 1 km away from the shoreline (Fig. 11). However, at moderate incident angles, the offshore flows strengthen, coalesce, and develop complex pathways. Near the shoreline, a series of alongshore feeder currents converge and route offshore across a wide zone around SOF-N (Fig. 11c-e). Beginning at an incident angle of +5°, four distinct zones of offshore-routed flows develop at y = 250 m, y = 1100 m, y = 1600 m, and y = 2500 m (Fig. 11c). These flows strengthen as incident angles shift towards -5° and begin to converge into two dominant offshore routing zones (near y = 750 m and 1800 m) which are continually present as wave angles continue to become more oblique at -10°, identifiable at y = 450 m and y = 1750 m (Fig. 11f).

6 Discussion

6.1 Model error assessment

Several past studies have evaluated a similar model configuration at the FRF and found that model results of H_s and energy-density spectra compare well with in-situ sensors located across the nearshore region (Gomes et al., 2016) as well as spatially-continuous XBR estimates of wave angles and wave breaking patterns (Szczyrba et al., 2023b). In the absence of in-situ sensors situated within the study site, the accuracy of the J, M1, and M2 simulations is assessed through a comparison to the XBR observations of surf zone width, celerity, and wave height. The alongshore variability in surf zone width measured by XBR is well represented by patterns of Q_b simulated in the model (Fig. 5b). Mean celerity errors are low, ranging from -0.04 to 0.26 m/s. Errors are highest shoreward of x = 400 m, where high rates of bathymetric change occur (Fig. 6).

Estimates of H_p are also in good agreement and both depict similar alongshore variability in response to the complex bathymetric configuration (Fig. 7). The best available bathymetric data were surveyed in June of 2017. Subsequent changes in the nearshore morphology, particularly in the surf and swash zones, would lead to differences in wave parameters estimated from XBR and SWASH and contribute to the identified errors. Past studies have indicated that the SOFs in the region remain in fixed locations even after energetic wave events (McNinch, 2004; Browder & McNinch, 2006; Schupp et al., 2006), therefore it is expected that high errors due to alterations in the bathymetry would be confined to zones closest to the shoreline.

6.2 Identification of rip currents

Anomalously high XBR backscatter signals seaward of the surf zone can occur where incoming waves interact with surface current convergences, such as rip currents and other offshore flows (Takewaka & Yamakawa, 2011; Haller et al., 2014; O'Dea et al., 2021). Backscatter anomalies indicative of strong offshore currents are visible in nearly every collection hour with incident $H_s \geq 2$ m (Fig. 4d). These offshore flows emerge in two primary locations, between y = 200 - 400 m and between y = 1500 - 2000 m. Flow structures remain visible for several hours across a variety of incident angles, water levels, wave periods, and directional spreading conditions. The visible plumes also extend 1-3 surf-zone widths beyond the XBR-identified surf zone edge (Fig. 4), supporting the findings of Kumar et al. (2021) and O'Dea et al. (2021).

Because the observed currents re-emerge in similar positions, they are likely morphologically controlled (Short, 2007). These flow structures are more obscured when wind levels in the region reach above 10 m/s (Fig. 4c) because XBR images become saturated during periods of high water surface roughness (Haller et al., 2014). Another limitation of XBR is the requisite for depth-limited wave breaking. Small waves below ∼1 m are not large enough to be resolved by XBR, although this threshold is site-specific (McNinch, 2007). However, rip currents are also more likely to be generated as wave energy increases (MacMahan et al., 2005), thus XBR remains a useful tool to identify them.

The observed reoccurring offshore flows coincide with the locations of SOF-N and SOF-S and are also represented in simulations of J, M1, and M2 (Fig. 8d and Fig. 9j-l). Because the maximum current velocities outside of the surf zone at x = 600 m reach values between 0.54 - 0.90 m/s during these events, these flows would pose a risk to human safety and thus can be considered morphologically-controlled rip currents (Leatherman & Fletemeyer, 2011). Similar re-emergent flows are also represented in the idealized simulations with H_s values of 1 m, 3 m, and 5 m (Fig. 11). Even during low energy conditions ($H_s = 1$ m), narrow bands of weak offshore flow appear in a similar location shoreward of SOF-S (flows originating near y = 500 m) and SOF-N (flows originating near y = 1500 m).

During higher energy conditions ($H_s = 3$ m and 5 m), the origin of the offshore flow within the surf zone is more variable, however the flows preferentially route along either the northern or southern edges of SOF-N and SOF-S. When waves approach at a positive angle, depth-averaged currents are directed onshore along the southern edge (upstream side of the SOF) and are offshore-directed along the northern edge (downstream side). The opposite circulation pattern emerges when waves approach at a negative angle, with offshore flows directed along the southern edge. This patterns is similar to observations of a dredged rip channel by Moulton et al. (2017), wherein a commonly observed circulation pattern included meandering longshore currents with offshore-directed flows occurring on the downstream rip channel wall.

Other studies have linked complex bathymetry to rip current generation. Along the northern shore of Prince Edward Island, Canada, Wernette and Houser (2022) proposed a relationship between paleo-river channels identified by ground-penetrating radar and rip currents observed by aerial imagery. At the present study site, results indicate that the SOFs act as a pseudo-transverse bar and rip morphology, which is associated with a common class of rip currents (Holman et al., 2006; Short, 2007; Turner et al., 2007). However, the SOFs remain fixed in place with little change, as opposed to ephemeral sandbar features that migrate shoreward after a storm reset (Houser et al., 2020). This process is akin to the shoreface-connected ridges on Fire Island, New York that have also been shown to modify wave refraction and produce alongshore variable wave breaking patterns (Safak et al., 2017).

6.3 Rip current generation

Rip currents are driven by gradients in wave momentum (Longuet-Higgins & Stewart, 1964) resulting from alongshore variations in wave breaking (Lippmann & Holman, 1989). These variations can be caused by hydrodynamic forcing, such as intersecting wave trains, standing edge waves, and wave spreading (Bowen, 1969; Suanda & Feddersen, 2015; Kumar & Feddersen, 2017; Moulton et al., 2023), or artificial structures, such as piers and groynes (Pattiaratchi et al., 2009). However, they are more often induced by alongshore variations in surf zone morphology (Bowen, 1969; Dalrymple, 1978). While the SOFs at this site are not morphologically pronounced within the surf zone, they are persistent nearshore structures that visibly impact the configuration of the bathymetry in areas of depth-limited breaking during higher energy wave events (e.g., the 4 m isobath, Fig. 1). Thus, the SOFs induce substantial alongshore variability in wave setup (Fig. 8c).

Nearshore wave heights respond to changes in nearshore bathymetry and the present results indicate that larger waves reach closer to the shoreline along the axis of the SOFs (Fig. 7), supporting the conclusions of Mulligan et al. (2019a) and observations by Sonu (1972) at other sites. Waves refract across the obliquely variable bathymetry (Fig. 9a-c), creating zones of wave energy convergence and alongshore variations in H_s (Fig. 8a, b). As a result, alongshore variations in wave breaking and surf zone widths also occur (Fig. 5), which can drive rip currents (Bowen, 1969; Dalrymple, 1978). Higher setup is generated near the shoreward side edges of the SOFs due to variability in wave breaking (Fig. 8c), leading to a pressure gradient that forces water to flow away from regions of intense breaking towards zones of lower setup. When these alongshore flows converge, they route offshore (Fig. 9), interact with the incoming wave field, and cause localized zones of higher frequency waves (Fig. 8d) and rougher water (Fig. 4b). These results support the findings of experimental rip channel studies (Haller et al., 2002; Moulton et al., 2017).

6.4 Influence of wave climate

The mean incident wave conditions near KH throughout 2017 included a significant wave height of 0.87 m, mean incident angle of 17°, and 32° of directional spreading. However, Nor'easters and tropical cyclones generate a variety of high-energy incident wave conditions in this region. When waves approach the SOFs at angles close to the orientation of the axis (negative incident angles, in our coordinate system), wave breaking occurs in concentrated local patches (Fig. 10). When approaching from the opposite direction (positive incident wave angles), wave breaking is more widely distributed along the 4 m isobath. These findings support Safak et al. (2017), who concluded that when waves approach shoreface-connected ridges at angles similar to the angle of the ridge crests, the features focused the most wave energy. Strong offshore flows (i.e., rip currents) are more likely to occur when wave angles approach the site between -10° to 10° (Fig. 11). Rip currents are more prevalent during conditions of moderate incident wave angles (Engle, 2002; MacMahan et al., 2005; Dusek & Seim, 2013a) because highly oblique angles induce strong longshore currents that inhibit offshore flow (Kumar et al., 2011). During positive, oblique incident conditions (15°), the longshore current accelerates where the contours of the SOFs pinch towards the shoreline (Fig. 11a) whereas during negative, oblique conditions (-15°), this acceleration occurs south of the SOFs.

Numerous weak offshore flows occur during periods of low energy, however these offshore flows re-emerge in similar positions across a variety of incident wave angles. As H_s increases, these offshore flows coalesce into larger, stronger offshore flows resembling rip currents (Fig. 11 that preferentially route down either the northern or southern edges of the SOFs when incident wave angles enter the domain between -10° to 10°. Fig. 12 explores the idealized effect of incident H_s and θ on maximum U (Fig. 12a, c-e) and variability of U (Fig. 12b, f-h) at the mean XBR-measured surf zone location as well as two zones located 250 m and 500 m offshore. Within the surf zone, maximum U values are mostly found at the shoreward axis of SOF-N, located at approximately $y = 1650 - 2000m$ (Fig. 12a). Additionally, U generally increases with increasingly oblique waves, owing to the generation of a strong longshore current (Fig. 12c). The variability of U is higher for negatively incident waves, but is highest for waves of moderate incident angles (Fig. 12f). Both mean U and the variability of U decrease offshore and increase with larger H_s. At all cross-shore locations, the variability of U decreases with increasingly oblique incident waves (Fig. 12f-h). The locations of maximum U variability are concentrated along the southern edges of both SOF-N and SOF-S (Fig. 12b).

The idealized simulations do not represent realistic field conditions, but are intended to isolate the response to different incident wave conditions. This set of simulations included JONSWAP spectra with zero directional spreading. Several studies have suggested that rip currents are more pervasive during narrow-banded incident conditions (Dusek et al., 2011; Dusek & Seim, 2013b), therefore the idealized results can not be used to predict rip current activity. However, XBR images indicate that rip currents at this site are indeed generated throughout a range of incident angles and directional spreading values (Fig. 4). The purpose of the idealized results is to explore the sensitivity and response of the SOFs to isolated variables (i.e. θ, H_s). It is also well known that rip current intensity varies in response to the total water level (e.g., tidal stage) and that strong rip currents can occur at low tide even during periods of low energy conditions due to enhanced wave breaking over surf zone sandbars (Brander & Short, 2001; MacMahan et al., 2005; Voulgaris et al., 2011). Overall, bathymetrically controlled rip currents tend to be strongest and most prevalent during periods of low water levels, high H_s, moderate incident $|theta$, and low spreading (Haller et al., 2002; MacMahan et al., 2010; Moulton et al., 2017).

6.5 Implications for hot spots of erosion

Prior studies have demonstrated that, at the regional scale (i.e., $\sim$ 40 km alongshore length), SOFs in the Outer Banks correlate significantly with erosional hot spots (McNinch, 2004; Schupp et al., 2006). The physical mechanisms contributing to the causal relationship have previously not been determined. The results of this research suggest that strong cross-shore fluxes (i.e., rip currents) are concentrated near the SOFs during periods with moderate incident wave angles. Between 2012 and 2022, 72 beach rescues specifically related to rip currents occurred within the study site (Kitty Hawk Ocean Rescue, personal communication, September 28, 2023). Rip currents and surf zone eddies are the primary mechanisms for cross-shore sediment transport (MacMahan et al., 2006; Dalrymple et al., 2011; Castelle et al., 2016) and Splinter and Palmsten (2012) found that areas of higher dune erosion occur where rip currents are present directly offshore. During periods of both high wave energy and moderate wave angles, strong offshore-directed flows may pronounce offshore transport, leading to enhanced erosion and undulations in the shape of the shoreline, similar to the results found in Fire Island, New York by Safak et al. (2017). During conditions with more oblique incident wave angles, longshore currents accelerate near the SOFs due to alongshore variability in bathymetry, which would also contribute to higher rates of sediment transport. Therefore, across a range of incident wave conditions and energy levels, a combination of longshore current accelerations and far-reaching offshore flows could contribute to the severity of beach erosion near the SOFs at this site.

Bathymetric surveys indicate that between 2004 and 2017 the trough of the 4 m contour within SOF-N and SOF-S deepened and moved south by 300 - 400 m (Szczyrba et al., 2023a). This might explain the southerly offset between the origin of the morphologically controlled rip currents and the long-term shoreline change rates (Fig. 4). We hypothesize that bathymetric hysteresis causes the erosional hot spot to lag behind the southerly movement of the SOFs and, therefore, in the future the hot spot will migrate south. When comparing the long-term shoreline change rate data released in 2004, 2013, and 2020, there is some evidence that the hot spot is intensifying and expanding southwards as the SOF troughs have deepened and moved south, although these data are cumulative long-term averages that do not highlight year to year changes. Nevertheless, according to these data, between 2004 and 2020 the rate of erosion at SOF-N increased from -0.36 m/yr to -0.70 m/yr and the SOF-S from -0.79 m/yr to -1.00 m/yr. The areas affected have also expanded south by 100 m (*North Carolina Division Of Coastal Management*, 2021).

However, this hypothesis is complicated by the beach nourishment projects that occur in this region nearly every five years. A monitoring report conducted one year after the conclusion of the 2017 beach nourishment project in KH observed that that up to 60% of the sand volume loss occurred adjacent to the SOFs, although the authors cited challenges in calculating sediment volumes around the complex bathymetric structures (APTIM, 2019). The report concluded that future monitoring should investigate the impact of these SOFs on nourishment performance. The results of this study suggest that the SOFs act as a conduit for enhanced cross-shore exchange of sediment because, during periods of moderate wave heights and angles, enhanced flow velocities are directed offshore down the SOF edges and persist beyond the surf zone edge. During periods with strong longshore currents, the flow accelerates and meanders near the SOFs, which would further enhance sediment transport away from the SOF and contributing to the erosional hot spot. These findings emphasize the importance of both cross- and longshore transport on nearshore morphological evolution, supporting the conclusions of Thieler et al. (1995) and Gutierrez et al. (2005) at other sites.

The storm-induced wave forcing addressed in this research also affects shoreline change on an inter-annual to decadal time scale (Splinter et al., 2014). As climate change alters ocean temperatures, the intensity and duration of the Atlantic hurricane season may increase (Knutson et al., 2010; Walsh et al., 2016). This elevates the likelihood of sequential high-energy wave events (i.e., storm clusters) that inhibit beach recovery (Coco et al., 2014) and result in higher rates of shoreline recession (Dodet et al., 2019). Geologically inherited complex bathymetry produces variability in beach response and recovery, whereby influencing the pattern of barrier island transgression over time (Houser, 2012). With a more intense wave climate, complex nearshore bathymetric features will continue to drive spatially variable circulation patterns and affect erosional hot spots.

7 Summary and Conclusions

The influence of complex bathymetry on nearshore flow dynamics in an area with erosional hot spots was explored with a combination of remotely-sensed data and a numerical model. An X-Band Radar (XBR) system was deployed at the study site in Kitty Hawk, North Carolina,zfor nine days at the end of September, 2017. This period coincided with the passage of Hurricane Jose and Hurricane Maria, and these events were also simulated with a phase-resolving numerical model. In total, 24 simulations were performed: 3 selected times during storm events (J, M1, M2) that were also observed by XBR and 21 idealized simulations that explored a range of incident wave conditions. The event simulations were validated against XBR observations of wave breaking patterns, celerity, and representative wave height estimates.

The XBR observations were used to identify two zones of persistently high sea-surface backscatter during energetic periods ($H_s \geq 2$ m), indicative of strong offshore flows. Across a wide variety of incident wave conditions, the offshore flows re-emerged near shore oblique features (SOFs) and are concluded to be bathymetrically controlled rip currents. The wave-current interactions associated with these offshore flows roughens the sea surface, enabling them to be easily identified with XBR, and also increases the wave frequency in localized zones. The location of the offshore currents are also linked to the incident wave direction and the bathymetry. When waves approach the shoreline at a positive angle, the offshore currents flow along the northern SOF edges while when wave approach at a negative angle, the flows route along the southern edges. The rip currents result from wave breaking across the alongshore-varying bathymetry near the SOFs, supported by both XBR and numerical modeling data. Numerical simulations indicate that relative wave heights and wave setup also vary across the cross-section of the SOFs. When the wave field is oblique, a strong alongshore current represses offshore flows, and this current accelerates and meanders where the SOF contours pinch towards the shoreline.

Idealized simulations indicate that the complex bathymetry exerts a strong control over nearshore wave heights, refraction patterns, and mean currents. The XBR observations were used to identify morphologically-driven persistent offshore-directed flows just south of long-term erosional hot spots. Future studies, using other numerical models that simulate sediment movement and bed elevation change, could directly model the morphodynamic evolution of zones with complex bathymetry to evaluate impacts on erosional hot spot intensity and evolution. Persistent offshore flows and alongshore flow acceleration may exacerbate erosion and enhance the shoreline undulations at this site. This underscores the importance of both cross-shore and alongshore sediment transport on the nearshore morphology and shoreline evolution on sandy beaches with nearshore bathymetric features.

8 Data Availability Statement

All model inputs, radar data, processed model output data, and figure generation MATLAB codes used in this study are hosted on the Borealis data repository at Queen's University titled "Nearshore Flow Dynamics – SWASH and XBand Radar", via DOI: `https://borealisdata.ca/privateurl.xhtml?token=fa6593ed-6ea6-437c-8734-4711be8950c8` with data use license agreement CC-BY 4.0. This is a private link for reviewers only, and the public link will be included upon manuscript acceptance.

Acknowledgments

This research is supported by a Queen's School of Graduate Studies Doctoral Fellowship to LS and Natural Sciences and Engineering Research Council of Canada (NSERC) Discovery Grants to RPM and PKP. We thank the staff of the US Army Corps of Engineers Field Research Facility (FRF) and Engineer Research and Development Center (ERDC) Coastal and Hydraulics Laboratory (CHL) for help with field observations. We also thank a supportive group of coastal researchers for their insightful guidance, including Elora Oades from Queen's University, Dr. David Honegger from Oregon State University, and Dr. Spicer Bak as well as Dr. Kate Brodie from the U.S. Army Engineer Research and Development Center.

Acronyms

AWAC Acoustic Wave and Currents profiler
FRF Field Research Facility
KH Kitty Hawk
RIOS Radar Inlet Observation System
R.I. Return intensity of X-band radar
RMSE Root mean square error
SOF Shore-oblique feature
SOF-N Northern shore-oblique feature
SOF-S Southern shore-oblique feature
SWASH Simulating WAves till SHore
TKE Turbulent kinetic energy
XBR X-band radar

Notation

$\boldsymbol{\alpha_{ad}}$ Calibration coefficient, Eq. 12 from Streßer et al. (2022)
$\boldsymbol{C_p}$ Celerity of peak frequency waves [m/s]
$\boldsymbol{D_{50}}$ Median grain size [mm]
$\boldsymbol{\eta}$ Water surface elevation [m]
$\boldsymbol{f}$ Wave frequency [Hz]
γ Breaking index (0.78)
$\boldsymbol{g}$ Gravitational acceleration [m/s^2]]
$\boldsymbol{h}$ Water depth [m]
$\boldsymbol{H_p}$ Height of peak frequency waves [m]
$\boldsymbol{H_s}$ Significant wave height [m]
$\boldsymbol{k}$ Wave number [1/m]
$\boldsymbol{\lambda}$ Wavelength [m]
$\boldsymbol{\theta_m}$ Mean wave angle [°]
$\boldsymbol{\tau}$ Shear [N/m^2]
$\boldsymbol{T_p}$ Peak period [s]
$\boldsymbol{U}$ Depth-averaged mean velocity [m/s]
$\boldsymbol{U_{*cr}}$ Critical velocity [m/s]
$\boldsymbol{Q_b}$ Breaking parameter

Table 1. Wave conditions during the hindcast simulated event (J, M1, M2) including significant wave height (H_s), peak period (T_p), total water level (η), mean wave angle relative to perpendicular of the study site's mean shoreline (θ_m), and peak directional spreading (σ_p).

Label	UTC	H_s [m]	T_p [s]	η [m]	θ_m [°]	σ_p [°]
J	19-Sep-2017 20:00:00	2.8	10.0	0.9	3.9	36.3
M1	27-Sep-2017 09:00:00	4.0	13.3	0.7	16.9	23.2
M2	28-Sep-2017 02:00:00	2.6	10.3	0.8	-37.1	58.5

Measured at the FRF's 11 m AWAC.

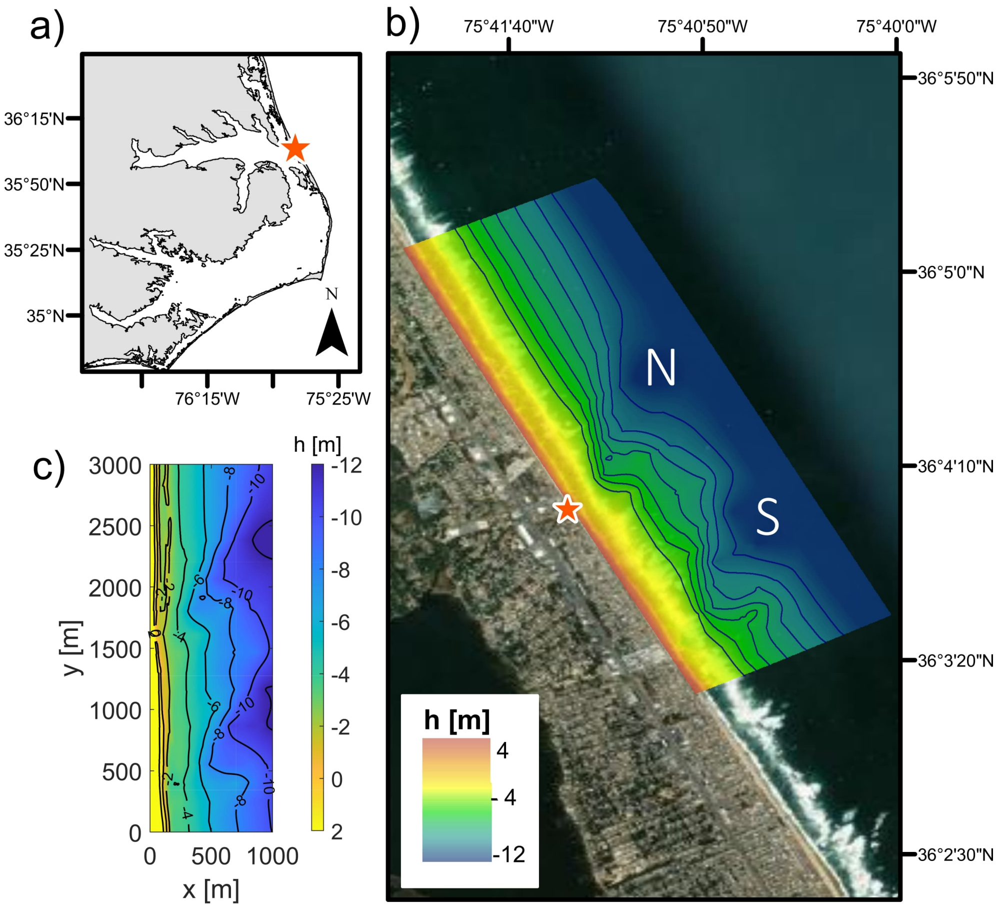

Figure 1. (a) Study region location within the Outer Banks, (b) June 2017 bathymetry measured offshore of Kitty Hawk, North Carolina where the red star represents the XBR location and labels N and S identify the lcoations of SOF-N and SOF-S, respectively, and (c) rotated bathymetric grid used for numerical modeling.

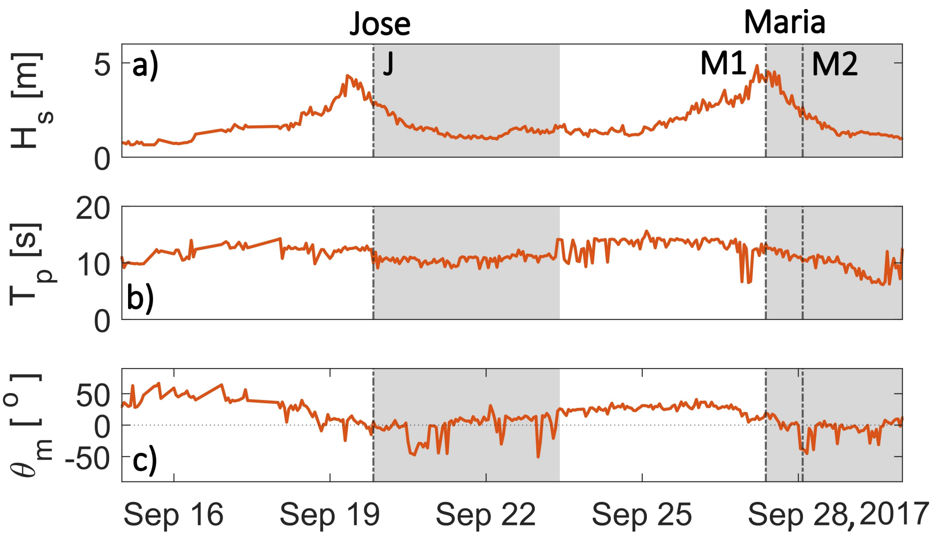

Figure 2. Wave conditions throughout the study period: (a) significant wave height (H_s), (b) peak period (T_p), and (c) mean wave angle relative to perpendicular of the mean shoreline (θ_m). Wave angles are described as going towards, meaning positive values indicate an approach angle north of shore-perpendicular and negative values indicate an approach angle south of shore-perpendicular. Vertical dashed lines indicate the simulated hours during Hurricanes Jose and Maria (J, M1, M2) and shaded regions are periods observed by XBR.

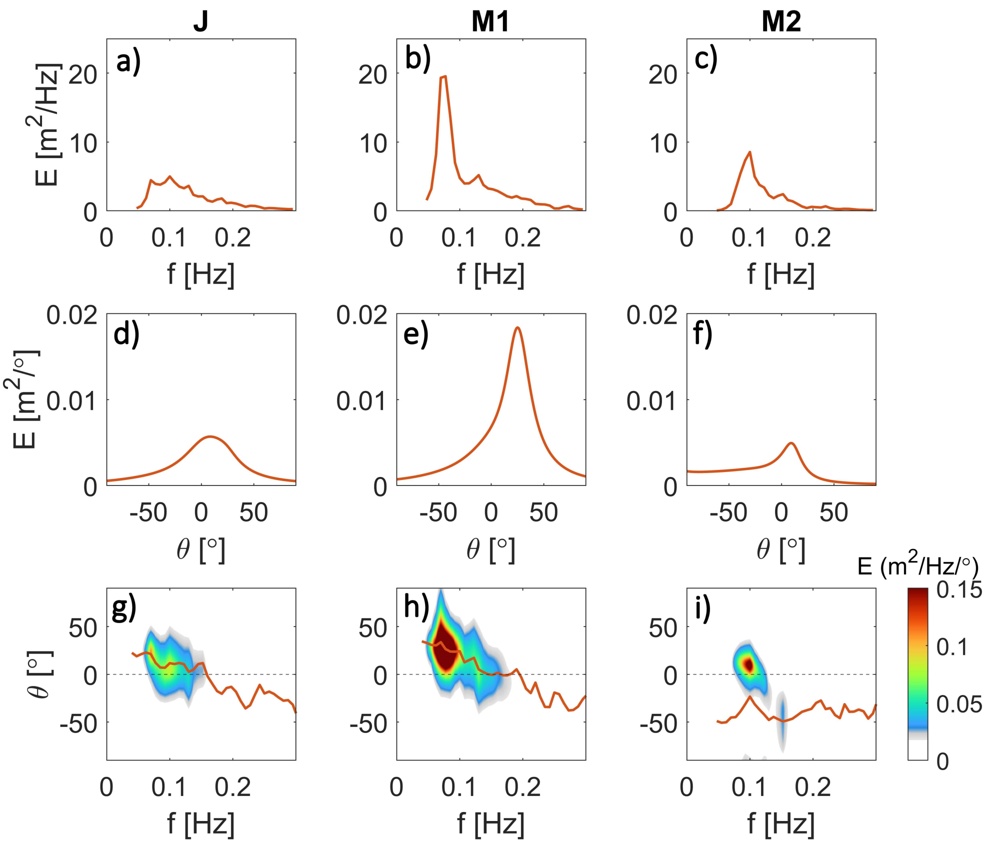

Figure 3. Wave spectra for time periods (left column) J, (middle column) M1, and (right column) M2: (a, b, c) energy-density, (d, e, f) directional distribution of wave angles, and (g, h, i) directional energy-density spectra used to force simulations at the offshore boundary. Red lines in (g, h, i) are the mean direction per frequency calculated from Kuik et al. (1988). Wave angles are described as going towards, meaning positive values indicate an approach angle north of shore-perpendicular and negative values indicate an approach angle south of shore-perpendicular.

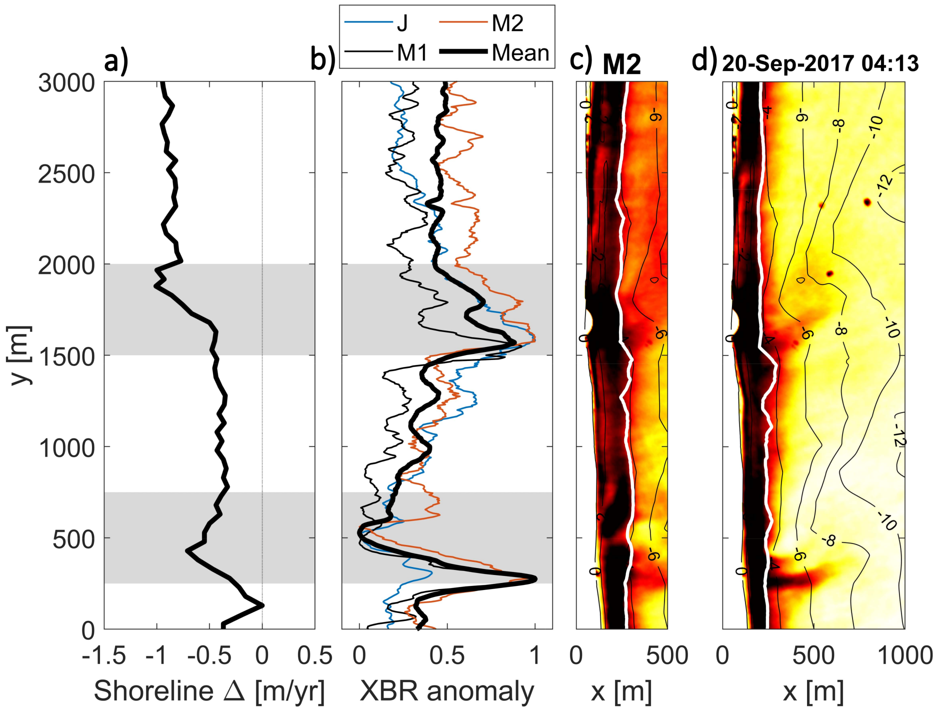

Figure 4. Alongshore variability in: (a) the long-term average shoreline change rate over 1940-2016 with shaded regions indicating the troughs of SOF-N and SOF-s;(b) XBR backscatter intensity anomalies for J (blue line), M1 (black line), M2 (orange line), and the mean during the observation period (thick black line); (c) time-averaged XBR backscatter return intensity (R.I.) during event M2 with the white lines indicating the corresponding XBR estimated offshore edge of the surf zone; and (d) time-averaged XBR backscatter during a moderate energy event (H_s = 2.3 m) on September 20, 2017 at 04:13 UTC.

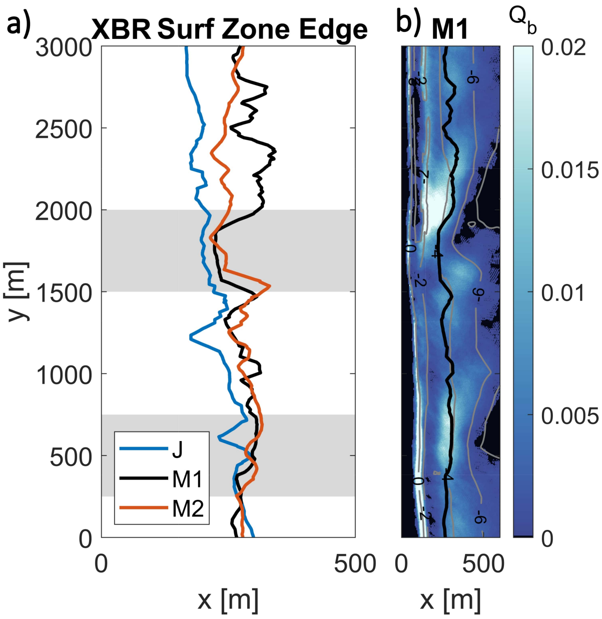

Figure 5. Surf zone detection from XBR observations and model: (a) XBR measurements of the cross-shore location of the offshore surf zone edge during event J (blue line), M1 (black line), and M2 (orange line) with shaded regions indicating the SOF troughs; (b) XBR-derived M1 surf zone edge (black line) over the simulated fraction of breaking waves (Q_b) for M1.

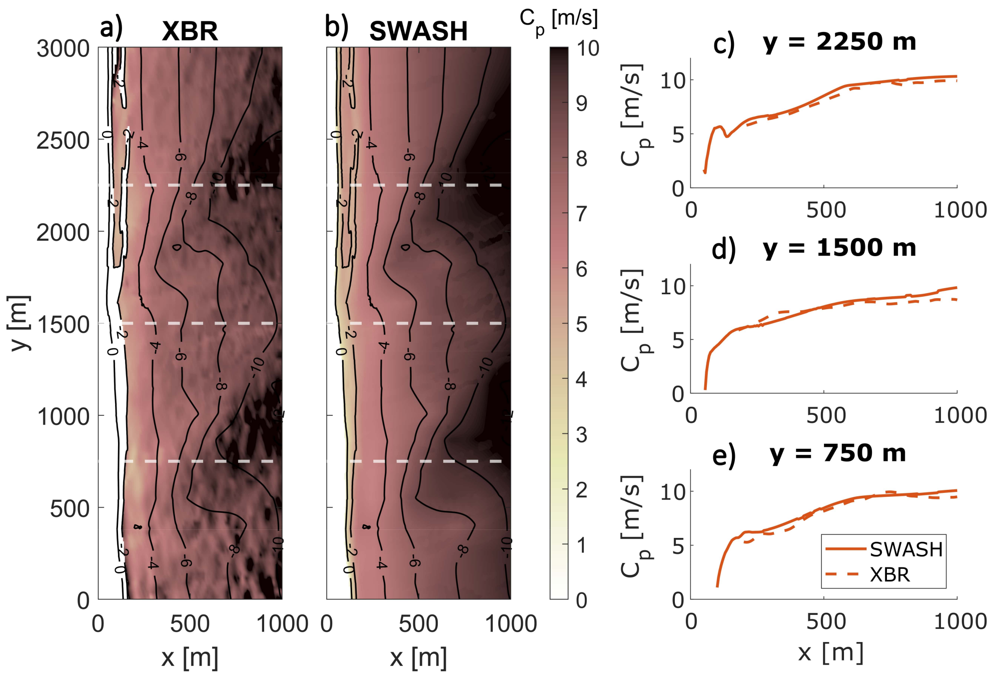

Figure 6. XBR observations and model results of wave celerity at the peak frequency (C_p) during M2: (a) XBR observations in areas deeper than 2 m, (b) SWASH results, and (c, d, e) cross-shore transects of modeling results (solid lines) and XBR observations (dashed lines) at alongshore locations (c) y = 2250 m, (d) y = 1500 m, and (e) y = 750 m. White dashed lines in (a) and (b) indicate the cross-shore transect locations.

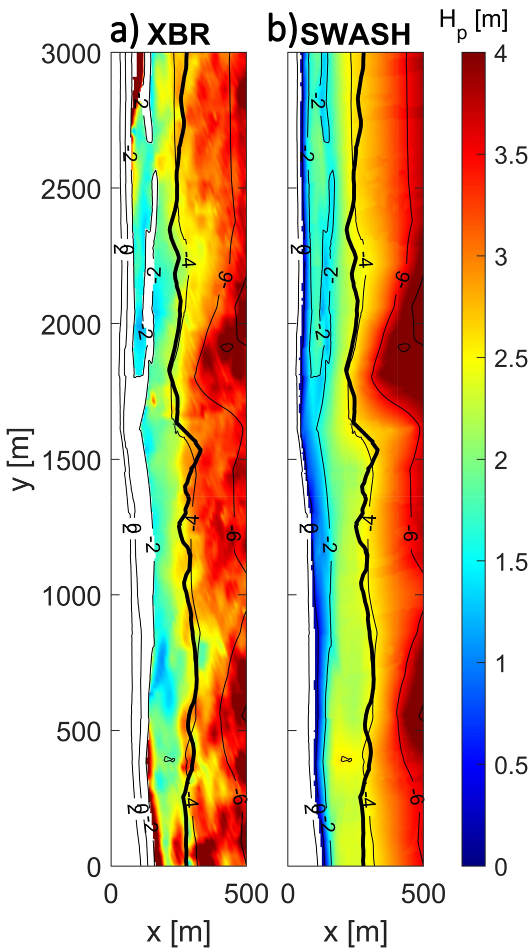

Figure 7. Estimates of the peak wave height (H_p) for event M2 from (a) XBR observations and (b) modelling results. Solid black lines in (a) and (b) represent the XBR-measured surf zone edge of M2.

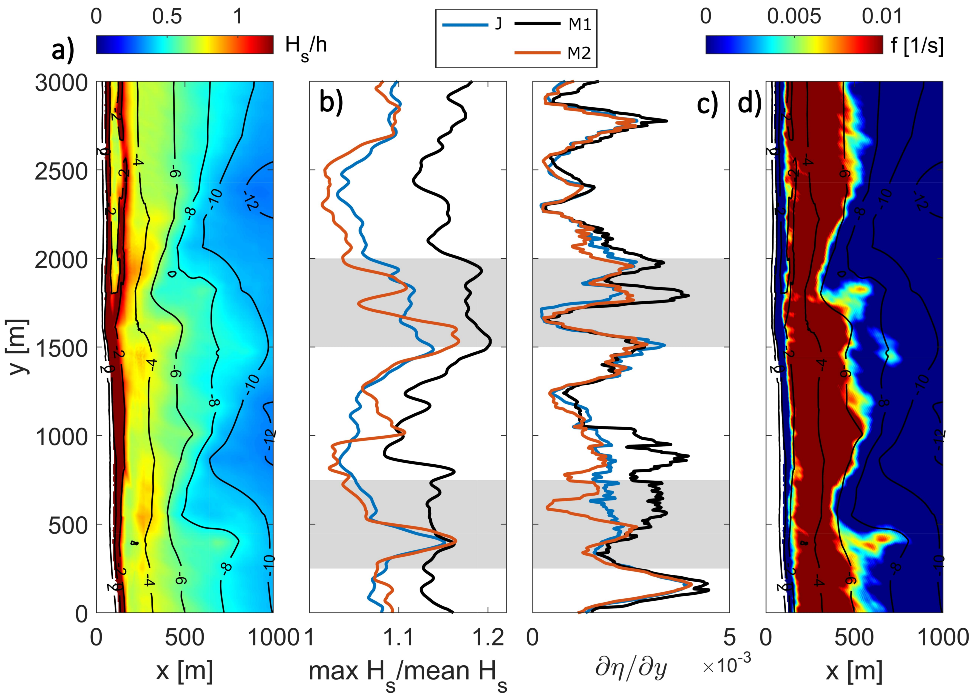

Figure 8. Wave height estimates from numerical simulations: (a) the spatial distribution of relative wave heights (H_s/h) during M1, (b) maximum H_s divided by mean H_s at each alongshore location for J (blue line), M1 (black line), and M2 (orange line), (c) maximum alongshore gradient in setup, and (d) saturated frequency map during M1. Gray shaded regions in (b) and (c) indicate the approximate bounds of the shore-oblique troughs.

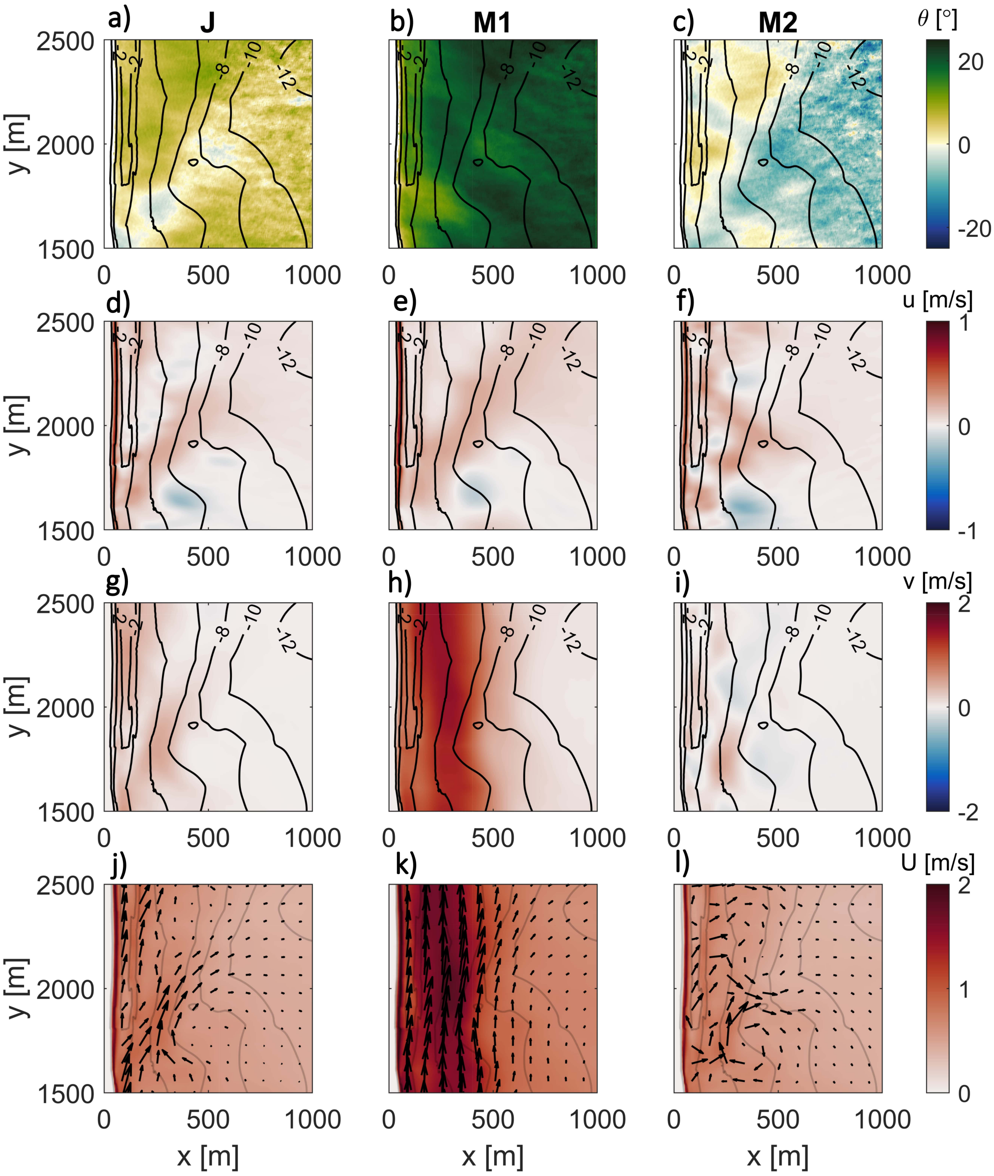

Figure 9. Flow dynamics around the northern shore-oblique feature between y = 1500 m – 2500 m for time periods (left column) J, (middle column) M1, and (right column) M2. Flow dynamics displayed include: (a, b, c) wave angle (θ) relative to shore-perpendicular, (d, e, f) cross-shore velocity (u), (g, h, i) alongshore velocity (v), and (j, k, l) overall depth averaged current velocity (U).

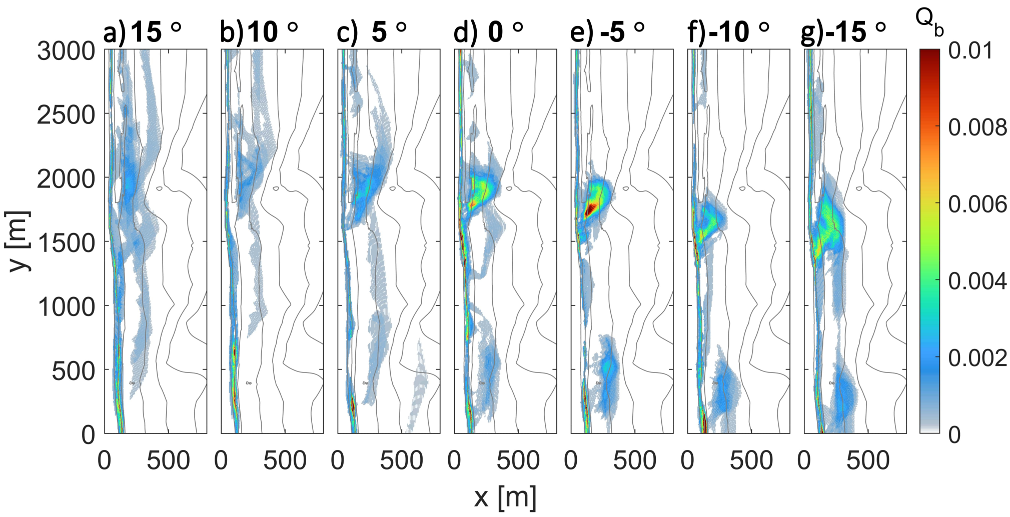

Figure 10. Fraction of breaking waves (Q_b) calculated from $H_s = 3$ m idealized simulations with various incident peak wave angles (θ_p): (a) 15°, (b) 10°, (c) 5°, (d) 0°, (e) -5°, (f) -10°, and (g) -15°.

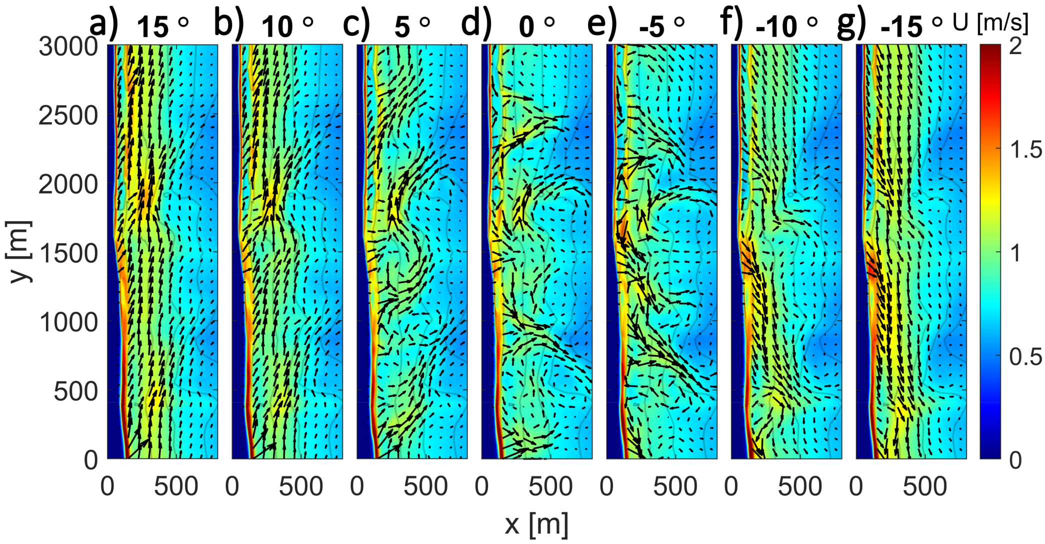

Figure 11. Depth-averaged current velocities (U) calculated from $H_s = 3$ m idealized simulations with various incident peak wave angles (θ_p): (a) 15°, (b) 10°, (c) 5°, (d) 0°, (e) -5°, (f) -10°, and (g) -15°.

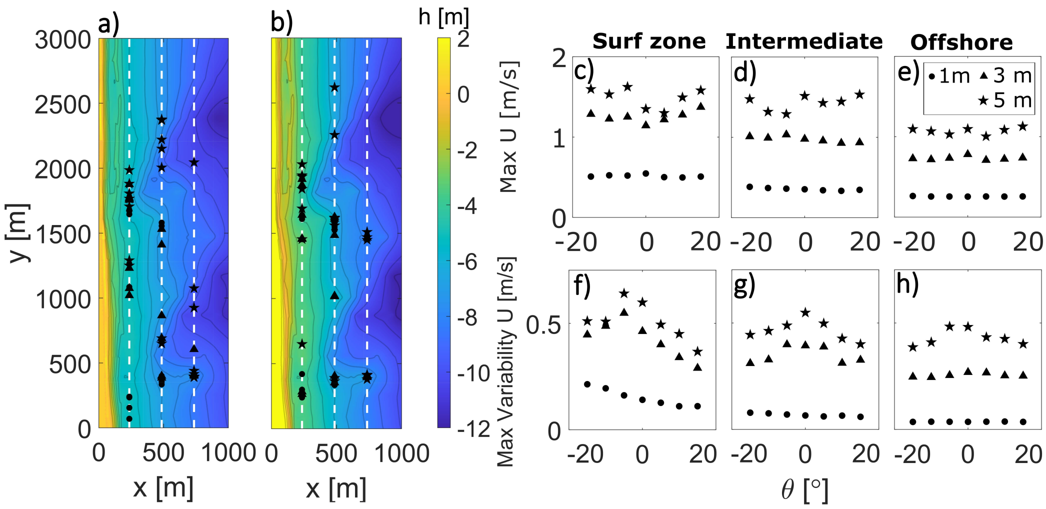

Figure 12. Locations of maximum U (a) and locations of maximum variability of U (b) during a variety of incident wave angles and significant wave heights (H_s), where circles represent an incoming H_s of 1 m, triangles represent H_s of 3 m, and stars represent H_s of 5 m. Quantified influence of incoming wave angle (θ) and H_s on maximum U (c-e) and the variability of U (f-h) in the surf, intermediate, and offshore zones. Cross-shore locations of the surf, intermediate, and offshore zones are depicted in (a) and (b) as white dashed lines.

References

APTIM. (2017). *2017 Town of Kitty Hawk, Town of Kill Devil Hills, NC beach profile survey report* (Tech. Rep.). 4038 Masonboro Loop Road, Wilmington, NC 28409: APTIM Coastal Planning and Engineering of North Carolina, Inc.

APTIM. (2019). *Town of Kitty Hawk and Kill Devil Hills, North Carolina 2018 shoreline change and volume change monitoring report* (Tech. Rep.). 4038 Masonboro Loop Road, Wilmington, NC 28409: APTIM Coastal Planning and Engineering of North Carolina, Inc.

Baker, C. M., Moulton, M., Raubenheimer, B., Elgar, S., & Kumar, N. (2021). Modeled three-dimensional currents and eddies on an alongshore-variable barred beach. *Journal of Geophysical Research: Oceans*, *126*(7), e2020JC016899.

Barrett, G., & Houser, C. (2012). Identifying hotspots of rip current activity using wavelet analysis at Pensacola Beach, Florida. *Physical Geography*, *33*(1), 32–49.

Boss, S. K., Hoffman, C. W., & Cooper, B. (2002). Influence of fluvial processes on the Quaternary geologic framework of the continental shelf, North Carolina, USA. *Marine Geology*, *183*(1-4), 45–65.

Bowen, A. J. (1969). Rip currents: 1. theoretical investigations. *Journal of Geophysical Research*, *74*(23), 5467–5478.

Brander, R. W., & Short, A. D. (2001). Flow kinematics of low-energy rip current systems. *Journal of Coastal Research*, 468–481.

Brodie, K. L., Palmsten, M. L., Hesser, T. J., Dickhudt, P. J., Raubenheimer, B., Ladner, H., & Elgar, S. (2018). Evaluation of video-based linear depth inversion performance and applications using altimeters and hydrographic surveys in a wide range of environmental conditions. *Coastal Engineering*, *136*, 147–160.

Browder, A. G., & McNinch, J. E. (2006). Linking framework geology and nearshore morphology: correlation of paleo-channels with shore-oblique sandbars and gravel outcrops. *Marine Geology*, *231*(1-4), 141–162.

Castelle, B., Scott, T., Brander, R., & McCarroll, R. (2016). Rip current types, circulation and hazard. *Earth-Science Reviews*, *163*, 1–21.

Catalán, P. A., Haller, M. C., & Plant, W. J. (2014). Microwave backscattering from surf zone waves. *Journal of Geophysical Research: Oceans*, *119*(5), 3098–3120.

Coco, G., Senechal, N., Rejas, A., Bryan, K. R., Capo, S., Parisot, J., … MacMahan, J. H. (2014). Beach response to a sequence of extreme storms. *Geomorphology*, *204*, 493–501.

Colman, S. M., Halka, J. P., HOBBS III, C., Mixon, R. B., & Foster, D. S. (1990). Ancient channels of the susquehanna river beneath chesapeake bay and the delmarva peninsula. *Geological Society of America Bulletin*, *102*(9), 1268–1279.

Culver, S. J., Pre, C. A. G., Mallinson, D. J., Riggs, S. R., Corbett, D. R., Foley, J., … others (2007). Late holocene barrier island collapse: Outer banks, north carolina, usa. *The Sedimentary Record*, *5*(4), 4–8.

Dalrymple, R. A. (1978). Rip currents and their causes. In *Coastal engineering 1978* (pp. 1414–1427).

Dalrymple, R. A., MacMahan, J. H., Reniers, A. J., & Nelko, V. (2011). Rip currents. *Annual Review of Fluid Mechanics*, *43*, 551–581.

da Silva, R. F., Hansen, J. E., Lowe, R. J., Rijnsdorp, D. P., & Buckley, M. L. (2023). Dynamics of the wave-driven circulation in the lee of nearshore reefs. *Journal of Geophysical Research: Oceans*, *128*(3), e2022JC019013.

Dean, R. G., & Dalrymple, R. A. (1991). *Water wave mechanics for engineers and scientists* (Vol. 2). world scientific publishing company.

Dodet, G., Castelle, B., Masselink, G., Scott, T., Davidson, M., Floc'h, F., … Suanez, S. (2019). Beach recovery from extreme storm activity during the

2013–14 winter along the atlantic coast of europe. *Earth Surface Processes and Landforms*, *44*(1), 393–401.

Dusek, G., & Seim, H. (2013a). A probabilistic rip current forecast model. *Journal of Coastal Research*, *29*(4), 909–925.

Dusek, G., & Seim, H. (2013b). Rip current intensity estimates from lifeguard observations. *Journal of coastal research*, *29*(3), 505–518.

Dusek, G., Seim, H., Hanson, J., & Elder, D. (2011). Analysis of rip current rescues at kill devil hills, north carolina. *Rip Currents: Beach Safety, Physical Oceanography and Wave Modeling.*.

Engle, J. (2002). Formulation of a rip current predictive index using rescue data jason engle*, james macmahan, robert j. thieke, daniel m hanes and robert g dean* graduate assistant, department of civil and coastal engineering, university of florida phone:(352) 392-9537 ext-1410; email: engle@ coastal. ufl. edu. In *2002 national conference on beach preservation technology. florida shore & beach preservation association, citeseer* (Vol. 285).

Fenton, J. D., & McKee, W. (1990). On calculating the lengths of water waves. *Coastal Engineering*, *14*(6), 499–513.

Gallagher, E. L., Elgar, S., & Guza, R. (1998). Observations of sand bar evolution on a natural beach. *Journal of Geophysical Research: Oceans*, *103*(C2), 3203–3215.

Garnier, R., Falqués, A., Calvete, D., Thiebot, J., & Ribas, F. (2013). A mechanism for sandbar straightening by oblique wave incidence. *Geophysical Research Letters*, *40*(11), 2726–2730.

Gomes, E. R., Mulligan, R. P., Brodie, K. L., & McNinch, J. E. (2016). Bathymetric control on the spatial distribution of wave breaking in the surf zone of a natural beach. *Coastal Engineering*, *116*, 180–194.

Green, M. O., Vincent, C. E., & Trembanis, A. C. (2004). Suspension of coarse and fine sand on a wave-dominated shoreface, with implications for the development of rippled scour depressions. *Continental Shelf Research*, *24*(3), 317–335.

Gutierrez, B. T., Voulgaris, G., & Thieler, E. R. (2005). Exploring the persistence of sorted bedforms on the inner-shelf of wrightsville beach, north carolina. *Continental Shelf Research*, *25*(1), 65–90.

Guza, R., Thornton, E., & Christensen Jr, N. (1986). Observations of steady longshore currents in the surf zone. *Journal of physical oceanography*, *16*(11), 1959–1969.

Haller, M. C., Dalrymple, R. A., & Svendsen, I. A. (2002). Experimental study of nearshore dynamics on a barred beach with rip channels. *Journal of Geophysical Research: Oceans*, *107*(C6), 14–1.

Haller, M. C., Honegger, D., & Catalan, P. A. (2014). Rip current observations via marine radar. *Journal of waterway, port, coastal, and ocean engineering*, *140*(2), 115–124.

Hayes, M. (1979). *Barrier island morphology as a function of tidal and wave regime. In: Leatherman SP (ed), Barrier Islands: From the Gulf of St. Lawerence to the Gulf of Mexico.* Academic Press, New York.

Hedges, T. (1976). An empirical modification to linear wave theory. *Proceedings of the Institution of Civil Engineers*, *61*(3), 575–579.

Holman, R. A., & Bergsma, E. W. (2021). Updates to and performance of the cbathy algorithm for estimating nearshore bathymetry from remote sensing imagery. *Remote Sensing*, *13*(19), 3996.

Holman, R. A., Plant, N., & Holland, T. (2013b). cbathy: A robust algorithm for estimating nearshore bathymetry. *Journal of geophysical research: Oceans*, *118*(5), 2595–2609.

Holman, R. A., & Sallenger, A. H. (1993). Sand bar generation: a discussion of the duck experiment series. *Journal of Coastal Research*, 76–92.

Holman, R. A., Symonds, G., Thornton, E. B., & Ranasinghe, R. (2006). Rip spacing and persistence on an embayed beach. *Journal of Geophysical Research: Oceans*, *111*(C1).

Honegger, D. A., Haller, M. C., & Holman, R. A. (2019). High-resolution bathymetry estimates via x-band marine radar: 1. beaches. *Coastal Engineering*, *149*, 39–48.

Houser, C. (2012). Feedback between ridge and swale bathymetry and barrier island storm response and transgression. *Geomorphology*, *173*, 1–16.

Houser, C., Hapke, C., & Hamilton, S. (2008). Controls on coastal dune morphology, shoreline erosion and barrier island response to extreme storms. *Geomorphology*, *100*(3-4), 223–240.

Houser, C., Wernette, P., Trimble, S., & Locknick, S. (2020). Rip currents. *Sandy beach morphodynamics*, 255–276.

Humberston, J., Lippmann, T., & McNinch, J. (2019). Observations of wave influence on alongshore ebb-tidal delta morphodynamics at Oregon Inlet, NC. *Marine Geology*, *418*, 106040.

Kemp, A. C., Kegel, J. J., Culver, S. J., Barber, D. C., Mallinson, D. J., Leorri, E., ... others (2017). Extended late holocene relative sea-level histories for north carolina, usa. *Quaternary Science Reviews*, *160*, 13–30.

Knutson, T. R., McBride, J. L., Chan, J., Emanuel, K., Holland, G., Landsea, C., ... Sugi, M. (2010). Tropical cyclones and climate change. *Nature geoscience*, *3*(3), 157–163.

Komar, P. D., & McDougal, W. G. (1988). Coastal erosion and engineering structures: the oregon experience. *Journal of Coastal Research*, 77–92.

Kuik, A., Van Vledder, G. P., & Holthuijsen, L. (1988). A method for the routine analysis of pitch-and-roll buoy wave data. *Journal of physical oceanography*, *18*(7), 1020–1034.

Kumar, N., & Feddersen, F. (2017). The effect of stokes drift and transient rip currents on the inner shelf. part i: No stratification. *Journal of Physical Oceanography*, *47*(1), 227–241.

Kumar, N., Lerczak, J. A., Xu, T., Waterhouse, A. F., Thomson, J., Terrill, E. J., ... others (2021). The inner-shelf dynamics experiment. *Bulletin of the American Meteorological Society*, *102*(5), E1033–E1063.

Kumar, N., Voulgaris, G., & Warner, J. C. (2011). Implementation and modification of a three-dimensional radiation stress formulation for surf zone and rip-current applications. *Coastal Engineering*, *58*(12), 1097–1117.

Larson, M., & Kraus, N. C. (1994). Temporal and spatial scales of beach profile change, duck, north carolina. *Marine Geology*, *117*(1-4), 75–94.

Leatherman, S., & Fletemeyer, J. (2011). *Rip currents: Beach safety, physical oceanography, and wave modeling.* CRC Press.

Lippmann, T., & Holman, R. (1989). Quantification of sand bar morphology: A video technique based on wave dissipation. *Journal of Geophysical Research: Oceans*, *94*(C1), 995–1011.

Lippmann, T., Holman, R. A., & Hathaway, K. (1993). Episodic, nonstationary behavior of a double bar system at Duck, North Carolina, USA, 1986–1991. *Journal of Coastal Research*, 49–75.

List, J. H., Farris, A. S., & Sullivan, C. (2006). Reversing storm hotspots on sandy beaches: Spatial and temporal characteristics. *Marine Geology*, *226*(3-4), 261–279.

Long, J. W., & Özkan-Haller, H. T. (2005). Offshore controls on nearshore rip currents. *Journal of geophysical research: oceans*, *110*(C12).

Longuet-Higgins, M. S. (1970). Longshore currents generated by obliquely incident sea waves: 1. *Journal of geophysical research*, *75*(33), 6778–6789.

Longuet-Higgins, M. S., & Stewart, R. (1964). Radiation stresses in water waves; a physical discussion, with applications. In *Deep sea research and oceanographic*

abstracts (Vol. 11, pp. 529–562).
Lygre, A., & Krogstad, H. E. (1986). Maximum entropy estimation of the directional distribution in ocean wave spectra. *Journal of Physical Oceanography*, *16*(12), 2052–2060.
Lyzenga, D. R. (1991). Interaction of short surface and electromagnetic waves with ocean fronts. *Journal of Geophysical Research: Oceans*, *96*(C6), 10765–10772.
MacMahan, J., Brown, J., Brown, J., Thornton, E., Reniers, A., Stanton, T., ... others (2010). Mean lagrangian flow behavior on an open coast rip-channeled beach: A new perspective. *Marine Geology*, *268*(1-4), 1–15.
MacMahan, J., Thornton, E. B., & Reniers, A. J. (2006). Rip current review. *Coastal engineering*, *53*(2-3), 191–208.
MacMahan, J., Thornton, E. B., Stanton, T. P., & Reniers, A. J. (2005). Ripex: Observations of a rip current system. *Marine Geology*, *218*(1-4), 113–134.
Magne, R., Belibassakis, K., Herbers, T. H., Ardhuin, F., O'Reilly, W. C., & Rey, V. (2007). Evolution of surface gravity waves over a submarine canyon. *Journal of Geophysical Research: Oceans*, *112*(C1).
Mallinson, D., Burdette, K., Mahan, S., & Brook, G. (2008). Optically stimulated luminescence age controls on late pleistocene and holocene coastal lithosomes, north carolina, usa. *Quaternary Research*, *69*(1), 97–109.
McNinch, J. E. (2004). Geologic control in the nearshore: shore-oblique sandbars and shoreline erosional hotspots, Mid-Atlantic Bight, USA. *Marine Geology*, *211*(1-2), 121–141.
McNinch, J. E. (2007). Bar and swash imaging radar (basir): A mobile x-band radar designed for mapping nearshore sand bars and swash-defined shorelines over large distances. *Journal of Coastal Research*, *23*(1), 59–74.
McNinch, J. E., Brodie, K. L., & Slocum, R. K. (2012). Radar Inlet Observing System (RIOS): Continuous remote sensing of waves, currents, and bathymetry at tidal inlets. In *Oceans* (pp. 1–8).
McNinch, J. E., & Miselis, J. L. (2012). Geology metrics for predicting shoreline change using seabed and sub-bottom observations from the surf zone and nearshore. *Sediments, Morphology and Sedimentary Processes on Continental Shelves: Advances in Technologies, Research, and Applications*, 99–119.
Moulton, M., Elgar, S., Raubenheimer, B., Warner, J. C., & Kumar, N. (2017). Rip currents and alongshore flows in single channels dredged in the surf zone. *Journal of Geophysical Research: Oceans*, *122*(5), 3799–3816.
Moulton, M., Suanda, S. H., Garwood, J. C., Kumar, N., Fewings, M. R., & Pringle, J. M. (2023). Exchange of plankton, pollutants, and particles across the nearshore region. *Annual Review of Marine Science*, *15*, 167–202.
Mulligan, R. P., Gomes, E. R., Miselis, J. L., & McNinch, J. E. (2019a). Non-hydrostatic numerical modelling of nearshore wave transformation over shore-oblique sandbars. *Estuarine, Coastal and Shelf Science*, *219*, 151–160.
Mulligan, R. P., Mallinson, D. J., Clunies, G. J., Rey, A., Culver, S. J., Zaremba, N., ... Mitra, S. (2019b). Estuarine responses to long-term changes in inlets, morphology, and sea level rise. *Journal of Geophysical Research: Oceans*, *124*(12), 9235–9257.
North Carolina Division Of Coastal Management. (2021). `https://www.deq.nc.gov/about/divisions/coastal-management/coastal-management-oceanfront-shorelines/oceanfront-construction-setback-erosion-rate`. 400 Commerce Avenue Morehead City, NC 28557. (Accessed: 2023-08-10)
Oades, E. M., Mulligan, R., & Palmsten, M. (2023). Evaluation of nearshore bathymetric inversion algorithms using camera observations and synthetic numerical input of surface waves during storms. *Coastal Engineering*, 104338.
O'Dea, A., Kumar, N., & Haller, M. C. (2021). Simulations of the surf zone eddy field and cross-shore exchange on a nonidealized bathymetry. *Journal of Geo-*

physical Research: Oceans, *126*(5), e2020JC016619.
Pattiaratchi, C., Olsson, D., Hetzel, Y., & Lowe, R. (2009). Wave-driven circulation patterns in the lee of groynes. *Continental Shelf Research*, *29*(16), 1961–1974.
Plant, W. J., Keller, W. C., Hayes, K., & Chatham, G. (2010). Normalized radar cross section of the sea for backscatter: 1. mean levels. *Journal of Geophysical Research: Oceans*, *115*(C9).
Raubenheimer, B., Guza, R., & Elgar, S. (1996). Wave transformation across the inner surf zone. *Journal of Geophysical Research: Oceans*, *101*(C11), 25589–25597.
Riggs, S. R., Cleary, W. J., & Snyder, S. W. (1995). Influence of inherited geologic framework on barrier shoreface morphology and dynamics. *Marine geology*, *126*(1-4), 213–234.
Riggs, S. R., York, L. L., Wehmiller, J. F., & Snyder, S. W. (1992). Depositional patterns resulting from high-frequency quaternary sea-level fluctuations in northeastern north carolina. *Quaternary Coasts of the United States: Marine and Lacustrine Systems*.
Safak, I., List, J. H., Warner, J. C., & Schwab, W. C. (2017). Persistent shoreline shape induced from offshore geologic framework: Effects of shoreface connected ridges. *Journal of Geophysical Research: Oceans*, *122*(11), 8721–8738.
Sallenger, A. H., Doran, K. S., & Howd, P. A. (2012). Hotspot of accelerated sea-level rise on the atlantic coast of north america. *Nature Climate Change*, *2*(12), 884–888.
Schupp, C. A., McNinch, J. E., & List, J. H. (2006). Nearshore shore-oblique bars, gravel outcrops, and their correlation to shoreline change. *Marine Geology*, *233*(1-4), 63–79.
Schwab, W. C., Thieler, E. R., Allen, J. R., Foster, D. S., Swift, B. A., & Denny, J. F. (2000). Influence of inner-continental shelf geologic framework on the evolution and behavior of the barrier-island system between fire island inlet and shinnecock inlet, long island, new york. *Journal of Coastal Research*, 408–422.
Schwartz, R. K., & Birkemeier, W. A. (2004). Sedimentology and morphodynamics of a barrier island shoreface related to engineering concerns, outer banks, nc, usa. *Marine Geology*, *211*(3-4), 215–255.
Short, A. (2007). Australian rip systems–friend or foe? *Journal of Coastal Research*, 7–11.
Smit, P., Zijlema, M., & Stelling, G. (2013). Depth-induced wave breaking in a non-hydrostatic, near-shore wave model. *Coastal Engineering*, *76*, 1–16.
Snedden, J. W., Tillman, R. W., Kreisa, R. D., Schweller, W. J., Culver, S. J., & Winn, R. D. (1994). Stratigraphy and genesis of a modern shoreface-attached sand ridge, peahala ridge, new jersey. *Journal of Sedimentary Research*, *64*(4b), 560–581.
Sonu, C. J. (1972). Field observation of nearshore circulation and meandering currents. *Journal of Geophysical Research*, *77*(18), 3232–3247.
Splinter, K. D., & Palmsten, M. L. (2012). Modeling dune response to an east coast low. *Marine Geology*, *329*, 46–57.
Splinter, K. D., Turner, I. L., Davidson, M. A., Barnard, P., Castelle, B., & Oltman-Shay, J. (2014). A generalized equilibrium model for predicting daily to interannual shoreline response. *Journal of Geophysical Research: Earth Surface*, *119*(9), 1936–1958.
Streßer, M., Horstmann, J., & Baschek, B. (2022). Surface wave and roller dissipation observed with shore-based doppler marine radar. *Journal of Geophysical Research: Oceans*, *127*(8), e2022JC018437.
Suanda, S. H., & Feddersen, F. (2015). A self-similar scaling for cross-shelf exchange driven by transient rip currents. *Geophysical Research Letters*, *42*(13), 5427–5434.

Svendsen, I. A. (1984). Mass flux and undertow in a surf zone. *Coastal engineering*, *8*(4), 347–365.

Szczyrba, L. D., Mulligan, R. P., Humberston, J. L., Bak, A. S., McNinch, J. E., & Pufahl, P. K. (2023b). Nearshore wave angles and directional variability during storm events. *Coastal Engineering*, 104372.

Szczyrba, L. D., Mulligan, R. P., Pufahl, P. K., Humberston, J. L., & McNinch, J. E. (2023a). Morphodynamic link between shore-oblique bars and erosional hotspots. *Coastal Sediments 2023: The Proceedings of the Coastal Sediments 2023*, 1907–1922.

Takewaka, S., & Yamakawa, T. (2011). Rip current observation with x-band radar. *Coastal Engineering Proceedings*(32), 43–43.

Thieler, E. R., Brill, A. L., Cleary, W. J., Hobbs III, C. H., & Gammisch, R. A. (1995). Geology of the wrightsville beach, north carolina shoreface: Implications for the concept of shoreface profile of equilibrium. *Marine Geology*, *126*(1-4), 271–287.

Turner, I. L., Whyte, D., Ruessink, B., & Ranasinghe, R. (2007). Observations of rip spacing, persistence and mobility at a long, straight coastline. *Marine Geology*, *236*(3-4), 209–221.

Voulgaris, G., Kumar, N., & Warner, J. C. (2011). Methodology for prediction of rip currents using a three-dimensional numerical, coupled, wave current model. In *First international rip current symposium* (pp. 87–105).

Walsh, K. J., McBride, J. L., Klotzbach, P. J., Balachandran, S., Camargo, S. J., Holland, G., ... others (2016). Tropical cyclones and climate change. *Wiley Interdisciplinary Reviews: Climate Change*, *7*(1), 65–89.

Wernette, P., & Houser, C. (2022). evidence for geologic control of rip channels along prince edward island, canada. *Physical Geography*, *43*(2), 145–162.

Wright, L. D., & Short, A. D. (1984). Morphodynamic variability of surf zones and beaches: a synthesis. *Marine geology*, *56*(1-4), 93–118.

Zijlema, M. (2020). Computation of free surface waves in coastal waters with swash on unstructured grids. *Computers & Fluids*, *213*, 104751.

Zijlema, M., Stelling, G., & Smit, P. (2011). SWASH: An operational public domain code for simulating wave fields and rapidly varied flows in coastal waters. *Coastal Engineering*, *58*(10), 992–1012.

Zijlema, M., & Stelling, G. S. (2005). Further experiences with computing non-hydrostatic free-surface flows involving water waves. *International journal for numerical methods in fluids*, *48*(2), 169–197.

Nearshore flow dynamics over shore-oblique bathymetric features during storm wave conditions

L. Szczyrba, R.P. Mulligan, P. Pufahl, J. Humberston, J. McNinch

[1,2]Department of Civil Engineering, Queen's University
[1,3]Department of Geological Sciences and Geological Engineering, Queen's University
[4]Sandia National Laboratories
[5]Coastal and Hydraulics Laboratory, US Army Engineer Research and Development Center

Key Points:

- Radar and numerical modeling indicate variability in surf zone width and wave height
- Offshore-directed flows occur in a region with shore-oblique sand bars and erosional hot spots
- Morphologic influence and directional variability are quantified with idealized model simulations

Corresponding author: Laura Szczyrba, `20LDS@queensu.ca`

Abstract

Shore-oblique bathymetric features occur around the world and have been statistically correlated with enhanced shoreline retreat on sandy beaches. However, the physical mechanisms that explain a causal relationship are not well understood. In this study, radar remote sensing observations and results from a phase-resolved numerical model explore how complex morphology alters nearshore hydrodynamics. Observations at selected times during high-energy storm events as well as a suite of idealized simulations indicate that shore-oblique features induce strong spatial variations in the water surface elevation and wave breaking patterns. Re-emergent offshore flows and longshore current accelerations occur near the apex of the oblique nearshore features. The results suggest that complex bathymetric morphology exerts a powerful control on nearshore hydrodynamics and increases the potential for enhanced cross-shore and alongshore sediment transport, thus contributing to localized erosional zones.

Plain Language Summary

Near the shoreline, underwater topography is affected by sea level, waves, currents, tides, and geological characteristics. Typically, sandbars are oriented parallel to the coastline, but shore-oblique sandbars have also been identified around the world. In many instances, these oblique features have been correlated with zones of erosion, however the explanation for this statistical relationship is not fully understood. In this study, remote sensing observations and modeling results explore how complex underwater topographies alter coastal wave energy and flow patterns. Selected stormy periods were observed in addition to a set of idealized simulations. Results indicate that shore-oblique features cause localized changes to wave heights, wave breaking, and current speeds. These alterations contribute to the presence of fast offshore-directed rip currents and accelerations in shore-parallel currents, which would enhance the potential for sand to be transported away from these zones. The findings suggest that the changes to the flow field induced by the oblique features contribute to zones of high rates of erosion.

1 Introduction

The coastal nearshore region, defined as the transition zone between the shoreline and the inner shelf, is a dynamic zone shaped by the interplay of many physical processes occurring at various spatial and temporal scales. The level and distribution of incoming wave energy exerts a powerful control on nearshore forces and alters currents, sediment transport, and morphology (Wright & Short, 1984; Svendsen, 1984; Gallagher et al., 1998). When propagating at oblique incident angles to the bathymetric contours, surface waves transfer momentum and drive longshore currents, moving material along the coastline (Longuet-Higgins, 1970; Guza et al., 1986). These currents meander and change velocity in response to bathymetric variability (Garnier et al., 2013). At moderate incident angles, gradients in wave-driven setup of the mean water level can cause local alongshore flows to converge and flow offshore as rip-currents (Castelle et al., 2016; Moulton et al., 2017).

These strong offshore-directed rip currents can scour channels in nearshore sandbars and alter patterns in wave dissipation, causing the local mean water level to slope towards the rip channel (Haller et al., 2002). This feedback reinforces offshore flows and can erode the beach profile (Komar & McDougal, 1988). For weak offshore flows, wave energy dissipation can be reduced in rip-channels, leading to higher wave heights that break close to the shoreline (Haller et al., 2002) and increased vulnerability to erosion (Holman & Sallenger, 1993). In some cases, stable patterns in the underlying bathymetry (e.g., submarine canyons) produce morphologically-driven recurring offshore flows by redirecting wave energy (Long & Özkan-Haller, 2005; Magne et al., 2007; O'Dea et al., 2021). For example, dramatic variations in refraction and wave energy occur across the Scripps

Canyon in southern California, with increased local wave heights at the head of the canyon (Magne et al., 2007).

Morphologically-driven processes are often shaped by the underlying geology (also referred to as antecedent or framework geology). The geologic framework, generated over very long time scales, is characterized by deposits or bedrock underlying modern sediments to a depth of approximately 10 m (Browder & McNinch, 2006). Along the east coast of North America, anomalous nearshore bathymetric features have been identified and connected with geological history: shore-normal or shore-oblique troughs and bars occur in New York (Schwab et al., 2000), New Jersey (Snedden et al., 1994), Virginia (Colman et al., 1990; Browder & McNinch, 2006), North Carolina (McNinch, 2004), Florida (Houser et al., 2008; Barrett & Houser, 2012), northeastern New Zealand (Green et al., 2004), Prince Edward Island (Wernette & Houser, 2022) among many other locations and are commonly related to paleo-river channels. These features alter alongshore patterns in wave breaking (Safak et al., 2017), modify the distribution of wave energy (Mulligan et al., 2019a), and have been hypothesized to act as conduits for offshore sediment transport (Thieler et al., 1995) and enhanced alongshore advection (Gutierrez et al., 2005). However, the physical mechanisms linking framework geology to alterations in hydrodynamics and morphodynamics across the shoreface are not well understood.

In this study, we investigate the influence of a complex bathymetric framework on nearshore flow dynamics during storm conditions at Kitty Hawk, North Carolina, USA. We hypothesize that shore-oblique bathymetric features alter mean nearshore currents and induce localized zones of higher wave height and wave setup on the shoreface, which may affect sediment transport patterns and the morphology of this nearshore region. Both real and idealized storm events are simulated with a phase-resolving numerical model for a wide range of incident wave angles. The event-based simulations focus on time periods with large waves corresponding to Hurricane Jose and Hurricane Maria in 2017, that were also observed with an X-band radar (XBR) remote sensing system. The idealized simulations isolate the effects of the bathymetry and incident wave angle on the nearshore hydrodynamics. The novel combination of remote sensing and numerical results are synthesized to provide new insight on wave-driven flows over complex geologically-controlled bathymetric features.

1.1 Regional setting

Kitty Hawk (KH) is located on the Outer Banks of North Carolina (Fig. 1a). The Outer Banks are a series of long barrier islands segmented by inlets that formed in a microtidal, wave-dominated environment (Hayes, 1979), and are subject to storms (e.g., Tropical Cyclones and Nor'Easters) and high rates of sea level rise (Sallenger et al., 2012; Kemp et al., 2017). These barrier islands have been shaped into cuspate forelands that divide large estuaries (Albemarle and Pamlico Sounds) from the Atlantic Ocean. Currently, few inlets connect the sounds to the ocean and the barrier islands receive a very limited supply of sediment from riverine sources (Culver et al., 2007; Mulligan et al., 2019b). Located 5 km west of the modern transgressive shoreline at KH, a progradational beach ridge complex formed 3 ka - 2 ka before present during a period of rapid Holocene sea level rise and abundant sediment availability (Mallinson et al., 2008). The present-day coastal morphology and dynamics are influenced by the complex underlying regional geologic framework.

2 Shore-oblique features

The segment of coast is dominated by shore-parallel depth contours except near KH, where the nearshore region includes a series of bathymetric undulations with bars and troughs as shown in Fig. 1b. These bathymetric variations are situated in mean water depths ranging from 2-12 m and are oriented offshore at an average angle of 42° from the shoreline (Schupp et al., 2006). The morphologic features are referred to as shore-oblique features (SOFs) and, within the region considered in the present study, include a northern (SOF-N) and southern (SOF-S) trough shown in Fig. 1b. Seismic imaging studies have associated these bathymetric anomalies to underlying Pleistocene paleo-channels, specifically the paleo-Roanoke River (Boss et al., 2002; McNinch, 2004; Browder & McNinch, 2006). Cycles of eustatic sea-level changes that occurred concurrently with glacial episodes during the Pleistocene epoch dissected numerous fluvial channels into the underlying Quaternary strata (Boss et al., 2002). During the ensuing Holocene transgression, these channels were drowned and infilled with muds, peats, sands, and gravels (Riggs et al., 1992, 1995; Schwartz & Birkemeier, 2004).

The SOFs are relatively stable but can migrate approximately 250 m alongshore in response to individual storm events (McNinch & Miselis, 2012). Schupp et al. (2006) found that all movement was confined to zones shoreward of the -9 m bathymetric contour. They also slowly migrate downdrift on a decadal timescale. Between 2004 and 2017, SOF-N migrated south by approximately 600 m and deepened by 0.5 m (Szczyrba et al., 2023a). Regionally, these SOFs have been correlated with areas of high shoreline variability and, on longer time scales, high long-term shoreline change rates. McNinch (2004) visually identified a correlation between the SOFs and high shoreline change rates and Schupp et al. (2006) quantified this correlation on a regional scale as statistically significant. However, the nearshore hydrodynamic processes that physically link the SOFs with erosion have not been well defined.

3 Observations

3.1 Bathymetry and wave data

In June, 2017, bathymetric profiles were collected to support the local beach nourishment monitoring plan (APTIM, 2017). The nearshore survey lines were collected by a survey vessel and spaced approximately 150 m meters apart, with sounding points sampled every 7-8 m (APTIM, 2017). The survey data were interpolated onto a 5 m x 5 m regular grid in ArcGIS 10.7.1, encompassing two shore-oblique bathymetric features (SOF-N and SOF-S). This bathymetric grid, shown in Fig. 1c, is used as input to the numerical model.

Wave observations used as boundary conditions in the numerical model were sourced from the US Army Corps of Engineers Field Research Facility (FRF) at Duck, located 14 km north of KH. Wave spectra were observed by a 1 MHz Nortek Acoustic Wave and Current (AWAC) profiler, located offshore in a nominal depth of 11 m. Previous studies have shown that the bulk wave statistics including significant wave height (H_s), mean direction (θ_m), and peak period (T_p) are highly correlated at the 11 m depth over a distance of 33 km between the FRF and Jennette's Pier, located 20 km south of KH (Mulligan et al., 2019a). Wave data were obtained for key times during major wave events in September 2017. These correspond to a time during Hurricane Jose (denoted "J"; 19-September-2017 20:00:00 UTC), and two times during Hurricane Maria (denoted "M1" and "M2"; 27-September-2017 09:00:00 UTC and 28-September-2017 02:00:00 UTC) indicated in Fig. 2 and Table 1. Directional energy-density wave spectra were used as offshore boundary conditions for the numerical model (Fig. 3). The directional spectra were calculated from the first four Fourier coefficients, using the maximum entropy method (Lygre & Krogstad, 1986) with a directional resolution of 1°, a frequency resolution of 0.0075 Hz, and a frequency range of 0.0400-0.4975 Hz. The spectra were rotated 28° clockwise of true north to match the orientation of the rotated bathymetric grid before they were input into the model.

The times corresponding to J, M1, and M2 were selected because they have similar mean total water levels, and a range of energy levels and incident wave angles (Table 1 and Fig. 3). Hurricane Jose at time J was a moderate wave height ($H_s = 2.8$ m) event with a positive incident angle (meaning north of shore-perpendicular) and moderate directional spreading (Fig. 3a, d, g). Hurricane Maria at time M1 was a high-energy event, with an H_s of 4.0 m, long period waves, low directional spreading and an oblique positive incident angle (Fig. 3b, e, h). As Hurricane Maria propagated along the coastline, the dominant wind and wave direction shifted and the conditions at time M2, which occurred 17 hours after M1, had moderate wave heights ($H_s = 2.6$ m) and periods during the passage of the storm. Time M2 was characterized by high directional spreading from the high-frequency oblique wind-waves forced by strong offshore winds (Fig. 3c, f, i).

3.2 X-band radar collection and processing

The Radar Inlet Observation System (RIOS) is a fully automated non-Doppler XBR remote sensing system housed within a mobile trailer for rapid deployment (McNinch et al., 2012; Humberston et al., 2019). RIOS emits microwave radio signals with a horizontal beam width of 1.2° and a vertical beam width of 25° and records the subsequent backscatter. Bragg resonance is the primary mode of XBR backscatter, wherein radar pulses interact with short capillary waves (1-2 cm wavelength, λ) on the water surface. Backscatter increases when waves steepen, modulating the short-gravity wave field, and become roughened as they approach the shoreline and break (Catalán et al., 2014). Thus, RIOS provides a digital reconstruction of the incoming nearshore wave field as a series of sequential spikes in the XBR backscatter return intensity. XBR can resolve the spatio-temporal evolution of incoming nearshore waves and the observations compare well to both numerical models and in-situ data (Szczyrba et al., 2023b). Additional RIOS-system details are described by Humberston et al. (2019) and McNinch et al. (2012).

RIOS was deployed in the study site at the location shown in Fig. 1b (36.066408°, -75.690222°) in September, 2017. Nearshore sea surface conditions were observed for 14 minutes per hour between September 19-23 and September 27-30, capturing J, M1, and M2 time periods. The XBR antenna completed a rotation every 1.67 s, resulting in a sampling frequency of 0.60 Hz. Raw backscatter data were transformed from polar coordinates onto a 5 m x 5 m Cartesian grid (Humberston et al., 2019) and smoothed in the alongshore direction by 100 m using a multidimensional image averaging filter (imfilter). The resulting grid was rotated 28° clockwise of true north to match the orientation of the numerical modeling framework. Overall, the XBR footprint spanned 3 km alongshore and 1 km offshore. The time-dependant surf zone width was calculated from 14 minute time-averaged XBR backscatter data. Time-averaged XBR and optical data highlight zones of high dissipation and are often used to determine the spatial patterns of wave breaking (Lippmann et al., 1993; Brodie et al., 2018). Following the method described by O'Dea et al. (2021), the offshore surf zone edge was identified as the maximum cross-shore gradient of the XBR backscatter intensity, calculated at each alongshore location. Outliers were removed and the resulting surf zone edge lines were smoothed using a moving mean filter with a window size of 100 m.

Methods from O'Dea et al. (2021) were also applied to search for and identify morphologically driven offshore-directed currents in the study region. This approach analyzes backscatter intensity offshore of the surf zone where few waves are breaking. Offshore flows escaping beyond the breaker line can be identified in the XBR data as alterations in surface roughness. Offshore directed rip currents enhance sea surface roughness, incite short-scale wave breaking (i.e. microbreaking), and elevate XBR-measured backscatter intensity (Lyzenga, 1991; Plant et al., 2010; Haller et al., 2014; O'Dea et al., 2021). This effect has been confirmed in a study utilizing both XBR and GPS-equipped floating drifters (Takewaka & Yamakawa, 2011) and with a cross-shore array of current meters (Haller et al., 2014). To identify these zones of wave-current interaction, an alongshore transect of backscatter intensity was extracted at a location 100 m offshore of the surf zone edge during periods with waves with $H_s \geq 2$ m. The mean backscatter intensity was removed from each transect to highlight zone of anomalously high return intensities. The intensity anomaly transect data were then averaged together to identify persistent XBR backscatter anomalies in the 9-day observation period. The XBR anomalies for J, M1, and M2 were also analyzed.

XBR observations were used to determine representative wave phase speeds. Pixel intensity time series were input into the bathymetric-inversion algorithm cBathy (Holman et al., 2013b; Holman & Bergsma, 2021). cBathy is typically used to estimate bathymetry from optical imagery, often from Argus camera systems (e.g., Oades et al. (2023)), but can also process XBR data (Honegger et al., 2019). Resulting XBR-derived bathymetric surfaces have been applied in numerical modeling studies (O'Dea et al., 2021). The algorithm estimates the wave numbers (k) of dominant wave frequencies (f) and uses the linear dispersion equation to relate these k-f pairs to mean water depth. The k-f pairs are extracted within mapped tiles by calculating the Fourier phase cross-spectra between each pixel per tile. In the present study, tile spacings were set to be 10 m in the cross-shore direction and 25 m in the alongshore direction. The algorithm produces a matrix of wave numbers for each the most coherent 4 frequencies wherein the individual matrices contain a range of frequencies that represent the most dominant frequency calculated per pixel.

The most coherent k-f matrix was extracted to create wave speed maps of representative peak wave conditions for each event. cBathy's accuracy declines significantly in very shallow water with $h <$ -2 m (Honegger et al., 2019), therefore these regions were excluded from further analyses. Cross-shore transects were extracted to support comparisons with the modeling data with a 20 m moving mean applied to eliminate noise. Using the peak frequency calculated from cBathy, the method of Streßer et al. (2022) was adapted to convert XBR-measured wave phase speeds to representative wave height estimates (see Eq. 12 in Streßer et al. (2022)). Their wave-by-wave approach applies a physically derived scaling that relates changes in breaking phase speed to wave height via the amplitude dispersion relation:

$$H_p = \frac{{C_p}^2}{g(\frac{1}{\gamma} + \alpha_{ad})} \tag{1}$$

This equation was applied using the celerity of the peak frequency (C_p), the default breaking index (γ) value of 0.78 (Streßer et al., 2022; Larson & Kraus, 1994), and the recommended calibration coefficient (α_{ad}) value of 0.5 (Streßer et al., 2022) to estimate a representative wave height based on peak frequency values (H_p). This method is valid within the surf zone, since it was developed based on the modified nonlinear shallow water phase speed for waves in very shallow water (i.e., h:$\lambda < 1/10$) from Hedges (1976).

4 Numerical model

The phase-resolving 3D numerical model Simulating WAves till SHore (SWASH) applies the nonlinear shallow water horizontal momentum equations and the nonhydrostatic vertical momentum equation using a finite difference scheme (Zijlema et al., 2011; Zijlema, 2020) to simulate the water surface and velocity fluctuations. SWASH was applied to simulate several times (J, M1, M2) in the study period that correspond to radar data collection times. In addition to the selected events, an idealized suite of 21 simulations were also performed to isolate key variables and specifically explore how the incident wave conditions affect the nearshore hydrodynamics.

4.1 Model setup

SWASH has been used to simulate wave-driven currents over variable bathymetry, such as over submerged reefs (da Silva et al., 2023). Previous studies have also applied SWASH to model regions near the present study area (Gomes et al., 2016; Mulligan et al., 2019a; Szczyrba et al., 2023b) and similar numerical input parameters were applied in this study. A 5 m x 5 m regular structured grid, extending 1000 m offshore and 3000 m alongshore, was constructed. A 300 m extension was added to the offshore edge of the bathymetric grid (from x = 1000-1300 m) to create a uniform offshore region and prevent numerical anomalies from being introduced due to depth variations at the east boundary (without the extension, the bathymetric variations at the model boundary causes numerical instabilities that are not realistic). The extension was created by linearly interpolating the offshore bathymetric edge to a constant depth of h =-12 m over a cross-shore distance of 100 m and then extending this constant depth over the remaining 200 m, following previous studies (O'Dea et al., 2021). The bathymetry was also extended by 500 m in each alongshore direction by interpolating the sides to a uniform contour configuration in order to enable the application of periodic alongshore boundary conditions in the numerical model. The bathymetry data was rotated 28° clockwise of true north which oriented the mean shoreline parallel to the y-axis of the grid (Fig. 1c). To resolve depth-dependent dynamics, three bathymetry-following vertical layers with equal thickness were included. This vertical resolution is sufficient to resolve wave frequency-dispersion (Zijlema & Stelling, 2005; Smit et al., 2013). To confirm this, a sensitivity test using 9 vertical layers was conducted to explore the flow structure in and around the SOFs in further detail, and found no substantial differences from the 3-layer runs.

The Sommerfeld radiation condition was applied at the onshore boundary to appropriately limit wave reflection and the offshore boundary was weakly reflective. The alongshore boundary was periodic, meaning that energy exiting one alongshore boundary re-entered the domain at the opposite alongshore boundary. The first 15 minutes of modeling time were disregarded as model spin-up and the remaining 45 minutes were analyzed. The wavemaker generated random wave time series that statistically matched the input wave parameters with a cycle interval of 2700 seconds (45 minutes). According to Zijlema et al. (2011), the cycle time should span 100-300 peak wave periods to provide accurate statistical results and the selected cycle time spans over 200 wave periods of the longest peak period simulated (M1). The model performed calculations with an initial time step of 0.05 s that is automatically adjusted throughout the simulation according to the Courant number, which can reach a maximum of 0.5. Total water levels were adjusted for the correct tidal stage and storm surge present during the simulated events. Event times during hurricane wave events J (Jose), and M1, M2 (Maria) were forced at the offshore boundary using the directional energy-density spectra for each corresponding time (Fig. 3g-i).

4.2 Model output processing

To enable direct comparison with the XBR cBathy products, spectral processing extracted peak wave frequency parameters per grid cell from the J, M1, and M2 simulations. The fast Fourier transform was calculated at each grid cell with 256 samples and a Hanning window with 50% overlap. The peak wave frequency per grid cell was also extracted and used to calculate k and λ with the dispersion relation (Fenton & McKee, 1990; Dean & Dalrymple, 1991). The representative C_p was then calculated and input into Eq. 1. This approach emulates the XBR processing steps. H_s was calculated across the computational domain as four times the standard deviation of the water surface elevation output (Raubenheimer et al., 1996). The spatial gradient of the water surface elevation data highlighted wave crests as locations with steepest slopes. Vectors perpendicular to these crests at each grid cell were then time-averaged to provide local estimates of mean wave angles across the study region (Szczyrba et al., 2023b). A dimensionless wave breaking parameter (Q_b) was calculated from the binary wave breaking locations output from the model (Gomes et al., 2016). This parameter represents the relative intensity of breaking independent of the model time step and spatial resolution. These breaking zones were compared to the surf zone widths observed by XBR.

5 Results

5.1 Event flow dynamics

Regions of persistently high XBR backscatter outside of the surf zone were identified for J, M1, and M2 as well as the mean during all periods with $H_s \geq 2$ m observed by XBR (Fig. 4). The strongest XBR anomalies occur at the southern edge of SOF-N and the southern edge of SOF-S, located at y $\sim$ 1600 m and y $\sim$ 250 m (Fig. 4b-d). Each event, as well as the study-period mean, indicate anomalously high backscatter signals at these locations. Offshore flows enhance XBR backscatter intensity where wave-current interactions roughen the sea surface. Even during lower energy periods, high backscatter indicative of offshore flow extends outside of the surf zone. For example, as shown in Fig. 4d, at a time when $H_s = 2.3$ m, high backscatter return intensity (RI) is evident at y $\sim$ 1600 m and y $\sim$ 250 m. The signals along the southern edges of both SOFs are strongest during M2, an event with negatively incident (southerly) waves. Spikes in XBR backscatter also occur along both the northern and southern edges of SOF-S during M2, and in the channel trough backscatter measures abruptly weaken (Fig. 4b, c). In the mean observations, this U-shaped pattern in the XBR anomaly can be observed in both SOFs and is much wider in SOF-S than SOF-N. This U-shape indicates increased backscatter along both edges of each SOF, with the southern edge inducing stronger backscatter. M1, an event with large waves approaching the shoreline at a highly oblique, positive (northerly) angle, only exhibits backscatter anomalies along the southern edges of the SOFs, and no anomaly is detected near the northern edges. The strongest XBR anomalies align approximately with regions of higher local shoreline change rates, i.e., erosional hot spots (List et al., 2006), with a slight offset (Fig. 4a, b). Each hot spot is offset north of the southern edge of SOF-N and SOF-S, where the highest XBR anomalies occur.

The observed and simulated extent of the surf zone are shown in Fig. 5. Event M1 was the highest energy event with the widest surf zone (Fig. 5a). Mean surf zone widths are 223 m, 281 m, and 269 m for J, M1, and M2, respectively, however the extents vary considerably in the alongshore direction. The surf zone of M1 is widest north of SOF-N, beginning offshore at x $\sim$ 340 m. The surf zone of M2 is widest south of SOF-N, occurring at x $\sim$ 320 m. During all events, surf zones narrow along the shoreward apex of SOF-N and widen on either side, coincident with the feature's edges. SOF-N modulates surf zone widths more than SOF-S. The offshore extent of the surf zone identified by XBR (Fig. 5a) was compared to the breaking parameter (Q_b) calculated from the numerical model (Fig. 5b). The XBR-sensed surf zone edge aligns with the offshore edge of the most intense breaking locations in the SWASH simulations and displays similar lateral variability in break-point locations. During M1, Q_b is most intense at x $\sim$ 200 m, y $\sim$ 2,000, which is located along the northern edge of SOF-N (Fig. 5b).

Spatial patterns in C_p shown in Fig. 6 are similar in XBR observations (Fig. 6a) and SWASH results (Fig. 6b), wherein C_p remains high within the shore-oblique troughs as the waves approach the shoreline, coinciding with the bathymetric contours. Peak frequency waves enter the domain at 9-10 m/s and slow to 6-7 m/s along the 4 m bathymetric line. Across a variety of cross-shore profiles, XBR and SWASH estimates agree well (Fig. 6c-e). Mean C_p errors are 0.26, 0.26, and -0.04 m/s for J, M1, and M2, respectively, however errors vary spatially. In the cross-shore, error is highest shoreward of x $\sim$ 335 m where the model slightly underestimates C_p by 0.47 m/s when compared to XBR observations. In the alongshore, the model underestimates C_p north of y $\sim$ 1,750 m and overestimates south of y $\sim$ 1,500 m. Across all periods simulated, mean error is highest between y $\sim$ 925 - 1,225 m with a maximum of -0.53 m/s.

Using Eq. 1, spatial distributions of C_p were converted into representative wave heights (H_p) to further compare XBR and model results as shown in Fig. 7. Patterns in H_p compare well between XBR and the model. Wave heights vary laterally across the study domain, with higher wave heights reaching closer to the shoreline in the lee of the troughs of the SOFs. Wave dissipation begins along the 4 m contour lines. Root mean square errors (RMSE) are 0.76 m, 0.72 m, and 0.65 m across the entire domain and 1.35 m, 0.61 m, and 0.57 m within the surf zone for J, M1, and M2, respectively.

Fig. 8 displays the spatial patterns in relative wave height H_s/h (Fig. 8a) and wave frequency (Fig. 8b) alongside the alongshore distributions of the normalized maximum H_s (Fig. 8b) and the water surface elevation gradient (Fig. 8c) The distribution of modeled H_s varies across space and by event (Fig. 8a, b). Relative wave heights are elevated north and south of SOF-N around y $\sim$ 2000 and 1500 m, and in these zones high relative wave heights extend to the 6 m contour (Fig. 8a). H_s values increase near the SOFs and decrease in the region between SOF-N and SOF-S (Fig. 8b). During all events, H_s increases along the edges of the SOFs, following the bathymetric contours, and decreases along the central axes (Fig. 8b). The alongshore differences in H_s at a particular cross-shore location varies between 0.2-0.4 m. The alongshore variability in wave heights also induces strong variations in the water surface elevation gradient (Fig. 8c). At SOF-N, the minimum alongshore gradient occurs at y = 1665 m and then sharply increases on either side of that location across all events. The mean wave frequency is also elevated along the southern edges of SOF-N and SOF-S, coincident with the abrupt alongshore variations in wave setup (Fig. 8c), indicative of wave-current interactions. The wave frequency changes displayed in Fig. 8d appear similar to the XBR backscatter patterns displayed in Fig. 4d.

Simulated wave angle and velocity results near SOF-N during J, M1, and M2 are shown in 9. The SOFs modulate patterns of wave refraction during each event (Fig. 9a-c). M1 waves maintain positive approach angles across the domain even near the shoreline but are moderated closer towards shore-normal in the lee of SOF-N. J and M2 waves refract into positive and negative directions, creating zones of convergence and divergence around SOF-N. In both events, divergence occurs along the northern edge of SOF-N while convergence occurs along the southern edge. A similar, but less severe effect, is observed around SOF-S. The features cause asymmetric wave refraction, whereby wave entering at moderate angles refract away from the trough and toward the edges of the SOFs (Fig. 9a-c), increasing wave heights along the edges and sheltering the zone immediately in the lee of the trough (Fig. 8b).

Across all three selected times, cross-shore velocities are directed offshore down the oblique central axis of SOF-N (Fig. 9d-f), coinciding with the locations of wave divergence (Fig. 9a-c). These flows decelerate and broaden as they move offshore. Cross-shore velocities route back onshore at the southern edge outside of the surf zone and this shoreward-directed patch occurs 50 m farther offshore during M1 than during J and M2. North of SOF-N, cross-shore velocities are also directed onshore during J and M2, but this effect is weak during M1. The offshore and onshore-directed velocities thus form asymmetric circulation cells, with the stronger cell occurring along SOF-N's southern edge. The location of the maximum and minimum cross-shore velocities remain fairly stable across all three periods simulated. Alongshore velocities accelerate and meander significantly offshore near SOF-N in J and M2 (Fig. 9g-i). The acceleration in both events occurs near x $\sim$ 250 m, y $\sim$ 1750 m. During M1, the alongshore velocities are very strong and meander slightly in response to the SOF contours. The longshore current reverses direction during M2 at x $\sim$ 300 m, y $\sim$ 1950 m, and the nexus of the reversal coincides with a location of high cross-shore velocity.

During J and M2, the mean flow is characterized by two circulation cells between (1) x ∼ 0-500 m, y ∼ 2000-2500 m and (2) x ∼ 0-500 m, y ∼ 1500-2000 m (Fig. 9j-l). The southern circulation cell is stronger than the northern cell. While water moves offshore down the axis of SOF-N in J and M2, the mean current merely meanders in response SOF in M1 since the strong inertia of the longshore current overpowers potential circulation cells. The offshore-directed flows in J and M2 maintain high velocities offshore of the surf zone, with fast flows identifiable up to 2 surf zone widths away from shoreline. Offshore of SOF-N at x = 600 m, the maximum velocities occur in similar locations (U = 0.57 m/s, 0.90 m/s, 0.54 m/s at y = 1820 m, 1515 m, 1500 m for J, M1, M2, respectively) and the minimum velocities also occur in similar locations (U = 0.45 m/a, 0.79 m/s, 0.40 m/s at y = 2275 m, 2065 m, 2255 m for J, M1, M2, respectively). The alongshore velocity component plays a larger role than the cross-shore velocity component in controlling the overall mean current.

5.2 Idealized effects of incident wave conditions

A second suite of idealized simulations isolated the effects of various wave conditions including incident θ_p and H_s on nearshore hydrodynamics. These simulations were forced by a JONSWAP spectra with a T_p of 12 s and zero directional spreading. The H_s values varied between 1.0, 3.0, and 5.0 m while θ_p varied between -15 to 15° in intervals of 5°. It should be noted that the ideal simulation with an H_s of 5.0 m and θ_p of 15° failed because large waves at highly oblique angles are challenging to simulate (Baker et al., 2021). Thus, results for that simulations pertain to an H_s of 4.9 m at θ_p of 15°.

Model results of Q_b across a variety of incident wave approach angles are shown in Fig. 10. Incident waves that approach from +15° and transition to -15° emulate a common pathway of tropical cyclones in this region and Q_b varies depending on the incoming θ_p (Fig. 10). Q_b is dispersed relatively evenly alongshore between the 6 m depth contour and the shoreline when incident waves approach at +15°. However, Q_b begins further offshore along the edges of SOF-N and closer to the shoreline at the shoreward apex of the SOF. Between +10° - 0°, Q_b begins to concentrate along the northern edge of SOF-N. The breaking region is most localized when incident waves approach at -5°, focused at the shoreward apex of SOF-N (near x = 150 m, y = 1750 m) as well as SOF-S (near x = 250 m, y = 500 m). North of SOF-N most breaking occurs at the shoreline. At -10°, waves break again across the northern sandbar. Finally, at -15°, breaking is more widely distributed across the axes of both SOF-N and SOF-S.

Simulated U across a variety of incident wave approach angles are shown in Fig. 11. When waves approach the shoreline at highly oblique angles, a strong longshore current develops with minor offshore movement (Fig. 11a-b, f-g). The longshore currents accelerate at the apex of SOF-N, near y = 1900 m, and SOF-S, near y = 500 m, and the flow also meanders slightly offshore in these zones. With moderate incident θ_p, several offshore circulation cells develop. During moderately positive incident angles, offshore flows route down the northern edges of the SOFs (Fig. 11b, c) while during moderately negative incident angles, they flow down the southern edges of the SOFs (Fig. 11e, f). During periods of negative wave incidents (Fig. 11e-g), a localized zone of flow acceleration away from the shoreline develops at the location where the shoreline angle changes orientation, between y = 1400 - 1600 m.

Across all simulations, weak offshore flows are consistently present along either the northern or southern edges of SOF-N and SOF-S and these offshore currents exit the computational domain, 1 km away from the shoreline (Fig. 11). However, at moderate incident angles, the offshore flows strengthen, coalesce, and develop complex pathways. Near the shoreline, a series of alongshore feeder currents converge and route offshore across a wide zone around SOF-N (Fig. 11c-e). Beginning at an incident angle of +5°, four distinct zones of offshore-routed flows develop at y = 250 m, y = 1100 m, y = 1600 m, and y = 2500 m (Fig. 11c). These flows strengthen as incident angles shift towards -5° and begin to converge into two dominant offshore routing zones (near y = 750 m and 1800 m) which are continually present as wave angles continue to become more oblique at -10°, identifiable at y = 450 m and y = 1750 m (Fig. 11f).

6 Discussion

6.1 Model error assessment

Several past studies have evaluated a similar model configuration at the FRF and found that model results of H_s and energy-density spectra compare well with in-situ sensors located across the nearshore region (Gomes et al., 2016) as well as spatially-continuous XBR estimates of wave angles and wave breaking patterns (Szczyrba et al., 2023b). In the absence of in-situ sensors situated within the study site, the accuracy of the J, M1, and M2 simulations is assessed through a comparison to the XBR observations of surf zone width, celerity, and wave height. The alongshore variability in surf zone width measured by XBR is well represented by patterns of Q_b simulated in the model (Fig. 5b). Mean celerity errors are low, ranging from -0.04 to 0.26 m/s. Errors are highest shoreward of x = 400 m, where high rates of bathymetric change occur (Fig. 6).

Estimates of H_p are also in good agreement and both depict similar alongshore variability in response to the complex bathymetric configuration (Fig. 7). The best available bathymetric data were surveyed in June of 2017. Subsequent changes in the nearshore morphology, particularly in the surf and swash zones, would lead to differences in wave parameters estimated from XBR and SWASH and contribute to the identified errors. Past studies have indicated that the SOFs in the region remain in fixed locations even after energetic wave events (McNinch, 2004; Browder & McNinch, 2006; Schupp et al., 2006), therefore it is expected that high errors due to alterations in the bathymetry would be confined to zones closest to the shoreline.

6.2 Identification of rip currents

Anomalously high XBR backscatter signals seaward of the surf zone can occur where incoming waves interact with surface current convergences, such as rip currents and other offshore flows (Takewaka & Yamakawa, 2011; Haller et al., 2014; O'Dea et al., 2021). Backscatter anomalies indicative of strong offshore currents are visible in nearly every collection hour with incident $H_s \geq 2$ m (Fig. 4d). These offshore flows emerge in two primary locations, between y = 200 - 400 m and between y = 1500 - 2000 m. Flow structures remain visible for several hours across a variety of incident angles, water levels, wave periods, and directional spreading conditions. The visible plumes also extend 1-3 surf-zone widths beyond the XBR-identified surf zone edge (Fig. 4), supporting the findings of Kumar et al. (2021) and O'Dea et al. (2021).

Because the observed currents re-emerge in similar positions, they are likely morphologically controlled (Short, 2007). These flow structures are more obscured when wind levels in the region reach above 10 m/s (Fig. 4c) because XBR images become saturated during periods of high water surface roughness (Haller et al., 2014). Another limitation of XBR is the requisite for depth-limited wave breaking. Small waves below ∼1 m are not large enough to be resolved by XBR, although this threshold is site-specific (McNinch, 2007). However, rip currents are also more likely to be generated as wave energy increases (MacMahan et al., 2005), thus XBR remains a useful tool to identify them.

The observed reoccurring offshore flows coincide with the locations of SOF-N and SOF-S and are also represented in simulations of J, M1, and M2 (Fig. 8d and Fig. 9j-l). Because the maximum current velocities outside of the surf zone at x = 600 m reach values between 0.54 - 0.90 m/s during these events, these flows would pose a risk to human safety and thus can be considered morphologically-controlled rip currents (Leatherman & Fletemeyer, 2011). Similar re-emergent flows are also represented in the idealized simulations with H_s values of 1 m, 3 m, and 5 m (Fig. 11). Even during low energy conditions (H_s = 1 m), narrow bands of weak offshore flow appear in a similar location shoreward of SOF-S (flows originating near y = 500 m) and SOF-N (flows originating near y = 1500 m).

During higher energy conditions (H_s = 3 m and 5 m), the origin of the offshore flow within the surf zone is more variable, however the flows preferentially route along either the northern or southern edges of SOF-N and SOF-S. When waves approach at a positive angle, depth-averaged currents are directed onshore along the southern edge (upstream side of the SOF) and are offshore-directed along the northern edge (downstream side). The opposite circulation pattern emerges when waves approach at a negative angle, with offshore flows directed along the southern edge. This patterns is similar to observations of a dredged rip channel by Moulton et al. (2017), wherein a commonly observed circulation pattern included meandering longshore currents with offshore-directed flows occurring on the downstream rip channel wall.

Other studies have linked complex bathymetry to rip current generation. Along the northern shore of Prince Edward Island, Canada, Wernette and Houser (2022) proposed a relationship between paleo-river channels identified by ground-penetrating radar and rip currents observed by aerial imagery. At the present study site, results indicate that the SOFs act as a pseudo-transverse bar and rip morphology, which is associated with a common class of rip currents (Holman et al., 2006; Short, 2007; Turner et al., 2007). However, the SOFs remain fixed in place with little change, as opposed to ephemeral sandbar features that migrate shoreward after a storm reset (Houser et al., 2020). This process is akin to the shoreface-connected ridges on Fire Island, New York that have also been shown to modify wave refraction and produce alongshore variable wave breaking patterns (Safak et al., 2017).

6.3 Rip current generation

Rip currents are driven by gradients in wave momentum (Longuet-Higgins & Stewart, 1964) resulting from alongshore variations in wave breaking (Lippmann & Holman, 1989). These variations can be caused by hydrodynamic forcing, such as intersecting wave trains, standing edge waves, and wave spreading (Bowen, 1969; Suanda & Feddersen, 2015; Kumar & Feddersen, 2017; Moulton et al., 2023), or artificial structures, such as piers and groynes (Pattiaratchi et al., 2009). However, they are more often induced by alongshore variations in surf zone morphology (Bowen, 1969; Dalrymple, 1978). While the SOFs at this site are not morphologically pronounced within the surf zone, they are persistent nearshore structures that visibly impact the configuration of the bathymetry in areas of depth-limited breaking during higher energy wave events (e.g., the 4 m isobath, Fig. 1). Thus, the SOFs induce substantial alongshore variability in wave setup (Fig. 8c).

Nearshore wave heights respond to changes in nearshore bathymetry and the present results indicate that larger waves reach closer to the shoreline along the axis of the SOFs (Fig. 7), supporting the conclusions of Mulligan et al. (2019a) and observations by Sonu (1972) at other sites. Waves refract across the obliquely variable bathymetry (Fig. 9a-c), creating zones of wave energy convergence and alongshore variations in H_s (Fig. 8a, b). As a result, alongshore variations in wave breaking and surf zone widths also occur (Fig. 5), which can drive rip currents (Bowen, 1969; Dalrymple, 1978). Higher setup is generated near the shoreward side edges of the SOFs due to variability in wave breaking (Fig. 8c), leading to a pressure gradient that forces water to flow away from regions of intense breaking towards zones of lower setup. When these alongshore flows converge, they route offshore (Fig. 9), interact with the incoming wave field, and cause localized zones of higher frequency waves (Fig. 8d) and rougher water (Fig. 4b). These results support the findings of experimental rip channel studies (Haller et al., 2002; Moulton et al., 2017).

6.4 Influence of wave climate

The mean incident wave conditions near KH throughout 2017 included a significant wave height of 0.87 m, mean incident angle of 17°, and 32° of directional spreading. However, Nor'easters and tropical cyclones generate a variety of high-energy incident wave conditions in this region. When waves approach the SOFs at angles close to the orientation of the axis (negative incident angles, in our coordinate system), wave breaking occurs in concentrated local patches (Fig. 10). When approaching from the opposite direction (positive incident wave angles), wave breaking is more widely distributed along the 4 m isobath. These findings support Safak et al. (2017), who concluded that when waves approach shoreface-connected ridges at angles similar to the angle of the ridge crests, the features focused the most wave energy. Strong offshore flows (i.e., rip currents) are more likely to occur when wave angles approach the site between -10° to 10° (Fig. 11). Rip currents are more prevalent during conditions of moderate incident wave angles (Engle, 2002; MacMahan et al., 2005; Dusek & Seim, 2013a) because highly oblique angles induce strong longshore currents that inhibit offshore flow (Kumar et al., 2011). During positive, oblique incident conditions (15°), the longshore current accelerates where the contours of the SOFs pinch towards the shoreline (Fig. 11a) whereas during negative, oblique conditions (-15°), this acceleration occurs south of the SOFs.

Numerous weak offshore flows occur during periods of low energy, however these offshore flows re-emerge in similar positions across a variety of incident wave angles. As H_s increases, these offshore flows coalesce into larger, stronger offshore flows resembling rip currents (Fig. 11 that preferentially route down either the northern or southern edges of the SOFs when incident wave angles enter the domain between -10° to 10°. Fig. 12 explores the idealized effect of incident H_s and θ on maximum U (Fig. 12a, c-e) and variability of U (Fig. 12b, f-h) at the mean XBR-measured surf zone location as well as two zones located 250 m and 500 m offshore. Within the surf zone, maximum U values are mostly found at the shoreward axis of SOF-N, located at approximately $y = 1650 - 2000m$ (Fig. 12a). Additionally, U generally increases with increasingly oblique waves, owing to the generation of a strong longshore current (Fig. 12c). The variability of U is higher for negatively incident waves, but is highest for waves of moderate incident angles (Fig. 12f). Both mean U and the variability of U decrease offshore and increase with larger H_s. At all cross-shore locations, the variability of U decreases with increasingly oblique incident waves (Fig. 12f-h). The locations of maximum U variability are concentrated along the southern edges of both SOF-N and SOF-S (Fig. 12b).

The idealized simulations do not represent realistic field conditions, but are intended to isolate the response to different incident wave conditions. This set of simulations included JONSWAP spectra with zero directional spreading. Several studies have suggested that rip currents are more pervasive during narrow-banded incident conditions (Dusek et al., 2011; Dusek & Seim, 2013b), therefore the idealized results can not be used to predict rip current activity. However, XBR images indicate that rip currents at this site are indeed generated throughout a range of incident angles and directional spreading values (Fig. 4). The purpose of the idealized results is to explore the sensitivity and response of the SOFs to isolated variables (i.e. θ, H_s). It is also well known that rip current intensity varies in response to the total water level (e.g., tidal stage) and that strong rip currents can occur at low tide even during periods of low energy conditions due to enhanced wave breaking over surf zone sandbars (Brander & Short, 2001; MacMahan et al., 2005; Voulgaris et al., 2011). Overall, bathymetrically controlled rip currents tend to be strongest and most prevalent during periods of low water levels, high H_s, moderate incident $|theta$, and low spreading (Haller et al., 2002; MacMahan et al., 2010; Moulton et al., 2017).

6.5 Implications for hot spots of erosion

Prior studies have demonstrated that, at the regional scale (i.e., $\sim$ 40 km alongshore length), SOFs in the Outer Banks correlate significantly with erosional hot spots (McNinch, 2004; Schupp et al., 2006). The physical mechanisms contributing to the causal relationship have previously not been determined. The results of this research suggest that strong cross-shore fluxes (i.e., rip currents) are concentrated near the SOFs during periods with moderate incident wave angles. Between 2012 and 2022, 72 beach rescues specifically related to rip currents occurred within the study site (Kitty Hawk Ocean Rescue, personal communication, September 28, 2023). Rip currents and surf zone eddies are the primary mechanisms for cross-shore sediment transport (MacMahan et al., 2006; Dalrymple et al., 2011; Castelle et al., 2016) and Splinter and Palmsten (2012) found that areas of higher dune erosion occur where rip currents are present directly offshore. During periods of both high wave energy and moderate wave angles, strong offshore-directed flows may pronounce offshore transport, leading to enhanced erosion and undulations in the shape of the shoreline, similar to the results found in Fire Island, New York by Safak et al. (2017). During conditions with more oblique incident wave angles, longshore currents accelerate near the SOFs due to alongshore variability in bathymetry, which would also contribute to higher rates of sediment transport. Therefore, across a range of incident wave conditions and energy levels, a combination of longshore current accelerations and far-reaching offshore flows could contribute to the severity of beach erosion near the SOFs at this site.

Bathymetric surveys indicate that between 2004 and 2017 the trough of the 4 m contour within SOF-N and SOF-S deepened and moved south by 300 - 400 m (Szczyrba et al., 2023a). This might explain the southerly offset between the origin of the morphologically controlled rip currents and the long-term shoreline change rates (Fig. 4). We hypothesize that bathymetric hysteresis causes the erosional hot spot to lag behind the southerly movement of the SOFs and, therefore, in the future the hot spot will migrate south. When comparing the long-term shoreline change rate data released in 2004, 2013, and 2020, there is some evidence that the hot spot is intensifying and expanding southwards as the SOF troughs have deepened and moved south, although these data are cumulative long-term averages that do not highlight year to year changes. Nevertheless, according to these data, between 2004 and 2020 the rate of erosion at SOF-N increased from -0.36 m/yr to -0.70 m/yr and the SOF-S from -0.79 m/yr to -1.00 m/yr. The areas affected have also expanded south by 100 m (*North Carolina Division Of Coastal Management*, 2021).

However, this hypothesis is complicated by the beach nourishment projects that occur in this region nearly every five years. A monitoring report conducted one year after the conclusion of the 2017 beach nourishment project in KH observed that that up to 60% of the sand volume loss occurred adjacent to the SOFs, although the authors cited challenges in calculating sediment volumes around the complex bathymetric structures (APTIM, 2019). The report concluded that future monitoring should investigate the impact of these SOFs on nourishment performance. The results of this study suggest that the SOFs act as a conduit for enhanced cross-shore exchange of sediment because, during periods of moderate wave heights and angles, enhanced flow velocities are directed offshore down the SOF edges and persist beyond the surf zone edge. During periods with strong longshore currents, the flow accelerates and meanders near the SOFs, which would further enhance sediment transport away from the SOF and contributing to the erosional hot spot. These findings emphasize the importance of both cross- and longshore transport on nearshore morphological evolution, supporting the conclusions of Thieler et al. (1995) and Gutierrez et al. (2005) at other sites.

The storm-induced wave forcing addressed in this research also affects shoreline change on an inter-annual to decadal time scale (Splinter et al., 2014). As climate change alters ocean temperatures, the intensity and duration of the Atlantic hurricane season may increase (Knutson et al., 2010; Walsh et al., 2016). This elevates the likelihood of sequential high-energy wave events (i.e., storm clusters) that inhibit beach recovery (Coco et al., 2014) and result in higher rates of shoreline recession (Dodet et al., 2019). Geologically inherited complex bathymetry produces variability in beach response and recovery, whereby influencing the pattern of barrier island transgression over time (Houser, 2012). With a more intense wave climate, complex nearshore bathymetric features will continue to drive spatially variable circulation patterns and affect erosional hot spots.

7 Summary and Conclusions

The influence of complex bathymetry on nearshore flow dynamics in an area with erosional hot spots was explored with a combination of remotely-sensed data and a numerical model. An X-Band Radar (XBR) system was deployed at the study site in Kitty Hawk, North Carolina,zfor nine days at the end of September, 2017. This period coincided with the passage of Hurricane Jose and Hurricane Maria, and these events were also simulated with a phase-resolving numerical model. In total, 24 simulations were performed: 3 selected times during storm events (J, M1, M2) that were also observed by XBR and 21 idealized simulations that explored a range of incident wave conditions. The event simulations were validated against XBR observations of wave breaking patterns, celerity, and representative wave height estimates.

The XBR observations were used to identify two zones of persistently high sea-surface backscatter during energetic periods ($H_s \geq 2$ m), indicative of strong offshore flows. Across a wide variety of incident wave conditions, the offshore flows re-emerged near shore oblique features (SOFs) and are concluded to be bathymetrically controlled rip currents. The wave-current interactions associated with these offshore flows roughens the sea surface, enabling them to be easily identified with XBR, and also increases the wave frequency in localized zones. The location of the offshore currents are also linked to the incident wave direction and the bathymetry. When waves approach the shoreline at a positive angle, the offshore currents flow along the northern SOF edges while when wave approach at a negative angle, the flows route along the southern edges. The rip currents result from wave breaking across the alongshore-varying bathymetry near the SOFs, supported by both XBR and numerical modeling data. Numerical simulations indicate that relative wave heights and wave setup also vary across the cross-section of the SOFs. When the wave field is oblique, a strong alongshore current represses offshore flows, and this current accelerates and meanders where the SOF contours pinch towards the shoreline.

Idealized simulations indicate that the complex bathymetry exerts a strong control over nearshore wave heights, refraction patterns, and mean currents. The XBR observations were used to identify morphologically-driven persistent offshore-directed flows just south of long-term erosional hot spots. Future studies, using other numerical models that simulate sediment movement and bed elevation change, could directly model the morphodynamic evolution of zones with complex bathymetry to evaluate impacts on erosional hot spot intensity and evolution. Persistent offshore flows and alongshore flow acceleration may exacerbate erosion and enhance the shoreline undulations at this site. This underscores the importance of both cross-shore and alongshore sediment transport on the nearshore morphology and shoreline evolution on sandy beaches with nearshore bathymetric features.

8 Data Availability Statement

All model inputs, radar data, processed model output data, and figure generation MATLAB codes used in this study are hosted on the Borealis data repository at Queen's University titled "Nearshore Flow Dynamics – SWASH and XBand Radar", via DOI: `https://borealisdata.ca/privateurl.xhtml?token=fa6593ed-6ea6-437c-8734-4711be8950c8` with data use license agreement CC-BY 4.0. This is a private link for reviewers only, and the public link will be included upon manuscript acceptance.

Acknowledgments

This research is supported by a Queen's School of Graduate Studies Doctoral Fellowship to LS and Natural Sciences and Engineering Research Council of Canada (NSERC) Discovery Grants to RPM and PKP. We thank the staff of the US Army Corps of Engineers Field Research Facility (FRF) and Engineer Research and Development Center (ERDC) Coastal and Hydraulics Laboratory (CHL) for help with field observations. We also thank a supportive group of coastal researchers for their insightful guidance, including Elora Oades from Queen's University, Dr. David Honegger from Oregon State University, and Dr. Spicer Bak as well as Dr. Kate Brodie from the U.S. Army Engineer Research and Development Center.

Acronyms

AWAC Acoustic Wave and Currents profiler
FRF Field Research Facility
KH Kitty Hawk
RIOS Radar Inlet Observation System
R.I. Return intensity of X-band radar
RMSE Root mean square error
SOF Shore-oblique feature
SOF-N Northern shore-oblique feature
SOF-S Southern shore-oblique feature
SWASH Simulating WAves till SHore
TKE Turbulent kinetic energy
XBR X-band radar

Notation

$\boldsymbol{\alpha_{ad}}$ Calibration coefficient, Eq. 12 from Streßer et al. (2022)
$\boldsymbol{C_p}$ Celerity of peak frequency waves [m/s]
$\boldsymbol{D_{50}}$ Median grain size [mm]
$\boldsymbol{\eta}$ Water surface elevation [m]
$\boldsymbol{f}$ Wave frequency [Hz]
γ Breaking index (0.78)
$\boldsymbol{g}$ Gravitational acceleration [m/s^2]]
$\boldsymbol{h}$ Water depth [m]
$\boldsymbol{H_p}$ Height of peak frequency waves [m]
$\boldsymbol{H_s}$ Significant wave height [m]
$\boldsymbol{k}$ Wave number [1/m]
$\boldsymbol{\lambda}$ Wavelength [m]
$\boldsymbol{\theta_m}$ Mean wave angle [°]
$\boldsymbol{\tau}$ Shear [N/m^2]
$\boldsymbol{T_p}$ Peak period [s]
$\boldsymbol{U}$ Depth-averaged mean velocity [m/s]
$\boldsymbol{U_{*cr}}$ Critical velocity [m/s]
$\boldsymbol{Q_b}$ Breaking parameter

Table 1. Wave conditions during the hindcast simulated event (J, M1, M2) including significant wave height (H_s), peak period (T_p), total water level (η), mean wave angle relative to perpendicular of the study site's mean shoreline (θ_m), and peak directional spreading (σ_p).

Label	UTC	H_s [m]	T_p [s]	η [m]	θ_m [°]	σ_p [°]
J	19-Sep-2017 20:00:00	2.8	10.0	0.9	3.9	36.3
M1	27-Sep-2017 09:00:00	4.0	13.3	0.7	16.9	23.2
M2	28-Sep-2017 02:00:00	2.6	10.3	0.8	-37.1	58.5

Measured at the FRF's 11 m AWAC.

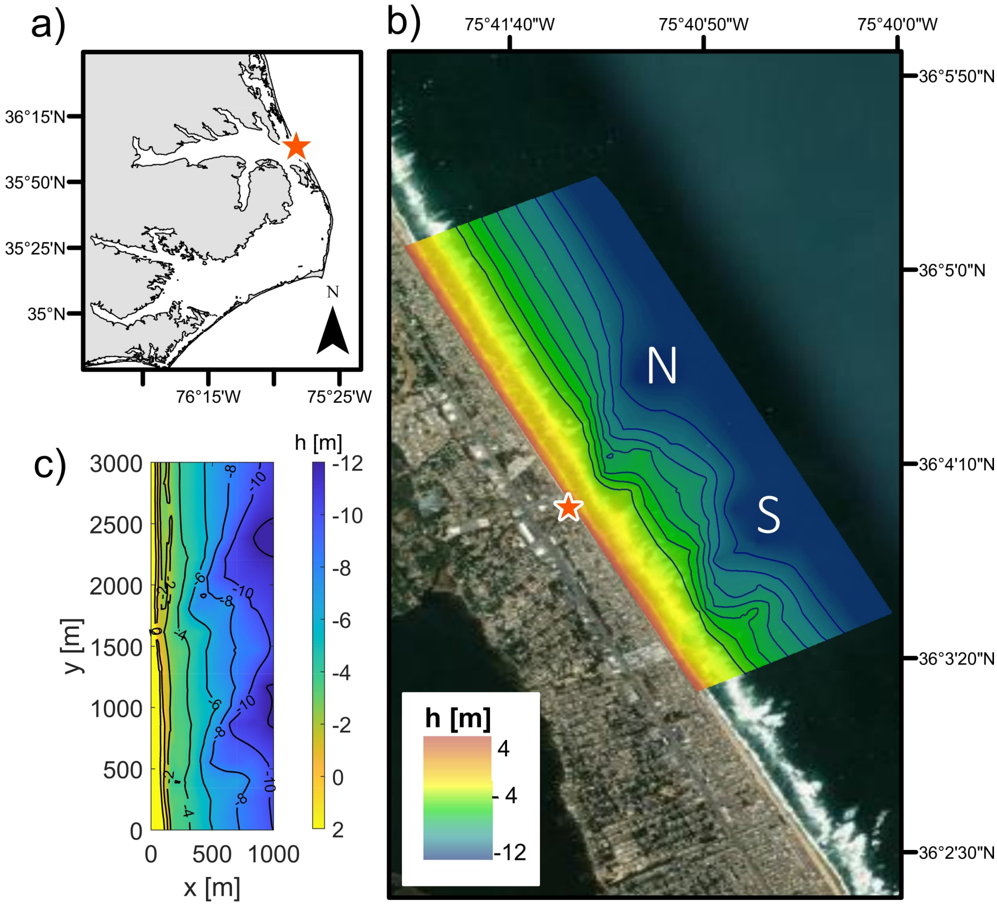

Figure 1. (a) Study region location within the Outer Banks, (b) June 2017 bathymetry measured offshore of Kitty Hawk, North Carolina where the red star represents the XBR location and labels N and S identify the lcoations of SOF-N and SOF-S, respectively, and (c) rotated bathymetric grid used for numerical modeling.

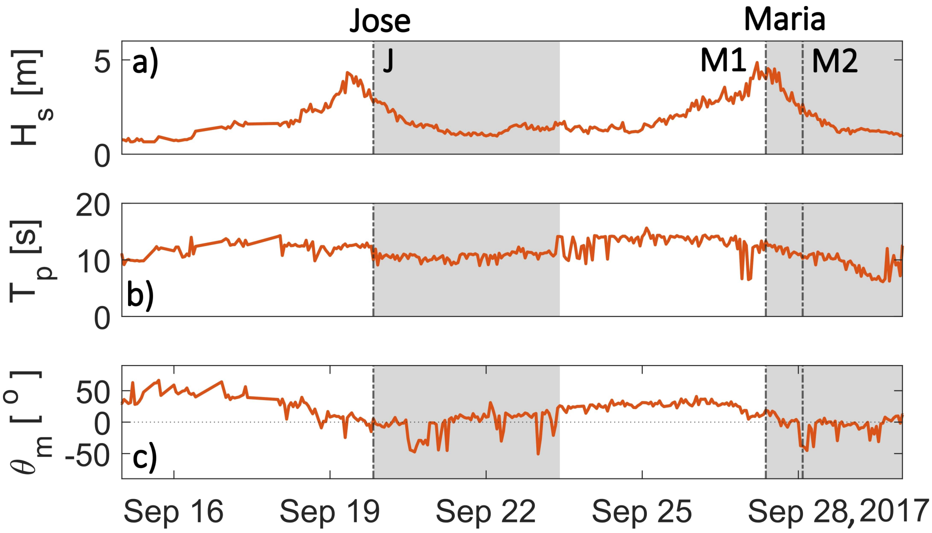

Figure 2. Wave conditions throughout the study period: (a) significant wave height (H_s), (b) peak period (T_p), and (c) mean wave angle relative to perpendicular of the mean shoreline (θ_m). Wave angles are described as going towards, meaning positive values indicate an approach angle north of shore-perpendicular and negative values indicate an approach angle south of shore-perpendicular. Vertical dashed lines indicate the simulated hours during Hurricanes Jose and Maria (J, M1, M2) and shaded regions are periods observed by XBR.

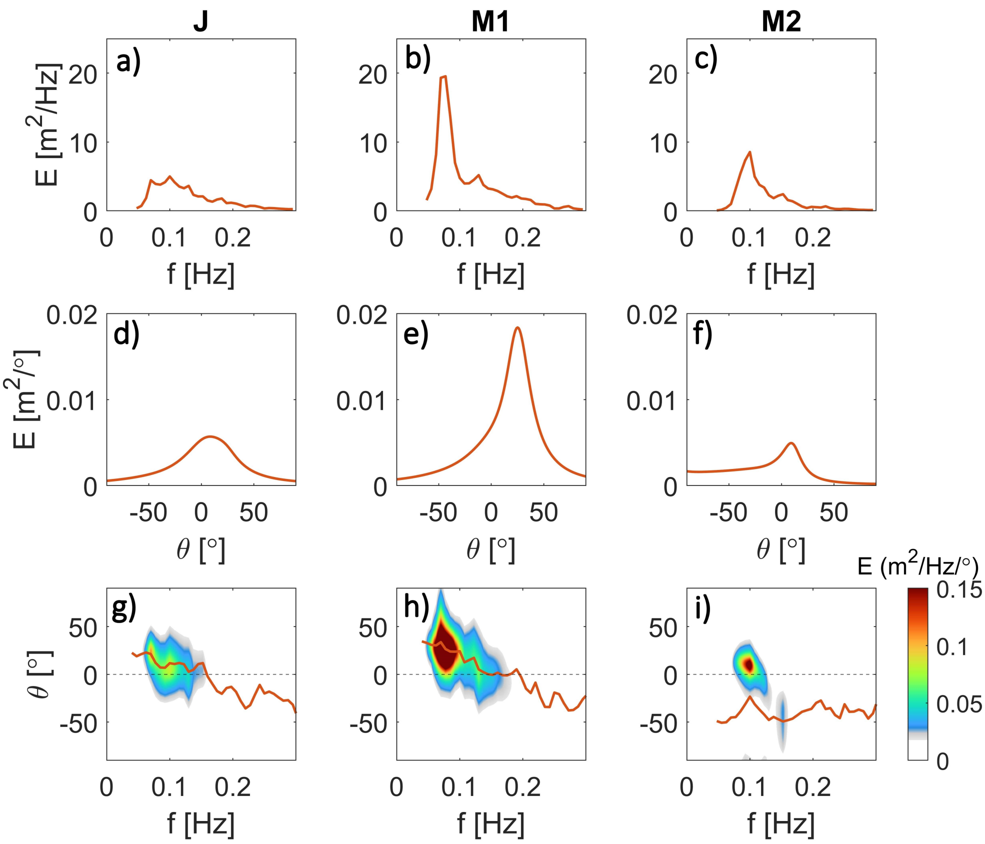

Figure 3. Wave spectra for time periods (left column) J, (middle column) M1, and (right column) M2: (a, b, c) energy-density, (d, e, f) directional distribution of wave angles, and (g, h, i) directional energy-density spectra used to force simulations at the offshore boundary. Red lines in (g, h, i) are the mean direction per frequency calculated from Kuik et al. (1988). Wave angles are described as going towards, meaning positive values indicate an approach angle north of shore-perpendicular and negative values indicate an approach angle south of shore-perpendicular.

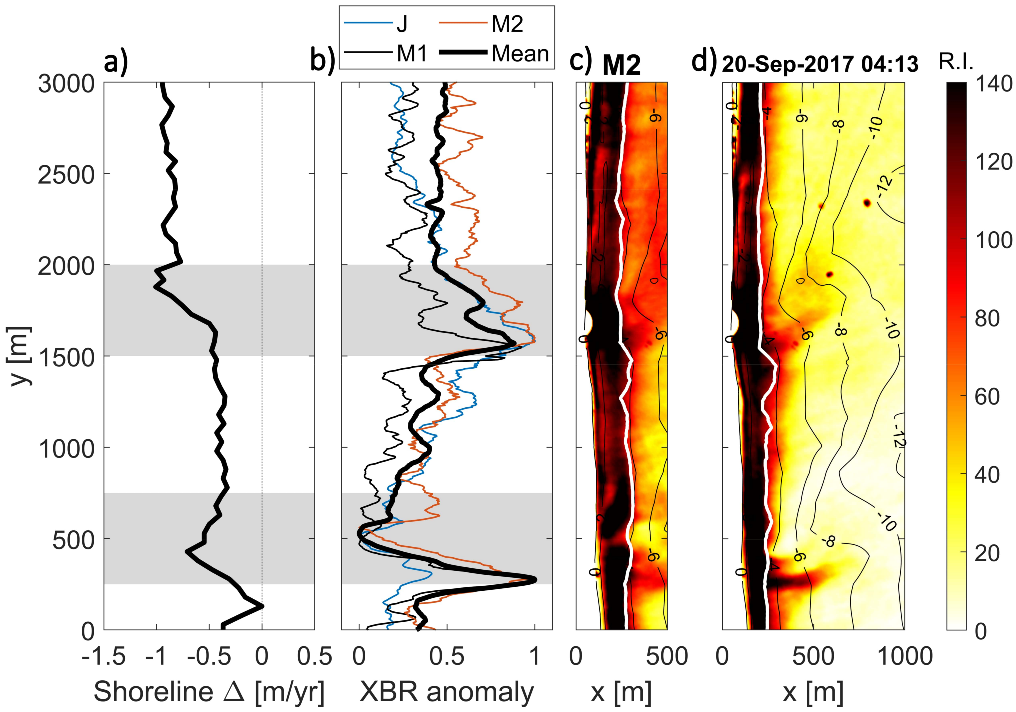

Figure 4. Alongshore variability in: (a) the long-term average shoreline change rate over 1940-2016 with shaded regions indicating the troughs of SOF-N and SOF-s;(b) XBR backscatter intensity anomalies for J (blue line), M1 (black line), M2 (orange line), and the mean during the observation period (thick black line); (c) time-averaged XBR backscatter return intensity (R.I.) during event M2 with the white lines indicating the corresponding XBR estimated offshore edge of the surf zone; and (d) time-averaged XBR backscatter during a moderate energy event (H_s = 2.3 m) on September 20, 2017 at 04:13 UTC.

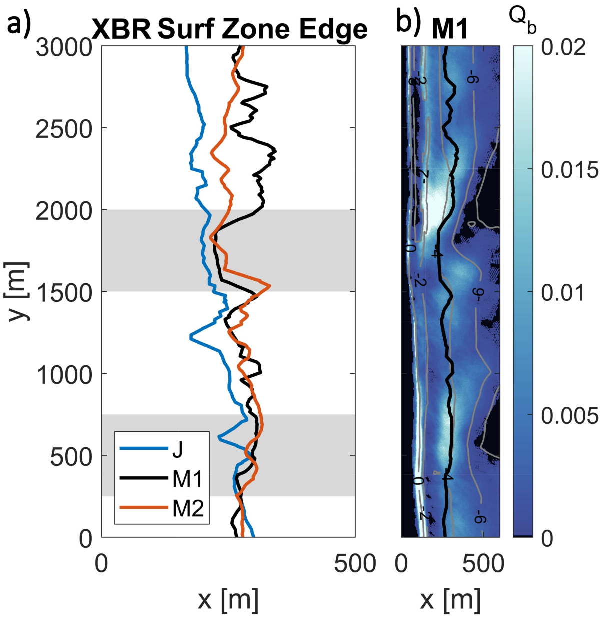

Figure 5. Surf zone detection from XBR observations and model: (a) XBR measurements of the cross-shore location of the offshore surf zone edge during event J (blue line), M1 (black line), and M2 (orange line) with shaded regions indicating the SOF troughs; (b) XBR-derived M1 surf zone edge (black line) over the simulated fraction of breaking waves (Q_b) for M1.

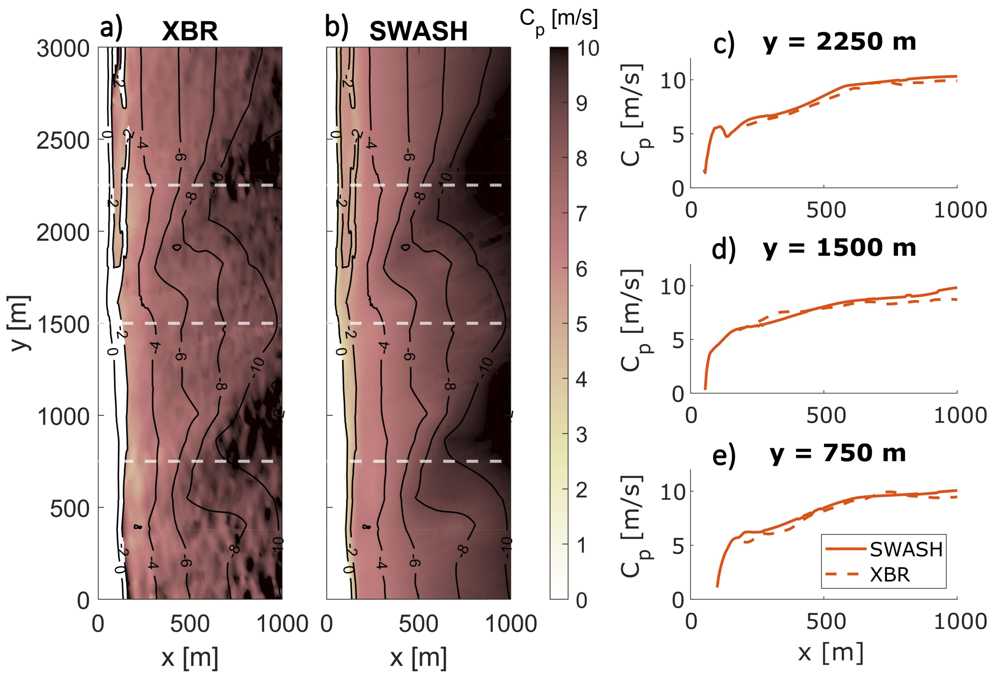

Figure 6. XBR observations and model results of wave celerity at the peak frequency (C_p) during M2: (a) XBR observations in areas deeper than 2 m, (b) SWASH results, and (c, d, e) cross-shore transects of modeling results (solid lines) and XBR observations (dashed lines) at alongshore locations (c) y = 2250 m, (d) y = 1500 m, and (e) y = 750 m. White dashed lines in (a) and (b) indicate the cross-shore transect locations.

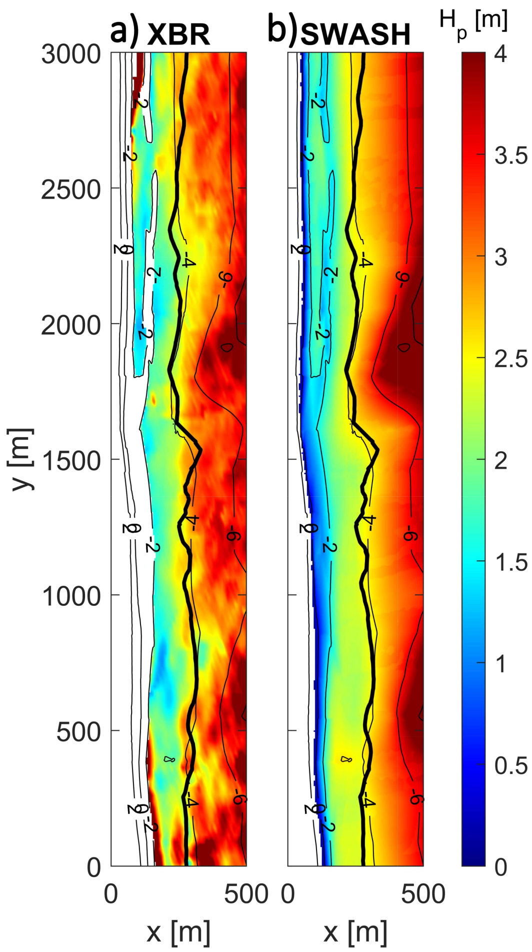

Figure 7. Estimates of the peak wave height (H_p) for event M2 from (a) XBR observations and (b) modelling results. Solid black lines in (a) and (b) represent the XBR-measured surf zone edge of M2.

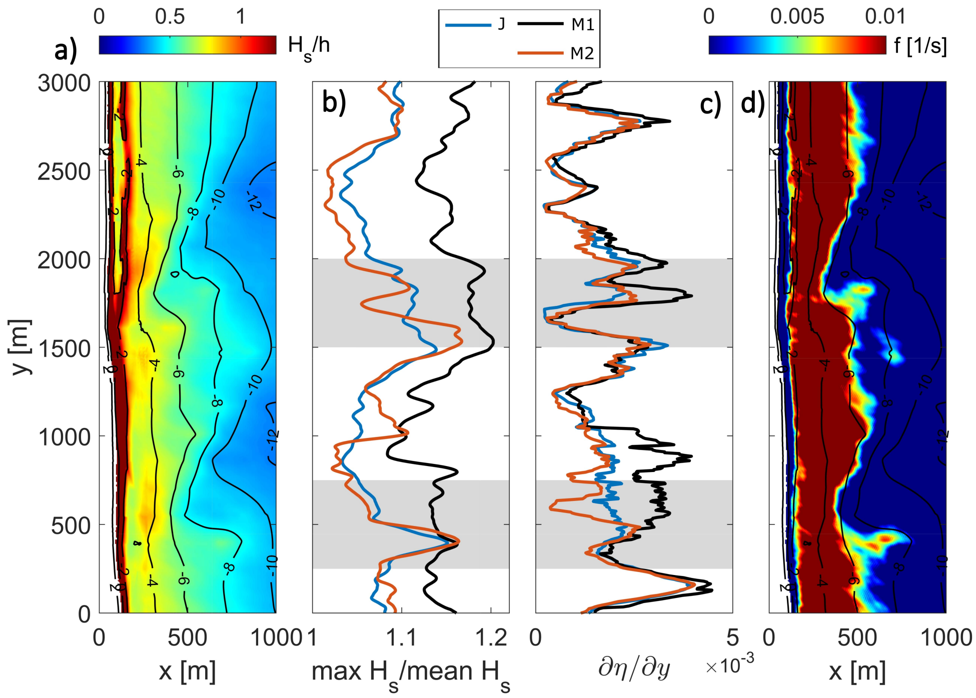

Figure 8. Wave height estimates from numerical simulations: (a) the spatial distribution of relative wave heights (H_s/h) during M1, (b) maximum H_s divided by mean H_s at each alongshore location for J (blue line), M1 (black line), and M2 (orange line), (c) maximum alongshore gradient in setup, and (d) saturated frequency map during M1. Gray shaded regions in (b) and (c) indicate the approximate bounds of the shore-oblique troughs.

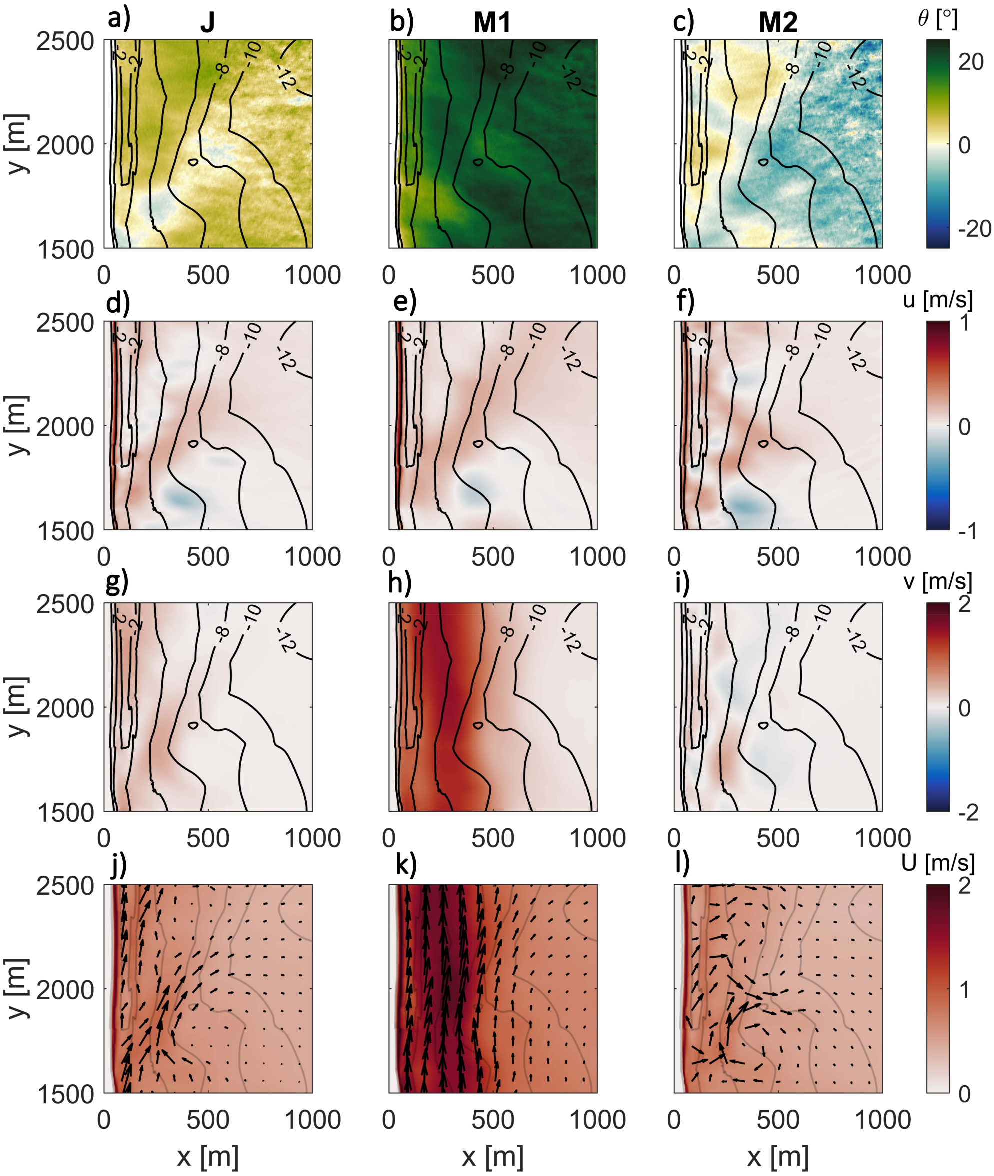

Figure 9. Flow dynamics around the northern shore-oblique feature between y = 1500 m – 2500 m for time periods (left column) J, (middle column) M1, and (right column) M2. Flow dynamics displayed include: (a, b, c) wave angle (θ) relative to shore-perpendicular, (d, e, f) cross-shore velocity (u), (g, h, i) alongshore velocity (v), and (j, k, l) overall depth averaged current velocity (U).

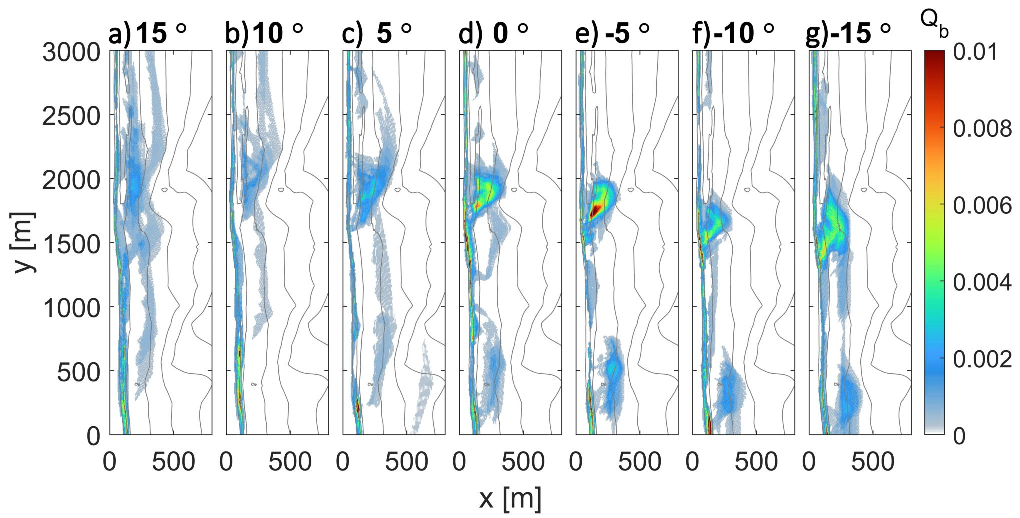

Figure 10. Fraction of breaking waves (Q_b) calculated from $H_s = 3$ m idealized simulations with various incident peak wave angles (θ_p): (a) 15°, (b) 10°, (c) 5°, (d) 0°, (e) -5°, (f) -10°, and (g) -15°.

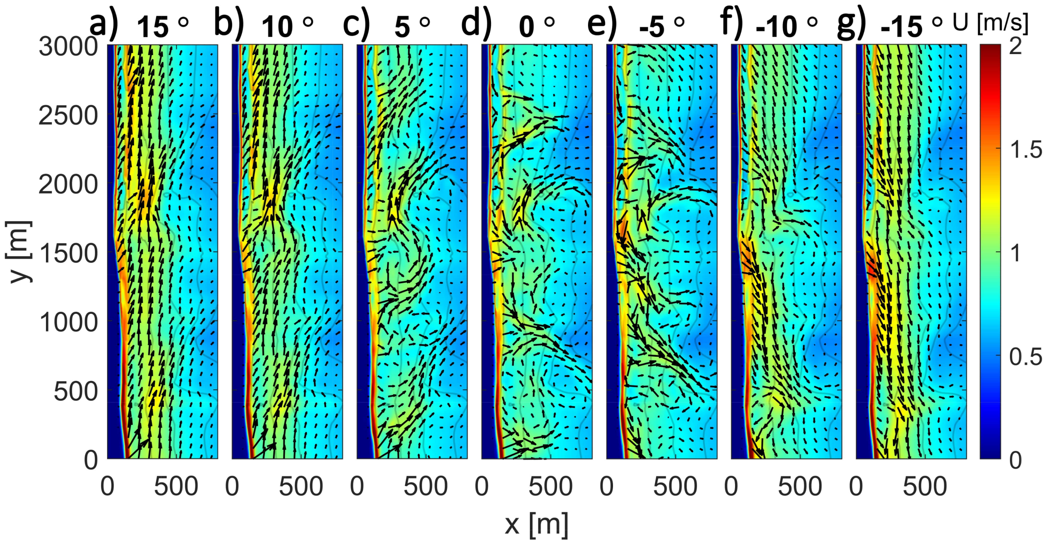

Figure 11. Depth-averaged current velocities (U) calculated from $H_s = 3$ m idealized simulations with various incident peak wave angles (θ_p): (a) 15°, (b) 10°, (c) 5°, (d) 0°, (e) -5°, (f) -10°, and (g) -15°.

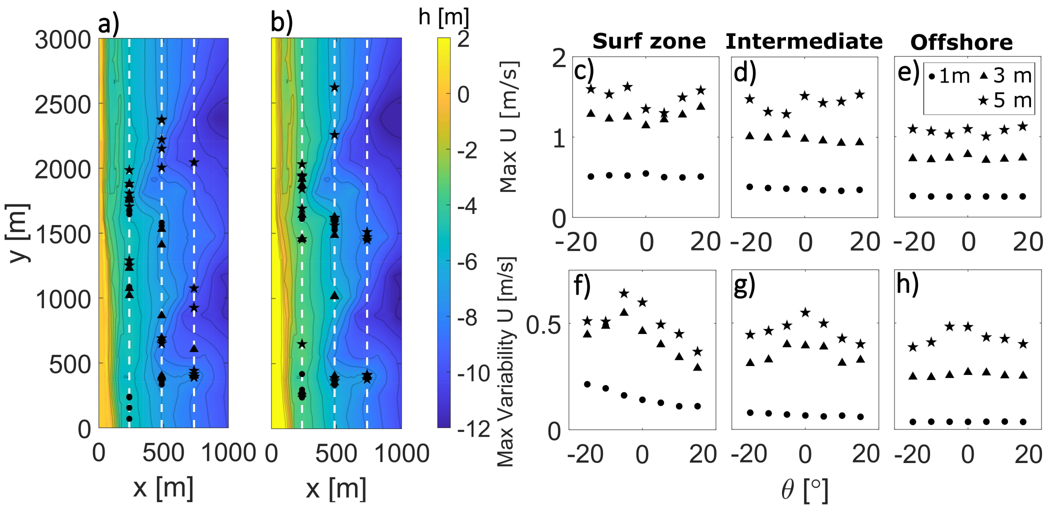

Figure 12. Locations of maximum U (a) and locations of maximum variability of U (b) during a variety of incident wave angles and significant wave heights (H_s), where circles represent an incoming H_s of 1 m, triangles represent H_s of 3 m, and stars represent H_s of 5 m. Quantified influence of incoming wave angle (θ) and H_s on maximum U (c-e) and the variability of U (f-h) in the surf, intermediate, and offshore zones. Cross-shore locations of the surf, intermediate, and offshore zones are depicted in (a) and (b) as white dashed lines.

References

APTIM. (2017). *2017 Town of Kitty Hawk, Town of Kill Devil Hills, NC beach profile survey report* (Tech. Rep.). 4038 Masonboro Loop Road, Wilmington, NC 28409: APTIM Coastal Planning and Engineering of North Carolina, Inc.

APTIM. (2019). *Town of Kitty Hawk and Kill Devil Hills, North Carolina 2018 shoreline change and volume change monitoring report* (Tech. Rep.). 4038 Masonboro Loop Road, Wilmington, NC 28409: APTIM Coastal Planning and Engineering of North Carolina, Inc.

Baker, C. M., Moulton, M., Raubenheimer, B., Elgar, S., & Kumar, N. (2021). Modeled three-dimensional currents and eddies on an alongshore-variable barred beach. *Journal of Geophysical Research: Oceans*, *126*(7), e2020JC016899.

Barrett, G., & Houser, C. (2012). Identifying hotspots of rip current activity using wavelet analysis at Pensacola Beach, Florida. *Physical Geography*, *33*(1), 32–49.

Boss, S. K., Hoffman, C. W., & Cooper, B. (2002). Influence of fluvial processes on the Quaternary geologic framework of the continental shelf, North Carolina, USA. *Marine Geology*, *183*(1-4), 45–65.

Bowen, A. J. (1969). Rip currents: 1. theoretical investigations. *Journal of Geophysical Research*, *74*(23), 5467–5478.

Brander, R. W., & Short, A. D. (2001). Flow kinematics of low-energy rip current systems. *Journal of Coastal Research*, 468–481.

Brodie, K. L., Palmsten, M. L., Hesser, T. J., Dickhudt, P. J., Raubenheimer, B., Ladner, H., & Elgar, S. (2018). Evaluation of video-based linear depth inversion performance and applications using altimeters and hydrographic surveys in a wide range of environmental conditions. *Coastal Engineering*, *136*, 147–160.

Browder, A. G., & McNinch, J. E. (2006). Linking framework geology and nearshore morphology: correlation of paleo-channels with shore-oblique sandbars and gravel outcrops. *Marine Geology*, *231*(1-4), 141–162.

Castelle, B., Scott, T., Brander, R., & McCarroll, R. (2016). Rip current types, circulation and hazard. *Earth-Science Reviews*, *163*, 1–21.

Catalán, P. A., Haller, M. C., & Plant, W. J. (2014). Microwave backscattering from surf zone waves. *Journal of Geophysical Research: Oceans*, *119*(5), 3098–3120.

Coco, G., Senechal, N., Rejas, A., Bryan, K. R., Capo, S., Parisot, J., ... MacMahan, J. H. (2014). Beach response to a sequence of extreme storms. *Geomorphology*, *204*, 493–501.

Colman, S. M., Halka, J. P., HOBBS III, C., Mixon, R. B., & Foster, D. S. (1990). Ancient channels of the susquehanna river beneath chesapeake bay and the delmarva peninsula. *Geological Society of America Bulletin*, *102*(9), 1268–1279.

Culver, S. J., Pre, C. A. G., Mallinson, D. J., Riggs, S. R., Corbett, D. R., Foley, J., ... others (2007). Late holocene barrier island collapse: Outer banks, north carolina, usa. *The Sedimentary Record*, *5*(4), 4–8.

Dalrymple, R. A. (1978). Rip currents and their causes. In *Coastal engineering 1978* (pp. 1414–1427).

Dalrymple, R. A., MacMahan, J. H., Reniers, A. J., & Nelko, V. (2011). Rip currents. *Annual Review of Fluid Mechanics*, *43*, 551–581.

da Silva, R. F., Hansen, J. E., Lowe, R. J., Rijnsdorp, D. P., & Buckley, M. L. (2023). Dynamics of the wave-driven circulation in the lee of nearshore reefs. *Journal of Geophysical Research: Oceans*, *128*(3), e2022JC019013.

Dean, R. G., & Dalrymple, R. A. (1991). *Water wave mechanics for engineers and scientists* (Vol. 2). world scientific publishing company.

Dodet, G., Castelle, B., Masselink, G., Scott, T., Davidson, M., Floc'h, F., ... Suanez, S. (2019). Beach recovery from extreme storm activity during the

2013–14 winter along the atlantic coast of europe. *Earth Surface Processes and Landforms*, *44*(1), 393–401.

Dusek, G., & Seim, H. (2013a). A probabilistic rip current forecast model. *Journal of Coastal Research*, *29*(4), 909–925.

Dusek, G., & Seim, H. (2013b). Rip current intensity estimates from lifeguard observations. *Journal of coastal research*, *29*(3), 505–518.

Dusek, G., Seim, H., Hanson, J., & Elder, D. (2011). Analysis of rip current rescues at kill devil hills, north carolina. *Rip Currents: Beach Safety, Physical Oceanography and Wave Modeling.*.

Engle, J. (2002). Formulation of a rip current predictive index using rescue data jason engle*, james macmahan, robert j. thieke, daniel m hanes and robert g dean* graduate assistant, department of civil and coastal engineering, university of florida phone:(352) 392-9537 ext-1410; email: engle@ coastal. ufl. edu. In *2002 national conference on beach preservation technology. florida shore & beach preservation association, citeseer* (Vol. 285).

Fenton, J. D., & McKee, W. (1990). On calculating the lengths of water waves. *Coastal Engineering*, *14*(6), 499–513.

Gallagher, E. L., Elgar, S., & Guza, R. (1998). Observations of sand bar evolution on a natural beach. *Journal of Geophysical Research: Oceans*, *103*(C2), 3203–3215.

Garnier, R., Falqués, A., Calvete, D., Thiebot, J., & Ribas, F. (2013). A mechanism for sandbar straightening by oblique wave incidence. *Geophysical Research Letters*, *40*(11), 2726–2730.

Gomes, E. R., Mulligan, R. P., Brodie, K. L., & McNinch, J. E. (2016). Bathymetric control on the spatial distribution of wave breaking in the surf zone of a natural beach. *Coastal Engineering*, *116*, 180–194.

Green, M. O., Vincent, C. E., & Trembanis, A. C. (2004). Suspension of coarse and fine sand on a wave-dominated shoreface, with implications for the development of rippled scour depressions. *Continental Shelf Research*, *24*(3), 317–335.

Gutierrez, B. T., Voulgaris, G., & Thieler, E. R. (2005). Exploring the persistence of sorted bedforms on the inner-shelf of wrightsville beach, north carolina. *Continental Shelf Research*, *25*(1), 65–90.

Guza, R., Thornton, E., & Christensen Jr, N. (1986). Observations of steady longshore currents in the surf zone. *Journal of physical oceanography*, *16*(11), 1959–1969.

Haller, M. C., Dalrymple, R. A., & Svendsen, I. A. (2002). Experimental study of nearshore dynamics on a barred beach with rip channels. *Journal of Geophysical Research: Oceans*, *107*(C6), 14–1.

Haller, M. C., Honegger, D., & Catalan, P. A. (2014). Rip current observations via marine radar. *Journal of waterway, port, coastal, and ocean engineering*, *140*(2), 115–124.

Hayes, M. (1979). *Barrier island morphology as a function of tidal and wave regime. In: Leatherman SP (ed), Barrier Islands: From the Gulf of St. Lawerence to the Gulf of Mexico.* Academic Press, New York.

Hedges, T. (1976). An empirical modification to linear wave theory. *Proceedings of the Institution of Civil Engineers*, *61*(3), 575–579.

Holman, R. A., & Bergsma, E. W. (2021). Updates to and performance of the cbathy algorithm for estimating nearshore bathymetry from remote sensing imagery. *Remote Sensing*, *13*(19), 3996.

Holman, R. A., Plant, N., & Holland, T. (2013b). cbathy: A robust algorithm for estimating nearshore bathymetry. *Journal of geophysical research: Oceans*, *118*(5), 2595–2609.

Holman, R. A., & Sallenger, A. H. (1993). Sand bar generation: a discussion of the duck experiment series. *Journal of Coastal Research*, 76–92.

Holman, R. A., Symonds, G., Thornton, E. B., & Ranasinghe, R. (2006). Rip spacing and persistence on an embayed beach. *Journal of Geophysical Research: Oceans*, *111*(C1).
Honegger, D. A., Haller, M. C., & Holman, R. A. (2019). High-resolution bathymetry estimates via x-band marine radar: 1. beaches. *Coastal Engineering*, *149*, 39–48.
Houser, C. (2012). Feedback between ridge and swale bathymetry and barrier island storm response and transgression. *Geomorphology*, *173*, 1–16.
Houser, C., Hapke, C., & Hamilton, S. (2008). Controls on coastal dune morphology, shoreline erosion and barrier island response to extreme storms. *Geomorphology*, *100*(3-4), 223–240.
Houser, C., Wernette, P., Trimble, S., & Locknick, S. (2020). Rip currents. *Sandy beach morphodynamics*, 255–276.
Humberston, J., Lippmann, T., & McNinch, J. (2019). Observations of wave influence on alongshore ebb-tidal delta morphodynamics at Oregon Inlet, NC. *Marine Geology*, *418*, 106040.
Kemp, A. C., Kegel, J. J., Culver, S. J., Barber, D. C., Mallinson, D. J., Leorri, E., . . . others (2017). Extended late holocene relative sea-level histories for north carolina, usa. *Quaternary Science Reviews*, *160*, 13–30.
Knutson, T. R., McBride, J. L., Chan, J., Emanuel, K., Holland, G., Landsea, C., . . . Sugi, M. (2010). Tropical cyclones and climate change. *Nature geoscience*, *3*(3), 157–163.
Komar, P. D., & McDougal, W. G. (1988). Coastal erosion and engineering structures: the oregon experience. *Journal of Coastal Research*, 77–92.
Kuik, A., Van Vledder, G. P., & Holthuijsen, L. (1988). A method for the routine analysis of pitch-and-roll buoy wave data. *Journal of physical oceanography*, *18*(7), 1020–1034.
Kumar, N., & Feddersen, F. (2017). The effect of stokes drift and transient rip currents on the inner shelf. part i: No stratification. *Journal of Physical Oceanography*, *47*(1), 227–241.
Kumar, N., Lerczak, J. A., Xu, T., Waterhouse, A. F., Thomson, J., Terrill, E. J., . . . others (2021). The inner-shelf dynamics experiment. *Bulletin of the American Meteorological Society*, *102*(5), E1033–E1063.
Kumar, N., Voulgaris, G., & Warner, J. C. (2011). Implementation and modification of a three-dimensional radiation stress formulation for surf zone and rip-current applications. *Coastal Engineering*, *58*(12), 1097–1117.
Larson, M., & Kraus, N. C. (1994). Temporal and spatial scales of beach profile change, duck, north carolina. *Marine Geology*, *117*(1-4), 75–94.
Leatherman, S., & Fletemeyer, J. (2011). *Rip currents: Beach safety, physical oceanography, and wave modeling*. CRC Press.
Lippmann, T., & Holman, R. (1989). Quantification of sand bar morphology: A video technique based on wave dissipation. *Journal of Geophysical Research: Oceans*, *94*(C1), 995–1011.
Lippmann, T., Holman, R. A., & Hathaway, K. (1993). Episodic, nonstationary behavior of a double bar system at Duck, North Carolina, USA, 1986–1991. *Journal of Coastal Research*, 49–75.
List, J. H., Farris, A. S., & Sullivan, C. (2006). Reversing storm hotspots on sandy beaches: Spatial and temporal characteristics. *Marine Geology*, *226*(3-4), 261–279.
Long, J. W., & Özkan-Haller, H. T. (2005). Offshore controls on nearshore rip currents. *Journal of geophysical research: oceans*, *110*(C12).
Longuet-Higgins, M. S. (1970). Longshore currents generated by obliquely incident sea waves: 1. *Journal of geophysical research*, *75*(33), 6778–6789.
Longuet-Higgins, M. S., & Stewart, R. (1964). Radiation stresses in water waves; a physical discussion, with applications. In *Deep sea research and oceanographic*

abstracts (Vol. 11, pp. 529–562).

Lygre, A., & Krogstad, H. E. (1986). Maximum entropy estimation of the directional distribution in ocean wave spectra. *Journal of Physical Oceanography*, *16*(12), 2052–2060.

Lyzenga, D. R. (1991). Interaction of short surface and electromagnetic waves with ocean fronts. *Journal of Geophysical Research: Oceans*, *96*(C6), 10765–10772.

MacMahan, J., Brown, J., Brown, J., Thornton, E., Reniers, A., Stanton, T., ... others (2010). Mean lagrangian flow behavior on an open coast rip-channeled beach: A new perspective. *Marine Geology*, *268*(1-4), 1–15.

MacMahan, J., Thornton, E. B., & Reniers, A. J. (2006). Rip current review. *Coastal engineering*, *53*(2-3), 191–208.

MacMahan, J., Thornton, E. B., Stanton, T. P., & Reniers, A. J. (2005). Ripex: Observations of a rip current system. *Marine Geology*, *218*(1-4), 113–134.

Magne, R., Belibassakis, K., Herbers, T. H., Ardhuin, F., O'Reilly, W. C., & Rey, V. (2007). Evolution of surface gravity waves over a submarine canyon. *Journal of Geophysical Research: Oceans*, *112*(C1).

Mallinson, D., Burdette, K., Mahan, S., & Brook, G. (2008). Optically stimulated luminescence age controls on late pleistocene and holocene coastal lithosomes, north carolina, usa. *Quaternary Research*, *69*(1), 97–109.

McNinch, J. E. (2004). Geologic control in the nearshore: shore-oblique sandbars and shoreline erosional hotspots, Mid-Atlantic Bight, USA. *Marine Geology*, *211*(1-2), 121–141.

McNinch, J. E. (2007). Bar and swash imaging radar (basir): A mobile x-band radar designed for mapping nearshore sand bars and swash-defined shorelines over large distances. *Journal of Coastal Research*, *23*(1), 59–74.

McNinch, J. E., Brodie, K. L., & Slocum, R. K. (2012). Radar Inlet Observing System (RIOS): Continuous remote sensing of waves, currents, and bathymetry at tidal inlets. In *Oceans* (pp. 1–8).

McNinch, J. E., & Miselis, J. L. (2012). Geology metrics for predicting shoreline change using seabed and sub-bottom observations from the surf zone and nearshore. *Sediments, Morphology and Sedimentary Processes on Continental Shelves: Advances in Technologies, Research, and Applications*, 99–119.

Moulton, M., Elgar, S., Raubenheimer, B., Warner, J. C., & Kumar, N. (2017). Rip currents and alongshore flows in single channels dredged in the surf zone. *Journal of Geophysical Research: Oceans*, *122*(5), 3799–3816.

Moulton, M., Suanda, S. H., Garwood, J. C., Kumar, N., Fewings, M. R., & Pringle, J. M. (2023). Exchange of plankton, pollutants, and particles across the nearshore region. *Annual Review of Marine Science*, *15*, 167–202.

Mulligan, R. P., Gomes, E. R., Miselis, J. L., & McNinch, J. E. (2019a). Non-hydrostatic numerical modelling of nearshore wave transformation over shore-oblique sandbars. *Estuarine, Coastal and Shelf Science*, *219*, 151–160.

Mulligan, R. P., Mallinson, D. J., Clunies, G. J., Rey, A., Culver, S. J., Zaremba, N., ... Mitra, S. (2019b). Estuarine responses to long-term changes in inlets, morphology, and sea level rise. *Journal of Geophysical Research: Oceans*, *124*(12), 9235–9257.

North Carolina Division Of Coastal Management. (2021). `https://www.deq.nc.gov/about/divisions/coastal-management/coastal-management-oceanfront-shorelines/oceanfront-construction-setback-erosion-rate`. 400 Commerce Avenue Morehead City, NC 28557. (Accessed: 2023-08-10)

Oades, E. M., Mulligan, R., & Palmsten, M. (2023). Evaluation of nearshore bathymetric inversion algorithms using camera observations and synthetic numerical input of surface waves during storms. *Coastal Engineering*, 104338.

O'Dea, A., Kumar, N., & Haller, M. C. (2021). Simulations of the surf zone eddy field and cross-shore exchange on a nonidealized bathymetry. *Journal of Geo-*

physical Research: Oceans, *126*(5), e2020JC016619.
Pattiaratchi, C., Olsson, D., Hetzel, Y., & Lowe, R. (2009). Wave-driven circulation patterns in the lee of groynes. *Continental Shelf Research*, *29*(16), 1961–1974.
Plant, W. J., Keller, W. C., Hayes, K., & Chatham, G. (2010). Normalized radar cross section of the sea for backscatter: 1. mean levels. *Journal of Geophysical Research: Oceans*, *115*(C9).
Raubenheimer, B., Guza, R., & Elgar, S. (1996). Wave transformation across the inner surf zone. *Journal of Geophysical Research: Oceans*, *101*(C11), 25589–25597.
Riggs, S. R., Cleary, W. J., & Snyder, S. W. (1995). Influence of inherited geologic framework on barrier shoreface morphology and dynamics. *Marine geology*, *126*(1-4), 213–234.
Riggs, S. R., York, L. L., Wehmiller, J. F., & Snyder, S. W. (1992). Depositional patterns resulting from high-frequency quaternary sea-level fluctuations in northeastern north carolina. *Quaternary Coasts of the United States: Marine and Lacustrine Systems*.
Safak, I., List, J. H., Warner, J. C., & Schwab, W. C. (2017). Persistent shoreline shape induced from offshore geologic framework: Effects of shoreface connected ridges. *Journal of Geophysical Research: Oceans*, *122*(11), 8721–8738.
Sallenger, A. H., Doran, K. S., & Howd, P. A. (2012). Hotspot of accelerated sea-level rise on the atlantic coast of north america. *Nature Climate Change*, *2*(12), 884–888.
Schupp, C. A., McNinch, J. E., & List, J. H. (2006). Nearshore shore-oblique bars, gravel outcrops, and their correlation to shoreline change. *Marine Geology*, *233*(1-4), 63–79.
Schwab, W. C., Thieler, E. R., Allen, J. R., Foster, D. S., Swift, B. A., & Denny, J. F. (2000). Influence of inner-continental shelf geologic framework on the evolution and behavior of the barrier-island system between fire island inlet and shinnecock inlet, long island, new york. *Journal of Coastal Research*, 408–422.
Schwartz, R. K., & Birkemeier, W. A. (2004). Sedimentology and morphodynamics of a barrier island shoreface related to engineering concerns, outer banks, nc, usa. *Marine Geology*, *211*(3-4), 215–255.
Short, A. (2007). Australian rip systems–friend or foe? *Journal of Coastal Research*, 7–11.
Smit, P., Zijlema, M., & Stelling, G. (2013). Depth-induced wave breaking in a non-hydrostatic, near-shore wave model. *Coastal Engineering*, *76*, 1–16.
Snedden, J. W., Tillman, R. W., Kreisa, R. D., Schweller, W. J., Culver, S. J., & Winn, R. D. (1994). Stratigraphy and genesis of a modern shoreface-attached sand ridge, peahala ridge, new jersey. *Journal of Sedimentary Research*, *64*(4b), 560–581.
Sonu, C. J. (1972). Field observation of nearshore circulation and meandering currents. *Journal of Geophysical Research*, *77*(18), 3232–3247.
Splinter, K. D., & Palmsten, M. L. (2012). Modeling dune response to an east coast low. *Marine Geology*, *329*, 46–57.
Splinter, K. D., Turner, I. L., Davidson, M. A., Barnard, P., Castelle, B., & Oltman-Shay, J. (2014). A generalized equilibrium model for predicting daily to interannual shoreline response. *Journal of Geophysical Research: Earth Surface*, *119*(9), 1936–1958.
Streßer, M., Horstmann, J., & Baschek, B. (2022). Surface wave and roller dissipation observed with shore-based doppler marine radar. *Journal of Geophysical Research: Oceans*, *127*(8), e2022JC018437.
Suanda, S. H., & Feddersen, F. (2015). A self-similar scaling for cross-shelf exchange driven by transient rip currents. *Geophysical Research Letters*, *42*(13), 5427–5434.

Svendsen, I. A. (1984). Mass flux and undertow in a surf zone. *Coastal engineering*, *8*(4), 347–365.

Szczyrba, L. D., Mulligan, R. P., Humberston, J. L., Bak, A. S., McNinch, J. E., & Pufahl, P. K. (2023b). Nearshore wave angles and directional variability during storm events. *Coastal Engineering*, 104372.

Szczyrba, L. D., Mulligan, R. P., Pufahl, P. K., Humberston, J. L., & McNinch, J. E. (2023a). Morphodynamic link between shore-oblique bars and erosional hotspots. *Coastal Sediments 2023: The Proceedings of the Coastal Sediments 2023*, 1907–1922.

Takewaka, S., & Yamakawa, T. (2011). Rip current observation with x-band radar. *Coastal Engineering Proceedings*(32), 43–43.

Thieler, E. R., Brill, A. L., Cleary, W. J., Hobbs III, C. H., & Gammisch, R. A. (1995). Geology of the wrightsville beach, north carolina shoreface: Implications for the concept of shoreface profile of equilibrium. *Marine Geology*, *126*(1-4), 271–287.

Turner, I. L., Whyte, D., Ruessink, B., & Ranasinghe, R. (2007). Observations of rip spacing, persistence and mobility at a long, straight coastline. *Marine Geology*, *236*(3-4), 209–221.

Voulgaris, G., Kumar, N., & Warner, J. C. (2011). Methodology for prediction of rip currents using a three-dimensional numerical, coupled, wave current model. In *First international rip current symposium* (pp. 87–105).

Walsh, K. J., McBride, J. L., Klotzbach, P. J., Balachandran, S., Camargo, S. J., Holland, G., ... others (2016). Tropical cyclones and climate change. *Wiley Interdisciplinary Reviews: Climate Change*, *7*(1), 65–89.

Wernette, P., & Houser, C. (2022). evidence for geologic control of rip channels along prince edward island, canada. *Physical Geography*, *43*(2), 145–162.

Wright, L. D., & Short, A. D. (1984). Morphodynamic variability of surf zones and beaches: a synthesis. *Marine geology*, *56*(1-4), 93–118.

Zijlema, M. (2020). Computation of free surface waves in coastal waters with swash on unstructured grids. *Computers & Fluids*, *213*, 104751.

Zijlema, M., Stelling, G., & Smit, P. (2011). SWASH: An operational public domain code for simulating wave fields and rapidly varied flows in coastal waters. *Coastal Engineering*, *58*(10), 992–1012.

Zijlema, M., & Stelling, G. S. (2005). Further experiences with computing non-hydrostatic free-surface flows involving water waves. *International journal for numerical methods in fluids*, *48*(2), 169–197.